



Leif Robin Knöpke



**Reaction monitoring in multiphase systems:
Application of coupled in situ spectroscopic
techniques in organic synthesis**



Cuvillier Verlag Göttingen
Internationaler wissenschaftlicher Fachverlag



Reaction monitoring in multiphase systems:
Application of coupled in situ spectroscopic techniques
in organic synthesis





**Reaction monitoring in multiphase systems:
Application of coupled in situ spectroscopic techniques
in organic synthesis**

Dissertation

zur

Erlangung des akademischen Grades

doctor rerum naturalium (Dr. rer. nat.)

der Mathematisch-Naturwissenschaftlichen Fakultät

der Universität Rostock

vorgelegt von

Diplom-Chemiker Leif Robin Knöpke

aus Hilden (Rheinland)



Bibliografische Information der Deutschen Nationalbibliothek

Die Deutsche Nationalbibliothek verzeichnet diese Publikation in der Deutschen Nationalbibliografie; detaillierte bibliografische Daten sind im Internet über <http://dnb.d-nb.de> abrufbar.

1. Aufl. - Göttingen : Cuvillier, 2012

Zugl.: Rostock, Univ., Diss., 2012

978-3-95404-029-2

1. Gutachter

Professor Dr. Angelika Brückner

Leibniz-Institut für Katalyse e.V. an der Universität Rostock

2. Gutachter

Professor Dr. Dr. h.c. Peter Langer

Institut für Chemie der Universität Rostock

Tag des wissenschaftlichen Kolloquiums: 24. Januar 2012

© CUVILLIER VERLAG, Göttingen 2012

Nonnenstieg 8, 37075 Göttingen

Telefon: 0551-54724-0

Telefax: 0551-54724-21

www.cuvillier.de

Alle Rechte vorbehalten. Ohne ausdrückliche Genehmigung des Verlages ist es nicht gestattet, das Buch oder Teile daraus auf fotomechanischem Weg (Fotokopie, Mikrokopie) zu vervielfältigen.

1. Auflage, 2012

Gedruckt auf säurefreiem Papier

978-3-95404-029-2



TABLE OF CONTENTS

Zusammenfassung	iii
Abstract	v
Selbständigkeitserklärung	vii
Acknowledgements	ix
1. MOTIVATION AND OBJECTIVES	1
2. STATE OF THE ART	5
2.1. Opportunities and limitations of common in situ methods	5
2.2. In situ studies by coupled techniques	10
3. TECHNICAL PART	15
3.1. Development of a reaction cell for the in situ investigations of low-temperature preparation processes	15
3.2. Development of a reaction cell for the in situ investigations of pressure reactions in multiphase systems	17
4. APPLICATION EXAMPLE 1: Elucidating the directing effect of the used Lewis acid on the reaction pathway in formal [3+3] cyclocondensation reactions	23
4.1. The ex situ studies at room temperature	24
4.2. The in situ studies under reaction conditions	32
4.3. Conclusion 1	39
4.4. Transfer of the obtained results to similar systems	39
4.5. Utilisation of aluminium(III)chloride as Lewis acid	40
4.6. Supplementary ex situ investigations	45
4.7. From single phase to multiphase systems: utilisation of solid Lewis Acids	47
4.8. Introduction of N-salicylideneaniline 14 as substrate for the reaction	50
4.9. Influence of the reaction time	59
4.10. Conclusion 2	60



TABLE OF CONTENTS

5.	APPLICATION EXAMPLE 2: Heterogeneously catalysed asymmetric hydrogenation of imines: Reaction monitoring and Mechanistic studies	63
5.1.	Interaction of selected imines with the chiral modifier in liquid phase	65
5.2.	Interaction of selected imines with the catalyst surface	74
5.3.	Interaction of the chiral modifier 22 with the catalyst surface	81
5.4.	Elucidation of the adsorption sites	83
5.5.	In situ studies: Testing of the reaction unit	85
5.6.	Conclusion 3	91
6.	GENERAL CONCLUSION AND OUTLOOK	95
7.	LITERATURE	99
	APPENDIX	A
	Experimental Section Application Example 1	A
	Experimental Section Application Example 2	C
	Selected bond lengths and angles in the bis-chelate complex 8b	F
	ATR-FTIR and Raman spectra of N-salicylideneaniline 14 in CCl ₄ (cf. Figure 25)	G
	ATR-FTIR spectrum of the 1:1-mixture of 14 and 22 in CH ₂ Cl ₂ before the co-adsorption experiments on Pt/Al ₂ O ₃ took place (cf. Figure 41)	H
	Remark to the spectroscopic limitations	I
	Remark to the limitations measuring kinetics	L
	Table of compounds	N
	Supplementary literature	R



Die Vorteile der Kopplung von in situ spektroskopischen Methoden (ATR-FTIR / UV-vis / Raman-Spektroskopie) wurde exemplarisch anhand zweier Beispielreaktionen demonstriert: der Lewis-Säure-gesteuerten formalen [3+3]-Cyclokondensation eines Diens mit einem Ketenacetal und der heterogenkatalysierten enantioselektiven Hydrierung von Iminen. Für beide Reaktionen wurden neue Reaktoren (Tieftemperaturzelle, Sondenautoklav) entwickelt, die in situ-Messungen unter realen Reaktionsbedingungen ermöglichen.

Für die [3+3]-Cyclokondensation konnte gezeigt werden, dass die Produktbildung von der Art der Intermediate abhängt, die durch die Wechselwirkung von Lewis-Säure und Ketenacetal gebildet werden (Komplexbildung oder säurekatalysierte Umlagerung). Darüber hinaus konnten die Mechanismen von ähnlichen Reaktionen (Einsatz anderer Lewis-Säuren wie AlCl_3 , Al_2O_3 und TiO_2 oder anderer Substrate wie N-Salicylidenanilin) erfolgreich aufgeklärt werden.

Die Effektivität der Hydrierung hängt von der Wechselwirkung der getesteten Ketimine mit dem als chiralen Modifikator eingesetztem Phosphorsäureester ab. Diese Wechselwirkung ist lösungsmittelabhängig und führt zur Bildung eines Carbokations (CH_3OH) oder eines Kontaktionenpaars (CH_2Cl_2 , $\text{CF}_3\text{CH}_2\text{OH}$). Ferner wurde gezeigt, dass die starke Adsorption von Iminen und Modifikator an der Oberfläche des Pt/ Al_2O_3 -Katalysators ihre Wirksamkeit in der Reaktion nachteilig beeinflusst.



The benefit of coupling different in situ spectroscopic methods (ATR-FTIR / UV-vis / Raman spectroscopy) is exemplarily demonstrated by the means of two reactions as application examples: the Lewis acid mediated formal [3+3] cyclocondensation reaction of a diene with a ketenacetal and the heterogeneously catalysed asymmetric hydrogenation of imines. For both reactions new reactors (deep-temperature cell, probe autoclave) have been developed enabling in situ measurements under real reaction conditions

For the [3+3] cyclocondensation reaction it was demonstrated that the nature of the formed product depends on the different intermediates formed between the ketenacetal and the acids (complexation or acid catalysed rearrangement reaction). Furthermore the mechanisms of similar reactions (including other Lewis acids like AlCl_3 , Al_2O_3 and TiO_2 or substrates like N-salicylideneaniline) could be successfully elucidated.

The effectiveness of the hydrogenation depends on the specific interaction of the tested ketimines with the phosphoric acid ester used as chiral modifier. This interaction is mainly influenced by the used solvent and leads to the formation of a carbocation (CH_3OH) or a contact ion pair in (CH_2Cl_2 , $\text{CF}_3\text{CH}_2\text{OH}$). Furthermore, the detected strong adsorption of imines and modifier on the $\text{Pt}/\text{Al}_2\text{O}_3$ catalyst affect their efficiency and activity in the reaction.





Ich gebe folgende Erklärung ab:

1. Die Gelegenheit zum vorliegenden Promotionsvorhaben ist mir nicht kommerziell vermittelt worden. Insbesondere habe ich keine Organisation eingeschaltet, die gegen Entgelt Betreuerinnen/Betreuer für die Anfertigung von Dissertationen sucht oder die mir obliegenden Pflichten hinsichtlich der Prüfungsleistungen für mich ganz oder teilweise erledigt.
2. Ich versichere hiermit an Eides statt, dass ich die vorliegende Arbeit selbstständig angefertigt und ohne fremde Hilfe verfasst habe. Dazu habe ich keine außer den von mir angegebenen Hilfsmitteln und Quellen verwendet und die den benutzten Werken inhaltlich und wörtlich entnommenen Stellen habe ich als solche kenntlich gemacht.

Rostock, den 29. November 2011

gez. Leif Robin Knöpke



First of all I would like to thank Dr U. Bentrup for the kind supervision of my work, for raising my awareness for the shape of spectra and for the interesting scientific discussions we had. I would also like to thank Professor Dr A. Brückner for her supervision of my work, the helpful discussions and for being referee of my work. My thanks go as well to Professor Dr Dr hc P. Langer for being referee of my work.

Special thanks go to S. Reimann who prepared the 1,3-bis(silyloxy)-1,3-butadiene and the ketenacetals, performed the reference experiments and also the work-up procedures in the cyclocondensation reactions.

Special thanks go also to Dr A. Köckritz and Dr N. Nemati for the helpful discussions and the support in synthetic matters concerning the heterogeneous catalysed asymmetric hydrogenation of imines.

I would like to thank kindly C. Rautenberg for helping me concerning several technical questions and for the measurement of FTIR-transmission spectra of the solid catalysts from self-supporting wafers, Dr M.-M. Pohl for measuring the TEM-pictures of the solid catalysts and Dr A. Spannenberg for the analysis of the single crystals. J. Dewart and M. Auer from the technical department I want to thank for helping me with the construction of the measuring cells and U. Bratsch for measuring supplementary FTIR-transmission spectra of solid catalysts.

Many thanks go to all the members of the departments of Catalytic in situ studies, Heterogeneous catalytic processes, Analytical service and Technical service who helped me on several occasions.

Finally, very special thanks go to my family, my friends and my office mates M. Baseda Krüger and Dr M. Bartoszek for their support.





THREE VIEWS OF A SECRET

John Francis "Jaco" Pastorius III



1. Motivation and Objectives

In situ spectroscopy is the only approach to derive reliable information on mechanisms and the role of intermediates in chemical reactions as well as on structure-reactivity relationships in catalysis [1-6].

In catalysis, the application of a variety of in situ methods has gained a lively development during the last two decades [1]. However, usually a complex network of reaction steps including interaction and conversion of reactants, formation of different intermediates as well as changes of the catalysts is passed during catalytic reactions which cannot be satisfactorily explored by applying only single spectroscopic in situ methods, since each of these techniques monitors only a restricted part of the overall reaction process.

Therefore, it is necessary to investigate chemical reactions by different in situ methods to obtain comprehensive information. If possible, a simultaneous coupling of such methods in the same experiment would be desirable to obtain most authentic results. An overview of opportunities is given in section 2. So far, there exist only few examples in which several in situ methods have been combined to analyse chemical reactions, under pressure or at temperatures below room temperature.

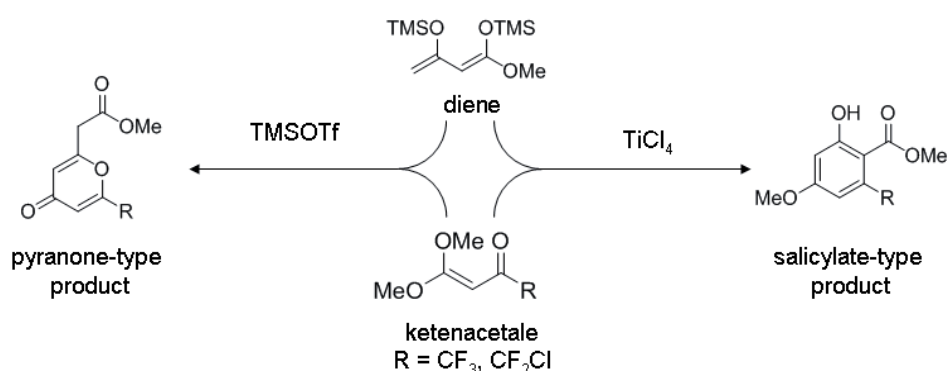
However, frequently chemical reactions have to be performed at elevated pressures or at low temperatures. This requires the use of special reactors that can be tempered and / or pressurised. The implementation of spectroscopic in situ methods in such reactor systems is still a widely unsolved problem and a true challenge.

It is the aim of this work to explore the potential of coupled in situ FTIR-ATR / UV-vis / Raman spectroscopy for applications at low temperature and higher pressures. This implies the development of sophisticated reactors with implemented spectroscopic probes. The following case studies have been selected to demonstrate the benefit of method coupling:

1. Elucidating the directing effect of the used Lewis acid on the reaction pathway in formal [3+3] cyclocondensation reactions
2. Heterogeneously catalysed asymmetric hydrogenation of imines: Reaction monitoring and mechanistic studies

In the first application example two different Lewis acids (TiCl_4 and TMSOTf) are utilised for the coupling of a 1,3-bis(silyloxy)-1,3-butadiene and a ketenacetale. Depending on the

applied acids, completely different products in form of salicylates or pyranones are obtained, although the same reaction conditions are applied (cf. Scheme 1) [7, 8]. In order to elucidate the driving force of the product selectivity of the [3+3] cyclisation reaction, the combined application of different spectroscopic methods becomes necessary [9]. Methods such as ATR-FTIR, UV-vis, and Raman spectroscopy are useful for studying the specific interactions between the Lewis acids TiCl_4 and TMSOTf with both reactants. Whereas ATR-FTIR and Raman spectroscopy reveal information of changes in terms of vibrations of characteristic bonds, UV-vis spectroscopy gives insight about changes of the electronic state of the molecules.



Scheme 1: Scheme of the Lewis acid mediated formal [3+3] cyclocondensation reaction; different products are obtained when TMSOTf or TiCl_4 are applied as mediating acid.

The obtained results from the in situ experiments shall be used as a basis for further investigations of this reaction type (cf. Figure 1). Thus, the possible utilisation of AlCl_3 , TiO_2 and Al_2O_3 as Lewis acids was proved. Furthermore, the nitrogen-containing N-salicylideneaniline was chosen as substrate.

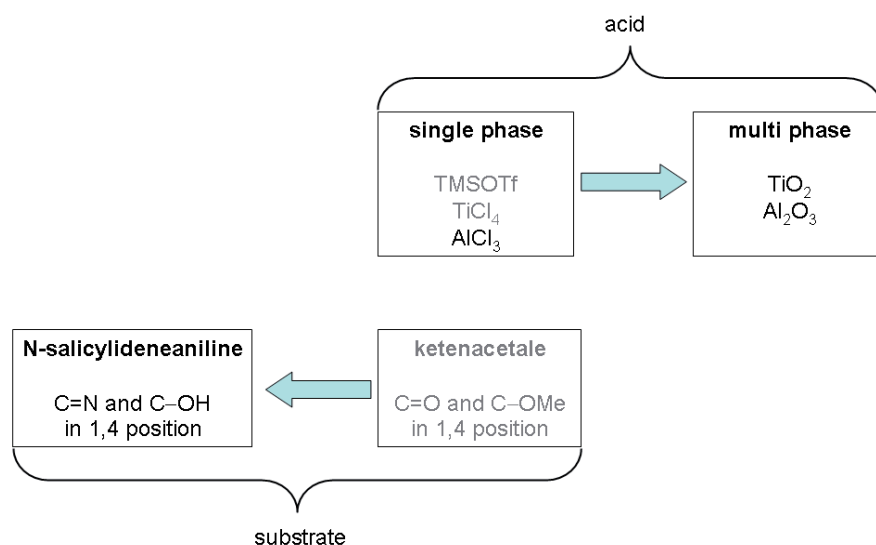


Figure 1: Transfer of the obtained results from the mechanistic investigations of the cyclocondensation reaction (grey) to similar systems (black).

In the second application example a new approach for the heterogeneously catalysed asymmetric hydrogenation of C=N double bonds is pursued using molecular hydrogen as hydrogen source. Supported noble metal catalysts are used for the activation of hydrogen. The implementation of chirality is effected by a suitable modifier like chiral phosphoric acid esters [10] (cf. Figure 2). First of all, the interaction between chiral modifier and solid catalyst are of interest. Only if the chiral modifier adsorbs with the right site on the surface of the catalyst, the modification of the surface will be successful. If the chiral modifier adsorbs with the wrong site or does not adsorb at all, the modification would be failed. The adsorption of the substrates and corresponding products is of interest, too, because adsorbates are important for the investigation of deactivation processes. Surface analysis combined with catalytic tests give insight if adsorbates deactivate the catalyst or not.

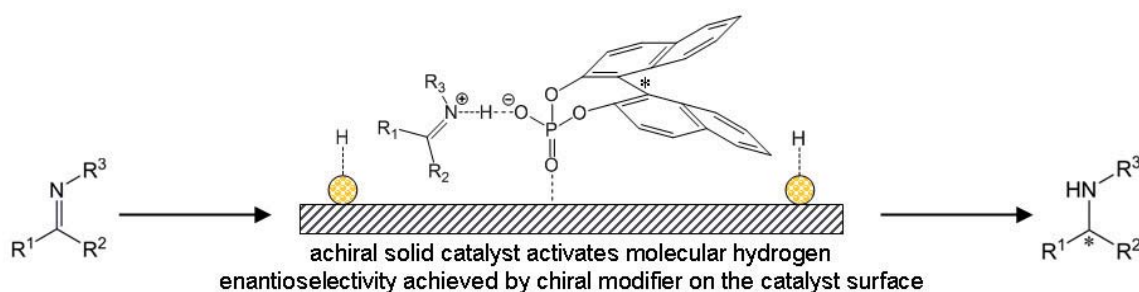


Figure 2: Principle of the heterogeneous catalyzed asymmetric hydrogenation of imines.

Although the interaction of imine and modifier shall occur at the surface of the catalyst, the interaction between both compounds have to be studied separately in liquid phase as well. The complexity of the system – substrate, modifier, catalyst, product, solvent – requires, besides the spectroscopic study of the single compounds, also studies of the mixtures. The main investigations will be focussed on the interaction between the imine and the chiral modifier because this is an essential step of the reaction.





2. State of the Art

2.1 Opportunities and limitations of common in situ methods

Numerous methods are suitable for in situ analysis. Several examples are known from magnetic resonance techniques, X-ray absorption and scattering methods, optical spectroscopy and even electron microscopy [1, 6, 11]. However, the field of application of most of these methods is determined by technical aspects.

NMR spectroscopy is not applicable to all nuclei and quenching problems may occur in the presence of paramagnetic species. On the other hand EPR spectroscopy can only detect systems with unpaired electrons. This limits the application potential for these methods. Furthermore, both methods require a homogeneous magnetic field. Therefore, the reactor geometry has to be narrow. Here, the application of small unstirred tube-type batch-reactors (e.g. NMR or EPR tubes) or of plug flow reactors (which require no stirring) is possible. The magnetic properties of the reactor wall materials have to be considered in every case. Even small impurities in the reactor material may cause fundamental perturbation of the analysis. Due to this fact the application of quartz glass reactors is essential in EPR spectroscopy because normal glass contains paramagnetic impurities which hinder a proper analysis. On the other hand all materials with high magnetic susceptibility constants cause problems when there are exposed to the magnetic fields of the spectrometers.

The application of X-ray methods is also limited referring to reactor geometry and materials. Common sample cells are rather narrow and a restrictive shielding to protect the operator and ambience from radiation is required. Due to the shielding manipulation of the reaction and monitoring of the running equipment inside the sample cell is often difficult. Optical control is commonly performed by cameras and all wires leading to control units have to pass special sewers through the shielding.

Discrete measurements inside the reaction mixture become necessary if the reaction conditions cannot be hold up in all locations in the reactor. For instance the vicinity of the walls is a critical zone referring to temperature and mixing. The analysis of inhomogeneous reaction mixtures requires proper spatial resolution. This can be archived by the implementation of probes which dip into the reaction mixture at the required point. Another problem is the analysis of pressure reactions inside stainless steel autoclaves. Therefore, aligned radiation and a sewer connection inside are required.

Contrary, to magnetic fields and X-ray beams optical radiation in form of ultraviolet, visible and infrared light can be aligned and routed easily. Classical tools for this are lenses, prisms and mirrors. These tools have in common that they can route beams straightforward only. But complex reactor geometries in narrow rooms require often flexible pathways and “beaming around the corner”. This can be achieved by using optical fibers. Typically, these fibers are made from quartz and can be used for transmission of ultraviolet and visible radiation. Such fibers are flexible, stable and well established for application in UV-vis and Raman spectrometers.

In contrast to this the transmission of infrared radiation is not possible with quartz fibers. In infrared spectroscopy the application of fibers made from chalcogenide or silver halogenide has been established in the last years [12-14]. Although these fibers are fragile and undergo ageing with time, there are no other alternatives. Silver halogenide fibers are beneficial because they are more stable and flexible than chalcogenide fibers.

Due to their fragility, fibers cannot be applied directly in the reaction medium. Generally they are connected to probe heads which are chemically inert and mechanically stable. Typical materials for the probe shafts are stainless steel or Hastelloy™. The other end of the probe head has a lens, a prism or any other kind of optical window which is chemically inert as well. Due to that the fibers are protected from but also connected to the chemical reaction.

Typical FTIR probes have a diamond prism which acts as internal reflection element and is suitable to perform ATR spectroscopic measurements [15]. Considering the diameter area of a 1/4” or 1/8” probe head the prism has to be small. Hence, the prism is just a single reflection element which is less considering the number of reflections in conventional ATR-IR prisms.

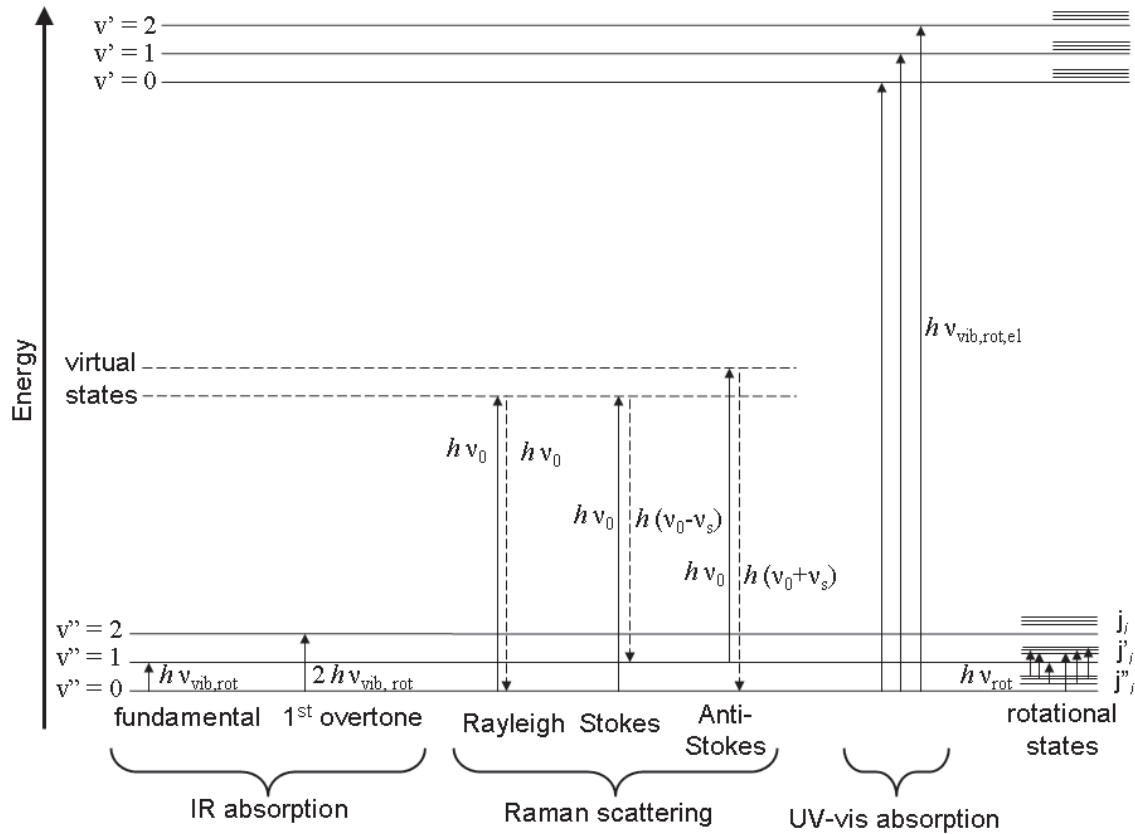
Modern Raman probes have a lens for the emission of the excitation laser at the end of the probe head. State of the art Raman spectrometers have detectors which enable the registration of Raman scattering in an angle of 180° relatively to the light source. For this reason the lens can be used for the detection of the scattered light, too. Illumination (send) and read (return) fiber can be located in parallel wires in the same cable. This setup is adequate to be used with 1/4” or 1/2” immersion probes as well as for contact-less measurements where the laser beam is focussed from outside through an optically transparent wall inside the reactor. In the latter case the focus is not directly in front of the lens but in a distinct distance and requires exact focusing on the sample with an optical bench [16].

Fiber probes for UV-vis spectroscopy are available for transmission as well as for reflection (UV-vis-DRS) spectroscopy. UV-vis transmission spectroscopy is usually applied to diluted solutions or – less common – to gaseous samples. Contrary, UV-vis-DRS spectroscopy is used for the analysis of powders and slurries. In a conventional system the illumination beam passes the sample which is stored in a transparent cuvette. A detector located on the other side receives the transmitted beam. The same principle is applied in the probes. Here the transmission probe has a gap which is filled with sample solution during the measurement. The illumination beam exits the illumination fibers, passes through the filled gap, gets reflected, passes through the gap again and is received by the read fiber. Due to the reflection the optical path is twice as the gap size. Contrary, reflection probes have no gap but an optical window. Here the probe has to be in intimate contact to the sample and the reflected light gets detected.

Nowadays the characterisation of organic and metal-organic compounds is mostly done by NMR spectroscopy, single crystal X-ray structure analysis and mass spectrometry. These methods provide information about the molecular structure of the sample in high-resolution. But as pointed out earlier the utilisation of these methods for in situ analysis is limited.

The molecular structures of organic and metal-organic compounds are mostly obtained by NMR spectroscopy and single crystal X-ray structure analysis. FTIR, Raman and UV-vis spectroscopy provide as well informations about the molecular structure but are mostly used as supplementary characterisation methods. FTIR and Raman spectroscopy is used for the observation of vibrational and rotational states of bonds between atoms and complete groups of a molecule. Especially the vibrations of functional groups like carbonyl groups are exhaustively documented. By means of respective band positions and intensities fundamental conclusions about the molecular structure are possible.

Although FTIR and Raman spectroscopy have similar scope of application, both methods provide rather complementary information. Scheme 2 shows that the transitions occurring during IR absorbance and Raman scattering are based on completely different mechanisms. This is due to the different selection rules occurring in both methods [17] (cf. Equation 1 and 2). FTIR spectroscopy requires groups with a permanent dipole moment. When the dipole moment of a certain group of a molecule or crystal is changed during its vibration, a certain amount of energy can be absorbed by this group.



Scheme 2. Schematic energy diagram of the common transitions occurring in IR, Raman and UV-vis spectroscopy referring to no special molecule; v : vibrational quantum numbers; j''_i, j''_f, j_i : rotational quantum numbers with $i = 0, 1, 2, \dots$; h : Planck constant; ν : frequency whereas: $\nu_{vib,rot} = \nu_{vib} + \nu_{rot}$, $\nu_{vib,rot,el} = \nu_{vib} + \nu_{rot} + \nu_{el}$, ν_{rot} = rotation, ν_{vib} = vibration, ν_{el} = electronic, ν_0 = excitation, ν_s = shifted emission; rotational niveaus shown for comparison; no rotational levels considered in the depictions of the vibronic transitions, no rotational and vibrational levels considered in the depictions of the electronic transitions; for the sake of clarity not all possible transitions are drawn in the scheme.

$$\frac{\partial \mu}{\partial r} \neq 0 \rightarrow IR\text{-active} \quad (1a)$$

$$\frac{\partial \alpha}{\partial r} \neq 0 \rightarrow Raman\text{-active} \quad (2a)$$

$$\frac{\partial \mu}{\partial r} = 0 \rightarrow IR\text{-inactive} \quad (1b)$$

$$\frac{\partial \alpha}{\partial r} = 0 \rightarrow Raman\text{-inactive} \quad (2b)$$

r = coordinate, μ = dipole moment, α = polarisability

Contrary, Raman spectroscopy requires groups in the molecule or crystal which can be polarised during vibration. Due to the polarisation the molecule group becomes anisotropic. If the polarised group is exposed to a laser beam, the incoming light is partly scattered at the electron shell. The major part of the scattered light is elastically scattered and has the same wavelength as the excitation light and is known as Rayleigh scattering. The rest of the incoming light is scattered inelastic and can be detected as Stokes-Raman and Anti-Stokes-Raman scattering. In this case the group interacts with a photon which causes energy transfer.

Stokes-Raman and Anti-Stokes-Raman scattering are shifted about the same amount to lower (Stokes scattering) or higher (Anti-Stokes) frequencies with respect to the Rayleigh radiation. The energy amount of the shifts is characteristic for the scattering group and can be used for structure elucidation. Usually only the Stokes scattering is used for the chemical analysis of samples with Raman spectroscopy.

As a result of the different selection rules certain vibrations of functional groups are active or inactive in IR or Raman spectra. Thus, the spectra of molecules like water or carbon monoxide show strong bands in the infrared spectra but only very weak bands in the Raman spectra. Otherwise, bands resulting from metal-non-metal vibrations can be observed well with Raman spectroscopy. The combination of both methods provides comprehensive information about the vibrational state of the sample.

While in common mid-infrared spectrometer vibrations below 400 cm^{-1} cannot be detected because the applied beam splitters are made from potassium bromide, Raman spectrometers do not have these limitations and can detect vibrations down to 100 cm^{-1} . But due to its nature Raman spectroscopy is very sensitive to fluorescence which can be emitted by the sample. Thus, the analysis of condensed aromatic systems can be perturbed by fluorescence and is difficult to perform with Raman spectroscopy [1, 3, 16].

UV-vis spectroscopy gives even less distinct information about the molecular structure than IR and Raman spectroscopy. Typically, the bands appearing in UV-vis spectra are no sharp absorption bands but rather broad band systems. This is due to the simultaneous excitation of rotational, vibrational and electronic transitions (cf. Scheme 2). This superposition of transitions causes the blurred broad bands. The fine structure arising from vibrational bands can be observed only in less common cases like in solid trans-stilbene [18] or in gaseous samples [19]. The bands appearing in UV-vis spectra are prominent for chromophores. These chromophores can be small parts of the sample molecule but in extreme case also the complete electronic shell of the sample molecule. Nevertheless, UV-vis spectroscopy is a powerful tool because it provides direct access to the electronic state of the molecules. Common UV-vis spectrometers allow to observe $\sigma \rightarrow \pi^*$, $\pi \rightarrow \pi^*$, $n \rightarrow \pi^*$, $n \rightarrow \sigma^*$, $d \rightarrow d$ and charge transfer transitions. The appearance of $\sigma \rightarrow \sigma^*$ transitions shall be neglected at this point because these transitions appear mostly beyond the detection range of common UV-vis spectrometers. Thus, the electron withdrawing or pushing effects of distinct groups in the molecule, appearance of charged molecules, interactions of lone pairs with Lewis acids and interactions of transition metals with ligands as well as with other transition metals can be observed by this method.

The previous discussion shows that there is no master method which can cover all problems. Each method has its distinct advantages and disadvantages. Hence, the coupling of methods provides the possibility to obtain a more complex picture due to the increased amount of incoming information. Several examples have shown the benefit of methods coupling up to five methods to give comprehensive insight into the respective reaction [20-23]. The coupled methods should be applied in the same reactor in order to provide a maximum of comparability of the obtained results.

2.2 In situ studies by coupled techniques

Several examples are given in literature for the application of coupled in situ spectroscopic methods in gas-phase reactions [22]. Beale et al. [23] describe the deactivation of Mo/Al₂O₃ and Mo/SiO₂ catalysts during propane dehydrogenation by coupled XAFS / Raman / UV-vis spectroscopy and O'Brian et al. [24] reported the stability of iron molybdate catalysts monitored by coupled WAXS / XANES / UV-vis spectroscopy. The reaction behaviour of molybdate catalysts during methanol oxidation [25] and the phase variation and volatilisation during the reduction of MoO₃ [26] was investigated by coupled WAXS / Raman / UV-vis spectroscopy by the same research group. Coupled Raman / UV-vis spectroscopy has been used for studies about the dehydrogenation of propane over Cr/Al₂O₃ catalysts [27-30]. In these experiments the oxidation state of the chromium species were detected by UV-vis spectroscopy and structural changes in the catalyst with Raman spectroscopy. Mechanistic investigations on dimethyl carbonate formation by oxidative carbonylation of methanol over a CuY zeolithe with a combined SSITKA / DRIFTS / MS approach has been recently published by Engeldinger et al. [31]. The adsorbates on the catalyst have been detected by DRIFTS and those which occurred in gas-phase by mass spectrometry. It was demonstrated that the utilisation of the SSITKA technique enables the discrimination between active and spectator species by comparison of the isotopic exchange rate of surface and gas-phase species. Finally, the utilisation of in situ EPR spectroscopy for the investigation of catalytic reactions was promoted in the last decade by A. Brückner [32]. A coupled EPR/ UV-vis / Raman spectroscopy / GC setup was used for the elucidation of structure reactivity relationships of V/TiO₂ catalysts in the propane dehydrogenation [2]. The presence of isolated VO²⁺ and absence of Mo⁵⁺ was observed by EPR spectroscopy, UV-vis spectroscopy showed the d-d transitions of reduced vanadium species and Mo⁶⁺-V⁴⁺ IVCT transitions, Raman spectroscopy provided information about the bond states of metal-non-metal bonds and the conversion was analysed by gas chromatography. Coupled EPR / UV-vis / Raman spectroscopy was also used

by Janke et al. [33] for the investigation of the impact of phosphorous and nitrogen on the structure and catalytic performance of VZrPON oxynitrides in the ammoxidation of 3-picoline. Also in this study EPR and UV-vis spectroscopy are used for the investigation of the change of the valence states of vanadium species and Raman spectroscopy for the analysis of metal-non-metal bonds.

So far, the previous section showed that several examples exist for the application of coupled in situ spectroscopy for the investigation of gas-phase reactions but also for the monitoring of in organic preparation processes. But, there are only a few examples of using different spectroscopic methods or combinations of them for monitoring catalysed reactions in liquid phase under unusual conditions like higher pressure or low temperatures. Mul et al. [34] studied the esterification of 1-octanol and hexanoic acid over a Nafion/silica catalyst using a ReactIR system. It was shown that the concentration profile of the esterification reaction, as determined by real-time in situ IR spectroscopy, was in qualitative and quantitative agreement with that determined by conventional off-line GC analysis.

A similar ATR system was used by Pintar et al. [35] to investigate the hydrogenation of prochiral ketones over a Pd/C catalyst in a ternary system. Their in situ analysis showed the presence of a zwitterionic form of (S)-proline which is exclusively formed under working conditions. The coupling of ATR-FTIR/Raman/UV-Vis spectroscopy for studying the oxidation of veratryl alcohol with Co(salen) in aqueous solution under oxygen pressure was described by Kervinen et al. [36]. They illustrated the need of using different types of spectroscopy for different concentration levels. The complementary methods ATR-FTIR and Raman spectroscopy were used for higher concentration levels and UV-vis spectroscopy for the lower ones. The presence of molecular oxygen in the system could be studied by UV-vis spectroscopy. Nevertheless all spectroscopic measurements have been performed only under slightly elevated pressure by using the balloon technique for inserting oxygen. While immersion probes were used for ATR-FTIR and UV-vis spectroscopic measurements, Raman spectra were recorded by focusing the laser beam on the glass reaction vessel from outside.

Investigations of heterogeneously catalysed reactions in liquid phase are also known [37-40]. Bürgi [37] studied the reaction mechanism as well as the catalyst deactivation during alcohol oxidation reactions with coupled ATR-FTIR / UV-vis spectroscopy. The adsorbates on the catalyst and species dissolved in liquid phase were studied by ATR-FTIR spectroscopy and changes in the catalyst due to treatment with oxygen and hydrogen by UV-vis spectroscopy. Caravati et al. [38] applied coupled FTIR-transmission / ATR-FTIR

spectroscopy to get spectroscopic insights into the oxidation of benzyl alcohol. Here, they characterised the working catalyst immobilised on the ATR-crystal by ATR-FTIR spectroscopy and the conversion and product formation in liquid phase by transmission FTIR spectroscopy. In our group coupled EPR / Raman spectroscopy was used for the elucidation of the state of the $\text{Fe}_3(\text{CO})_{12}$ catalyst during the photocatalytic water reduction [39]. Another example from our group is the application of coupled ATR-FTIR / UV-vis / Raman spectroscopy to monitor the hydrogenation of imines [40].

Coupled in situ spectroscopic methods have also been applied for monitoring non-catalysed chemical reactions like catalyst preparations or polymerisation reactions. The monitoring of preparation processes for the synthesis of heterogeneous catalysts was described, for instance, by Kongmark et al. [41], Bentrup et al. [21] and Radnik et al. [42]. Kongmark et al. [41] showed the presence of different steps in the crystal growth of Bi_2MoO_6 by coupled XRD / XANES / Raman spectroscopy. Bentrup et al. [21] monitored a molybdate-based catalyst precursor synthesis by coupled WAXS / SAXS / Raman / ATR-FTIR / UV-vis spectroscopy. SAXS provided information about the particle size and shape and WAXS about occurring crystalline phases. UV-vis spectroscopy showed the charge transfer bands of $\text{Mo}^{6+}\text{-O}$ and $\text{Fe}^{3+}\text{-O}$ species, ATR-FTIR spectroscopy gave information about the nature of phosphate species and Raman spectroscopy showed the formation and changes of different molybdate phases. Radnik et al. [42] investigated the crystallisation process of solid catalysts from salt solutions in levitated droplets trapped in an ultra-sonic trap by synchrotron X-ray diffraction coupled with Raman spectroscopy in order to obtain deeper insight into processes which occur during spray-drying.

Examples for the reaction monitoring in organic chemistry are published by Quinebécche et al. [43] and Tolstoy et al. [44]. Quinebécche [43] determined kinetic parameters of the anionic copolymerisation of styrene and isoprene by means of coupled mid-IR and UV-vis spectroscopy which enables simultaneous measurements of the concentrations of monomers and active species in the anionic (co)polymerisation of above mentioned monomers. Tolstoy et al. [44] studied the geometries of strong hydrogen bonds of phenols with carboxylic acids using coupled UV-vis/NMR spectroscopy.

Considering all previously mentioned examples, the current state of the art of coupled in situ techniques can be summarised as follows:

1. The major field of research is the investigation of gas-phase reactions. These investigations focus mainly on the state of the working catalyst. Product analysis is usually performed by gas chromatography or mass spectrometry.
2. The investigation of catalytic reactions in liquid phase systems is focused on the utilisation of in situ ATR-FTIR spectroscopy. Coupled techniques are especially used in liquid phase systems for the monitoring of preparation processes where mainly the syntheses of solid inorganic catalysts were investigated. Only few examples exist for the monitoring of organic processes in liquid phase.
3. In situ investigations of pressure reactions are still less common. Especially the application of three different spectroscopic methods in the same reactor by utilising immersion probes has rarely performed.
4. Investigations at lower temperatures ($\approx -60^{\circ}\text{C}$) with coupled optical in situ spectroscopy have not been performed yet.

The current thesis will bridge these gaps. Organic preparation processes at low temperature as well as heterogeneous catalysed reactions in liquid phase under pressure will be analysed in situ by coupled ATR-FTIR / UV-vis / Raman spectroscopy using respective immersion probes.

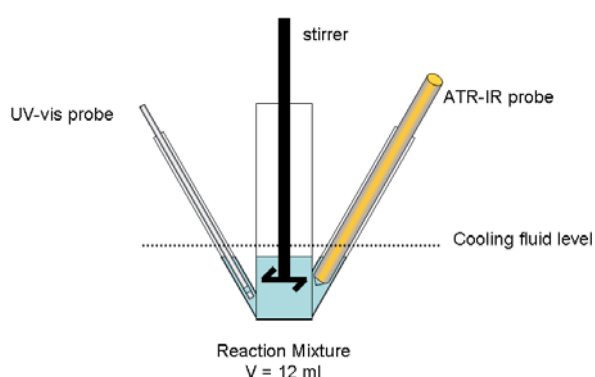


3. Technical Part

3.1 Development a reaction cell for the in situ investigations of low-temperature preparation processes

In order to enable in situ investigations a novel reaction cell has to be developed. The required features are inert atmosphere (no presence of moisture and air), small reaction volume, implementation of at least two probes considering the limited flexibility of the ATR-FTIR probe, cooling to -70°C by cooling bath of a cryostat, facilities for dosing reagents and sample taking during reaction and stirring.

The resulting design of the cell is shown in Scheme 3 and in Figure 3. The cell material is glass which is chemically inert and provides adequate stability with minimal thermal expansion / contraction. Adhesive water can be removed easily by heating the cell under argon flow when no probes are installed. In case of installed probes the thermal limit of the cell is determined by the limit of the probes. In this case no temperatures above $+70^{\circ}\text{C}$ should be applied (thermal limit of the UV-vis probe). Considering these limitations, working under semi-water-free is possible.



Scheme 3. Scheme of the reaction unit.



Figure 3. Picture of the reaction unit.

The lower temperature limit is determined by the probes as well. The lower limit of the UV-vis-Probe is 0°C whereas the limit of the ATR-FTIR probe is -100°C . Typically the glue inside the probes which fix the fibers to the crystal is the weakest part of the construction. Sudden cooling embrittles the glue but cooling down slowly by cryostat instead of sudden cooling - like using a bath filled with solid CO_2 and ethanol - does not weak the glue connection that much.

Due to the need to use a cryostat, no conventional stirring with a magnetic stirring bar and a stirring plate was possible. The distance between stirring in bar inside the reactor and the stirring plate below the cooling bath would be too large because of the cryostat. Due to this fact the application of an overhead stirrer becomes necessary. As a matter of stability the

shaft of the stirrer requires a certain diameter as well as the flanges needs a minimum of space for proper stirring. Considering these requirements the diameter of the complete reactor becomes relatively large which determines the size of the reaction volume.

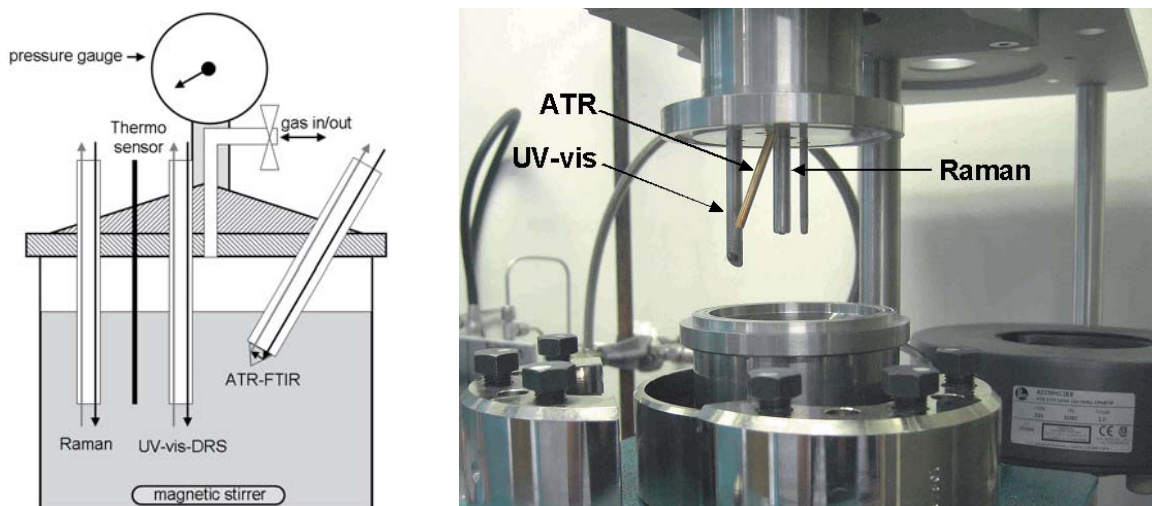
The remaining cell design was determined by the implementation of the probes. For in-line monitoring the probes should immerse deeply in the reactor without getting too close to the stirrer which consists the danger of damage. The implementation of additional side tubes at the bottom of the reactor proved to be the best design. The required minimal reaction volume is smaller than in case of all other designs where the probes are immersed from above. Additionally the probes are safe of damage due to rotating stirrer flanges because the probes are not immersing directly the reactor room. Disadvantageous are increased mass-transfer limitation due to the more complex geometry as well as the effect of communicating vessels referring to the side tubes. The latter effect becomes important when liquid reagents are added to the reaction mixture during the reaction or when gas occurs as reaction product.

The reactor has two side tubes with 4mm and two with 8 mm inner diameter, respectively. This enables the possibility to use the 3mm and 6 mm ATR-FTIR probes manufactured by ifs, as well as the opportunity using the Micro-UV-vis transmission probes and standard UV-vis reflection probes from Avantes. Also the 1/4" Raman probe supplied by Kaiser Optical Systems or every other probe with a diameter of 1/8" or 1/4" can be implemented in this reactor in general. Alternatively a hose with gas supply (inert gas as well as reactive gas) can be connected to the side tubes. All side tubes are inclined about 30° relatively to the reactor main tube and are adequate for sample taking for ex situ analysis by using a syringe. Due to the inclination the probes can be installed more easily because of a decreased curvature of the fibers. The inner diameter of the tubes is larger than the probes. This prevents from canting during implementation of the probes in the side tubes.

Finally the problem of sealing has to be solved. The overhead stirrer is connected due to a Teflon tube which fits air-tight around the stirrer's pole and the tube is connected via a grinding to the reactor. Neither the side tubes nor the probes or hoses contain any grindings. But the reactor has to be air- and moisture-tight under normal pressure only for a couple of hours. This can be achieved by the application of Teflon tape for fittings and plugs. Therefore Teflon tape is wrapped around the probe or house until the diameter is slightly above the inner diameter of the side tube where the probe should be installed. During the implementation of the probe the Teflon tape befalls plastic deformation which provokes that the connection fits tight enough into the tube. Plugs can be made and installed by using the same concept.

3.2 Development a reaction cell for the in situ investigations of pressure reactions in multiphase systems

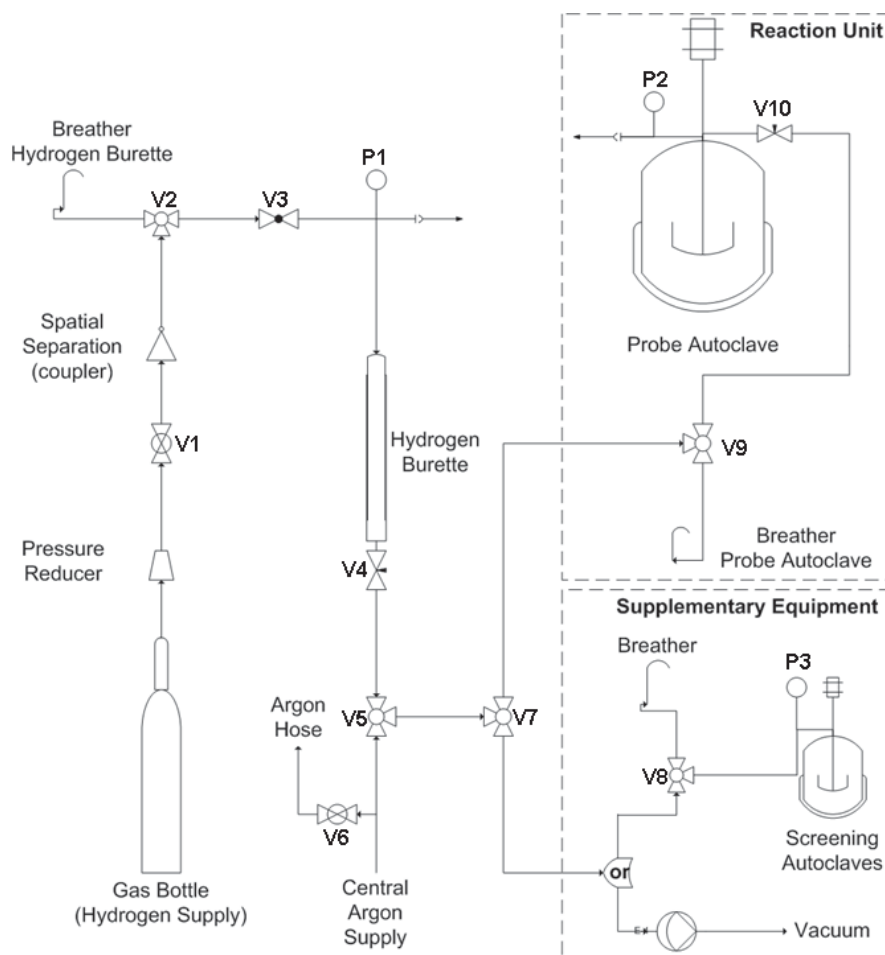
For the monitoring of pressure reactions by simultaneous ATR-FTIR, UV-vis and Raman spectroscopy a special autoclave (reaction unit) has to be developed which resists pressures up to 20 bar at 100°C. The reaction unit comprises a special customised autoclave, shown in Scheme 4 and Figure 4 and a hydrogen burette for gas dosing which are manufactured by Parr Instrument Co. (Illinois, USA).



Scheme 4 (left) and Figure 4 (right). The modified autoclave (Parr) with fiber-optical probes implemented in the cover plate for simultaneous Raman/ATR/UV-vis measurements during hydrogenation reaction under pressure.

The autoclave cover plate is fixed into a frame while the autoclave vessel can be removed easily for filling, emptying or cleaning procedures. The autoclave has a total volume of 100 mL. For experimental use the liquid phase should be 40 – 50 mL. More than 50 mL would be above the security limit of the autoclave and below 40 mL the probes would not dip into the liquid phase. In order to get space for the implementation of the probes the cooling loop line, the overhead stirrer and the gas outlet valve of a standard autoclave have been removed. Therefore, three flanges for probes with a diameter of 1/8", 1/4" and 3/8" are installed in the cover plate of the autoclave. While the 1/4" and the 3/8" flanges are installed vertically, the 1/8"-flange has an inclination of 30° referring to the vertical axis. This is made for a more easy installation of 3 mm-ATR-FTIR probes. The 3/8" flange can be converted into an 8 mm, a 6 mm or a second 1/4" flange by changing the tubing-to-NPT thread adapter. Because of the displacement of the overhead stirrer the stirring has to be performed by a magnetic stirring bar. The stirring rate can be set with a digital stirring rate in good reproducibility. This is important because the stirring rate has fundamental effect on the reaction rate of gas-liquid or gas-liquid-solid reactions referring to mass transport from the gas to the liquid phase [45]. The heating is done by a heating sleeve which surrounds the lower part of the reactor. Due to

the removal of the cooling loop line the heating has to be performed carefully and slowly to prevent overshooting of temperature. After displacement of the gas-outlet valve the complete gas dosing is realised via the remaining gas-inlet valve. Hence, the autoclave cannot be flushed with gas. A gas exchange can be achieved by alternating dosing and realising of the gas. This technique is often used as well on simple autoclaves which have one valve for gas supply.



Scheme 5. Piping and instrumentation diagram of the setup used for the in situ analysis of pressure reactions.

The gas supply is realised via a hydrogen burette (cf. Scheme 5) because a high-pressure gas supply system was not installed in the laboratory where the autoclaves and the spectrometers are located. Thence, a standard gas cylinder was equipped with a pressure reducer which is able to reduce the gas pressure from 0-200 bar inside the cylinder to 0-55 bar behind the pressure reducer. A gas line has been installed from the gas cabinet to the fumehood which stores the hydrogen burette and the probe autoclave. Outside the fumehood the line has got an outer diameter of 8 mm while all other lines have an outer diameter of 1/8". The smaller diameter enables bending of tubes with less power, smaller bending radii can be selected and as most important merit the dead-volume is small. Inside the fumehood the line is secured with a lock valve and with a spatial separation realised by a quick-connecting coupler with a

gas lock. Usually the line from the bottle cabinet to the hydrogen burette inside the fumehood is without pressure, the lock valve is closed and the quick-connecting coupler is disconnected. This safeguards that in case of a major malfunction only hydrogen stored inside the fumehood may react while the hydrogen gas cylinder which contains the major amount of hydrogen is still safe. A direct connection from the gas cylinder to the hydrogen burette is only required when the burette has to be refilled. This occurs only when no reaction takes place in the autoclave. The autoclaves can be filled from the burette which has a volume of 0.5 L and can hold up to a pressure of 5000 psi (~345 bar). The line between the coupler and the hydrogen burette as well as the line from the hydrogen burette to the autoclave have a breather each which allows the pressure realise in the complete unit where no pressure is required any more. This provides the possibility to reduce the amount of hydrogen inside the reaction unit to a minimum. Both breathers are extended by tubes which are laid into the flue. This provides that blowed off gas does not have to pass the complete fumehood room and drained off directly. The reaction unit is additionally connected to the central argon supply which provides argon with a pressure of maximal 10 bar which is enough for flushing the reaction unit with inert gas. The probe autoclave can be closed in argon counter current if the reaction is sensitive to air or moisture. With another valve the argon can be directed into a flexible PTFE hose, hence vessels can be flushed with argon before or after the experiment. The hydrogen and argon supply are designed primary to be used with the probe autoclave. But the construction also allows the supply of other reactors with gas. For screening experiments without in situ monitoring, simple autoclaves (Carl Roth Model 1) with a volume of 100 mL have been used parallel to the probe autoclave. Alternatively a vacuum pump can be installed at this place which can be used for cleaning the hydrogen burette. This becomes necessary when another gas shall be applied instead of hydrogen. The reaction unit including the gauges are stable enough to resist to a low pressure produced by a membrane pump which is about 1-5 mbar.

The hydrogen burette and the probe autoclave contain burst discs for security reasons. The operating limits of the autoclave are 100 bar and 350°C and 5000 psi (~345 bar) in case of the hydrogen burette. But both apparatus will be operated far below these limits. The pressure inside the hydrogen burette is determined by the maximum pressure behind the pressure reducer of the gas bottle which is 55 bar in this case. The operation limits of the autoclave are determined by the used probes and fittings. For this reason the autoclave with installed probes has never been used at pressures above 25 bar at 80°C. A test with a similar construction showed that 120°C at 20 bar are possible with 6 mm probes. However, the

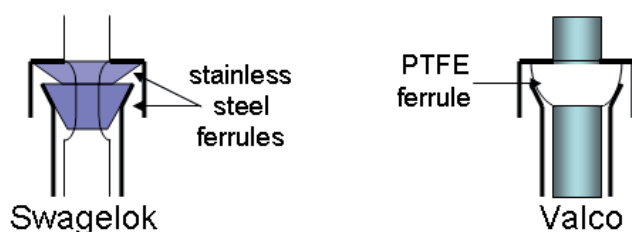
chance that the burst discs or pressure vessels will explode under the applied conditions is small. The most possible source of uncontrolled pressure release is a vertical ejection of the installed probes. The risk of injuries due to in all direction scattered fragments is small under these circumstances.

The installation of the probes is determined by two considerations: stability of the probes versus fitting of the probes.

The safest method would be the utilisation of standard stainless steel Swagelok™ ferrules for tube connections. These ferrules are adequate to connect tubes tight up to pressures of 300 bar and higher. But the conception of these Swagelok™ ferrules is based on the deformation of the tube at the point of the fitting. Due to this a fraction of the fragile probes during the installation of the fittings cannot be excluded. Additionally removing the fittings is difficult and a lateral contraction of the probe remains after removing.

A second method for fixing the probes would be the use of Swagelok™ Ultratorr or Ultratorr-type fittings. These fittings were developed to fix tubes deformation free in vacuum units. Instead of the probe an O-ring is deformed when the screw-nut is tightened. However, these fittings are developed for vacuum applications and not utilisation in pressure reaction units.

The third method is the replacement of the stainless steel Swagelok ferrules against ferrules made from softer materials. These ferrules do not deform the probe and the fitting occurs via the self-deformation (cf. Scheme 6 and Figure 5). Typical materials are polymers like PEEK, Nylon, Vespel or PTFE. For targeted tuning of the material properties the polymers can be filled with glass or graphite for instance.



Scheme 6. Principles of fitting.

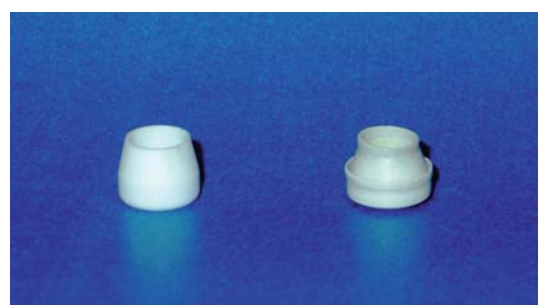


Figure 5. New (left) and deformed (right) Valco ferrules.

For the implementation of the probes glass-filled PTFE ferrules from Valco were selected. These ferrules are chemically inert, soft, but mechanically more stable than non-filled PTFE ferrules. The drawback is that PTFE tubing is relatively porous, and compounds of low molecular weight like hydrogen can diffuse through the tubing wall. On the other hand this

material is so soft that even when the screw-nut is tightened with higher torques, a deformation of the probe is not likely. Furthermore, the standard fittings between top and bottom of the probe autoclave and of the screening autoclaves are made from PTFE as well.

Due to the lack of deformation, the probes fit by friction only. Therefore, the probes have to be safeguarded by additional clamps which prevent the probes from outshooting from the autoclave. This danger increases with increasing diameter of the probes. Due to this increasing of pressure inside the autoclave should be carried out slowly during experiments. If the applied pressure is higher than 15 bar the stands of the clamps should be secured extra. It is possible that the UV-vis-transmission probe which has a diameter of 8 mm can be pressed out of the autoclave at 24 bar, even when the security clamp is fixed to a stand with a standard basis (weight 2.5 kg).

Another advantage is the greater flexibility if self-deforming ferrules are used. The installation of probes is often difficult in the narrow ambience. Especially the ATR-FTIR probe is endangered because of the exposed diamond prism and the gold coating which must not be damaged. Here it is advantageous to install probes which have a diameter of 3 mm in a 1/8" slot and probe with a diameter of 6 mm in a 1/4" slot respectively. The little difference is big enough for improving the lead-in but still narrow enough to fit tight. Additionally 6 mm (ATR-FTIR, UV-vis-DRS and UV-vis-transmission probes) and 1/4" probes (Raman probe) can be implemented in the same slot without any changes. The feasibility of this has been tested also under reaction conditions with stainless steel dummy probes before the real probes were implemented in the autoclave.

It has to be mentioned that the probes could not be installed gas-tight in all cases although the same installation procedure has been applied. Amongst the Valco ferrules 6 mm-Swagelok PTFE and Nylon ferrules have been tested. Nylon is known to be harder than PTFE but a significant improvement could not be observed. The same result was obtained when 6 mm-Swagelok PTFE ferrules instead of 1/4" glass-filled PTFE ferrules from Valco were applied. However, no problems occurred when the tests were done with Argon, CO or a CO/Helium-mixture. Thus, the emission of hydrogen is an effect of the small size of the molecules. But considering the application of the probes in the autoclave, this problem can be negotiated because the amount of released hydrogen is very small. Furthermore the autoclave is operated in a fumehood where the air is exchanged with 600 m³/h consecutively. Hence, the hydrogen is conveyed and diluted very fast. The screening experiments showed that the reaction was mostly finished after 90 minutes under the applied conditions. Consequently, even if a pressure drop of 1 bar hydrogen per hour occurs, the remaining amount of hydrogen

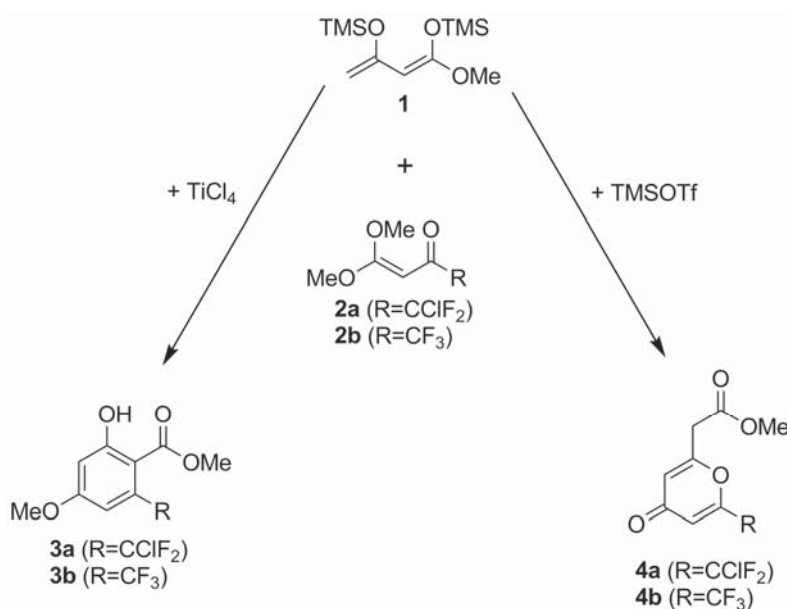
inside the autoclave is still great enough that the reaction works properly, when the starting pressure was set to 20 bar. Based on these considerations the autoclave was defined as leak-proof when the pressure drop was 1 bar per hour at room temperature when a pressure of 20 bar was set as starting pressure and the autoclave was not loaded with reagents or solvents. Using this definition it is possible to perform in situ investigations of pressure reactions in a proper way. However, a kinetic analysis cannot be made under these conditions and require a well-tempered and leak-proof reactor.

For the sake of completeness it has to be mentioned that due to the application of fiber optics all applied spectrometers are located outside the fumehood. This is advantageous because the spectrometers are in a protected place referring to malfunctions and exposition to chemicals, and finally the monitoring and operation of the spectrometers is more easy and comfortable for the operator. For the technical realisation two holes had to be drilled into one sidewall of the fumehood because of the limited flexibility and range of the ATR-FTIR and Raman fiber optics. The holes are small enough that the air exchange of the fumehood is not decreased.

4. Elucidating the directing effect of the used Lewis acid on the reaction pathway in formal [3+3] cyclocondensation reactions

Trifluoromethyl-substituted arenes and hetarenes are interesting substrates in medicinal chemistry [46-52]. Although the size of CH₃ and CF₃ groups are similar, the high electronegativity of the latter significantly changes reactivity and polarity. Thus, CF₃-substituted molecules allow a better transport of the drug in vivo which may be important in drug-receptor interactions. Otherwise, highly fluorinated arenes show an excellent solubility in fluorophilic solvents. This makes them to excellent ligands for catalytic reactions in fluorous biphasic systems and to useful organocatalysts [53-63].

One possibility to synthesise such small molecules are formal [3 + 3] cyclisations of 1,3-bis(silyloxy)-1,3-butadienes with 4-ethoxy-1,1,1-trifluoroalk-3-en-2-ones which lead to the formation of CF₃-substituted salicylates [64-67]. Recently, a Lewis acid-mediated cyclocondensation reaction was reported (cf. Scheme 7) showing the influence of the Lewis acid on the product distribution [68, 69]. The formal [3+3] cyclisation of 1,3-bis(silyloxy)-1,3-butadiene **1** with ketenacetals **2a,b** leads, depending on the choice of the Lewis acid, to the formation of salicylates **3a,b** (use of TiCl₄) or of pyran-4-ones **4a,b** (use of TMSOTf).



Scheme 7. General reaction scheme.

The reason for the influence of the type of Lewis acid on the product distribution has been unclear to date. Thus, coupled in situ spectroscopy shall be applied to elucidate the reaction mechanism. A similar reaction comprising the condensation of dialkyl- β -esters with several aldehydes promoted by TiCl₄ was studied by Marrone et al. [68]. For a comprehensive study

of the possible mechanism and the pivotal role of Ti^{4+} in this reaction DFT approaches and spectroscopic methods as NMR, IR and UV-vis were applied. In this study combined ATR-FTIR, UV-vis and Raman spectroscopy supported by X-ray single crystal structure analysis will be used for the investigations of the reaction mechanisms.

Up to now, the reactants are not characterised adequate enough with ATR-FTIR, UV-vis or Raman spectroscopy. Hence, the investigation started with the ex situ characterisation of single compounds and mixtures auf reactants with the acids in order to achieve a basis for the further in situ studies.

4.1 The ex situ studies at room temperature

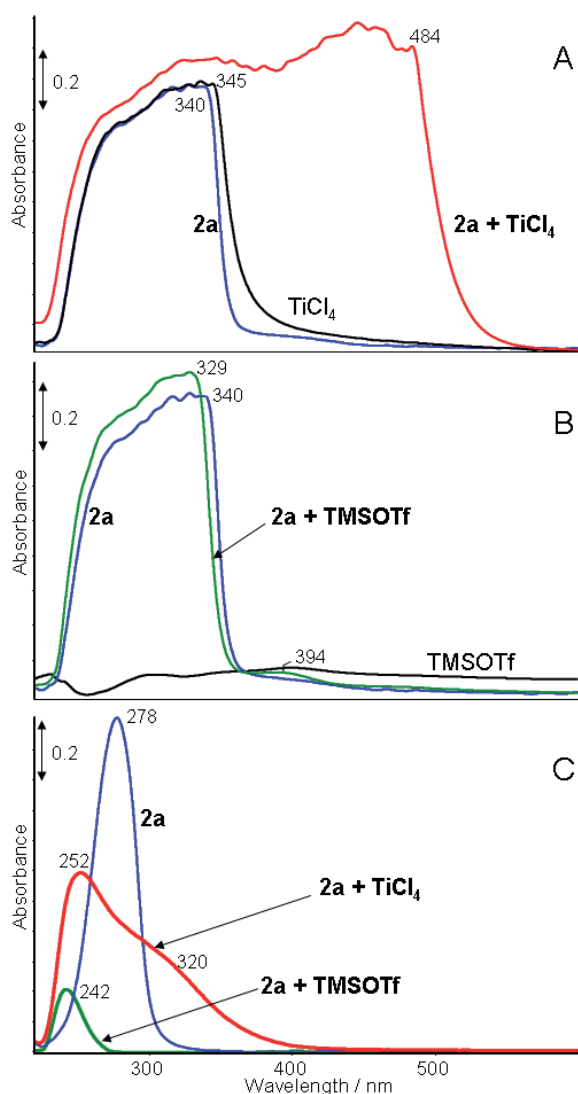


Figure 6. UV-vis spectra of (A) **2a**, TiCl_4 , and **2a** + TiCl_4 in CH_2Cl_2 at $c=0.5 \text{ mol}\cdot\text{L}^{-1}$; (B) **2a**, TMSOTf, and **2a** + TMSOTf in CH_2Cl_2 at $c=0.5 \text{ mol}\cdot\text{L}^{-1}$; (C) **2a**, TiCl_4 , **2a** + TiCl_4 , and **2a** + TMSOTf in CH_2Cl_2 at $c=5\cdot 10^{-4} \text{ mol}\cdot\text{L}^{-1}$.

First of all the interaction of the Lewis acids TiCl_4 and TMSOTf with the ketenacetale **2a** was exemplarily studied. The measurements were done at room temperature. Normally, the used concentrations of all samples was $0.5 \text{ mol}\cdot\text{L}^{-1}$ which is in the same order of magnitude as the starting concentrations of the reaction mixture.

The UV-vis spectra obtained from the pure Lewis acids, the ketenacetale **2a** and mixtures of them are shown in Figure 6 (A, B). The spectrum of the ketenacetale **2a** contains a broad band with an absorption edge at 340 nm. The spectrum of TiCl_4 is rather similar with an absorption edge at 345 nm, while TMSOTf is nearly UV-vis inactive. The UV-vis spectrum of the ketenacetale **2a**/ TiCl_4 mixture (molar ratio 1:1) shows a strong shift to longer wavelengths and the absorption edge is located at 484 nm. Contrary to this the mixture with TMSOTf shows a small shift to shorter wavelengths with an absorption edge

The spectrum of proposed compound **6** shows a broad band with maximum at 252 nm and a shoulder at 320 nm (Figure 6C). The band intensity is decreased again but to a lower extent as detected for the proposed compound **5a**. The shift to shorter wavelengths from 278 to 252 nm indicates an attack of the carbonyl group by TiCl_4 . Obviously, TiCl_4 interacts with the ketenacetale via a second site which would explain the observed shoulder at 320 nm. It is likely that an attack at one of the methoxy group causes an increase of the electron density in the C–O bond by electron delocalisation so that this group becomes UV-vis active. This suggests that TiCl_4 is attacked by the ketenacetale at two sites. As a result of electron delocalisation the carbonyl group loses UV-vis activity, but a new transition assigned to one of the methoxy groups becomes shifted and, thus, observable in the UV-vis spectrum. The nature of this spectrum which shows bands at 252 and 320 nm is similar to the UV-vis spectrum of $\text{Ti}(\text{acac})\text{Cl}_2$ reported by Schmidtke and Voets [71]. The shape of the transitions was described as predominantly $\pi \rightarrow \pi^*$. Other transitions like charge transfer or $n \rightarrow \pi^*$ are not predominant and contribute only to a low extent to the spectrum. In $\text{Ti}(\text{acac})\text{Cl}_2$ electron delocalisation is present, too. The degree of delocalised π -electrons directly effects the splitting of $\pi \rightarrow \pi^*$ transitions into several components.

In order to verify the results of the UV-vis spectroscopic investigations the same samples were studied by ATR-FTIR spectroscopy (cf. Figure 7). The ATR-FTIR spectrum of the ketenacetale **2a** shows some characteristic vibrations which are important for the discussion. According to the work of Dabrowski and Tencer [72], the band in the spectrum of the ketenacetale **2a** at 1688 cm^{-1} can be assigned to $\nu(\text{C}=\text{O})$ and the band at 1554 cm^{-1} to $\nu(\text{C}=\text{C})$. The bands at 1484 and 1391 cm^{-1} can be related to $\delta_{\text{as}}(\text{CH}_3)$ and $\delta_{\text{s}}(\text{CH}_3)$ of the methoxy groups, the band at 1437 cm^{-1} to $\delta(\text{=CH})$ of the methylene group.

Mixing the ketenacetale with TMSOTf effects that the $\nu(\text{C}=\text{O})$ band is nearly vanished. In return, five weak bands between 1773 cm^{-1} and 1648 cm^{-1} appear. According to the proposed mechanism of Bunescu et al. [7] the TMS^+ cation interacts with the carbonyl group which would cause the loss of the original C=O vibration. The appearance of five new bands indicates that possibly more than one intermediate product is formed. As can be seen from Figure 7, the $\nu(\text{C}=\text{C})$ vibration of the ketenacetale is nearly vanished by interaction with TMSOTf. Only a very weak band at 1557 cm^{-1} remains. The $\delta_{\text{as}}(\text{CH}_3)$ and $\delta(\text{=CH})$ bands are shifted to lower wavenumbers and the intensity of the $\delta_{\text{as}}(\text{CH}_3)$ vibration decreases dramatically. The $\delta_{\text{s}}(\text{CH}_3)$ at 1391 cm^{-1} band is nearly completely vanished or overlaid by other bands. Obviously, the loss of the C=C double bond influences the neighboured groups

and causes a shift of respective bands to lower wavenumbers. These observed changes in the spectrum of the mixture **2a** + TMSOTf confirm the proposed mechanism [7] assuming the loss of the C=C double bond by introducing the positive charge from TMSOTf to the ketenacetal by reaction. On the other hand, a loss of a methoxy group during the reaction with TMSOTf cannot be excluded.

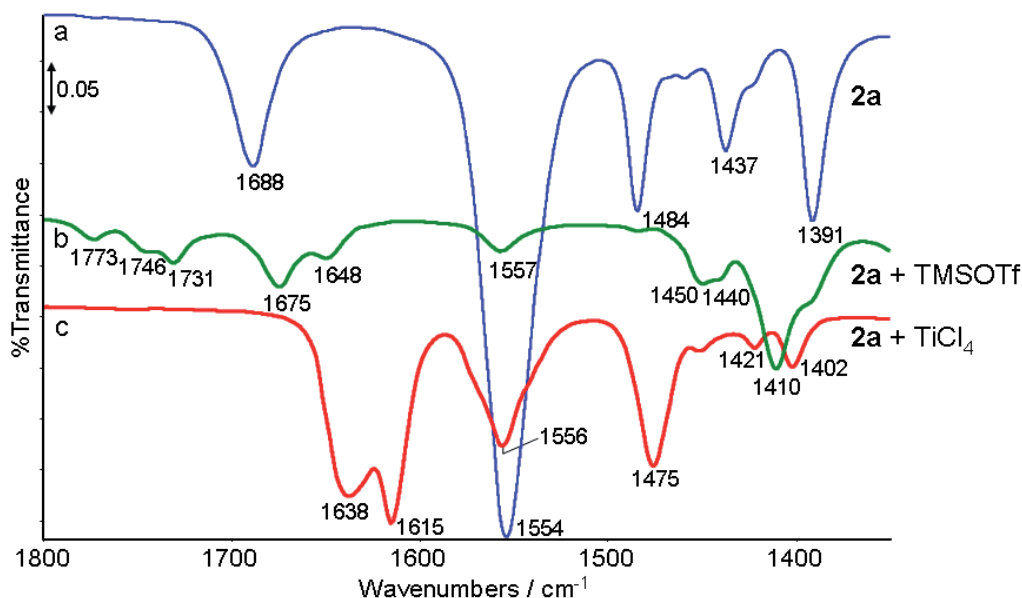


Figure 7. ATR-FTIR spectra of **2a** (a), **2a** + TMSOTf (b), and **2a** + TiCl₄ (c) in CH₂Cl₂ at $c=0.5 \text{ mol}\cdot\text{L}^{-1}$.

The ATR-FTIR spectrum of the mixture **2a** + TiCl₄ shows intensive bands with maxima at 1638 cm⁻¹ and 1615 cm⁻¹ which can be assigned to vibrations of carbonyl-like species. Shape and position of the bands lead to the conclusion that a metal chelate is present which means that titanium coordinates the carbonyl group. The band intensity is higher than that of the respective $\nu(\text{C}=\text{O})$ vibration of the ketenacetal **2a**. The formed chelate species should be similar to metal chelate complexes which are known from β -diketones [73]. Characteristically, the $\nu(\text{C}=\text{O})$ and the $\nu(\text{C}=\text{C})$ vibrations are strongly coupled with each other. The $\nu(\text{C}=\text{C})$ vibration of **6** appears at 1556 cm⁻¹ which is only a slight shift compared with the $\nu(\text{C}=\text{C})$ vibration of the ketenacetal **2a**, but its intensity is drastically decreased. Finally, additional bands at 493 cm⁻¹ with a shoulder at 474 cm⁻¹ and 414 cm⁻¹ with a shoulder at 438 cm⁻¹ were observed in the spectrum of the mixture **2a** + TiCl₄ (not shown in Figure 7) which result from $\nu(\text{Ti}-\text{O})$ vibrations, respectively [74].

Raman spectroscopy is a suitable method for the investigation of metal-halogen and metal-oxygen vibrations. Therefore, solutions of TiCl₄ and of the mixture TiCl₄ + **2a** were investigated by Raman spectroscopy, too. The spectra, including those of the solvent CH₂Cl₂ and of the pure ketenacetal **2a** in CH₂Cl₂, are displayed in Figure 8.

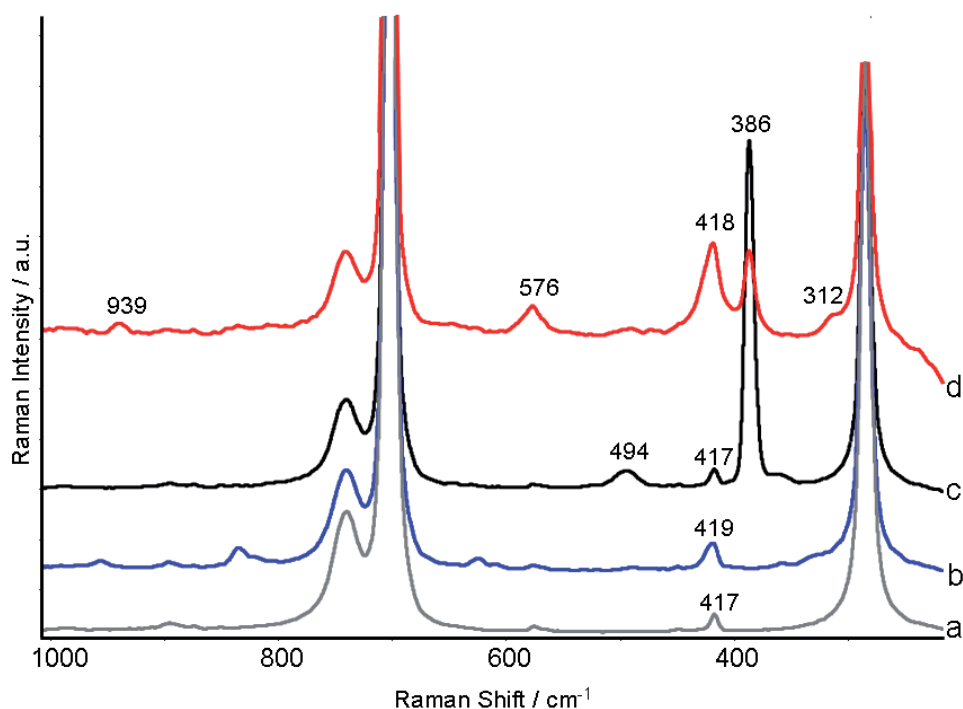


Figure 8. Raman spectra of pure CH_2Cl_2 (a), **2a** (b), TiCl_4 (c), **2a** + TiCl_4 (d) in CH_2Cl_2 at $c=0.5 \text{ mol}\cdot\text{L}^{-1}$.

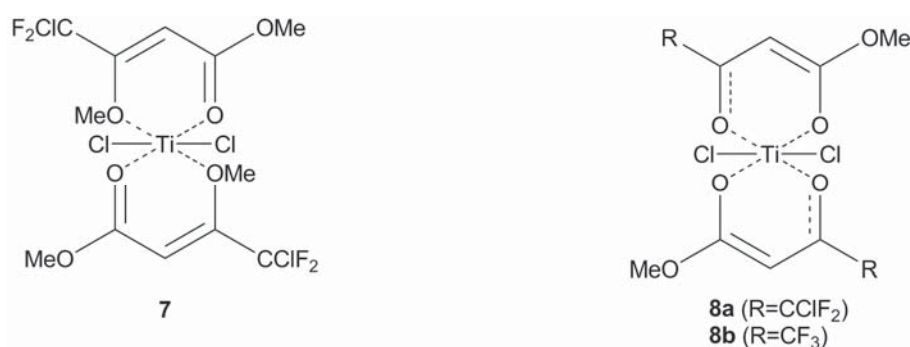
The solvent CH_2Cl_2 is nearly Raman-inactive in this region. Only one weak signal at 417 cm^{-1} appears. According to the work of Trumpy [75] and Escibano et al. [76] this signal is not prominent for a native vibration mode of CH_2Cl_2 . This band might root from a stabilising agent which was presumably added by the manufacturer. The dissolved ketenacetale is also nearly Raman-inactive. A weak signal appears at 419 cm^{-1} which might partly overlap with the weak signal of the solvent. This signal can be dedicated to skeletal vibrations of the ketenacetale.

The spectrum of TiCl_4 shows two bands: one weak band at 494 cm^{-1} and one strong band at 386 cm^{-1} which can be assigned as the ν_3 (weak) and ν_1 (strong) vibration of TiCl_4 [77]. The 1:1-mixture of ketenacetale **2a** and TiCl_4 shows some interesting changes in the Raman spectrum. The intensity of the ν_1 vibration mode is drastically reduced and slightly shifted to 386 cm^{-1} . This finding points to a possible loss of chloride anions due to coordination of TiCl_4 by the ketenacetale and is confirmed by the appearance of a new band at 418 cm^{-1} which should be prominent for a TiCl_2 -species with two additional coordination partners. The latter are certainly the oxygen atoms of the ketenacetale. The new band at 576 cm^{-1} might be prominent for a Ti-O-C vibration mode. Both assignments are based on the work of Dehnicke [78] who studied Titanium(IV)oxochloride. This study was performed in the solid state and the author observed a broad vibration band at 430 cm^{-1} in the IR spectrum which was assigned to $\nu(\text{Ti-Cl})$. He also measured the spectrum of $\text{TiOCl}_2\cdot\text{POCl}_3$ in which two bands at 402 cm^{-1} and 422 cm^{-1} appear. Due to the fact that the $\delta(\text{P=O})$ vibration appears

in this area as well, Dehnicke did not exactly assign these bands. But it seems to be possible that the coordination of additional oxygen atoms might lower the wavenumber of the $\nu(\text{Ti}-\text{Cl})$. Thus, the observed vibration at 422 cm^{-1} could refer to $\nu(\text{Ti}-\text{Cl})$ of this compound which would support the assignments done in the current study. Finally, the presence of a TiCl_3 species can be excluded. Neither α - nor β - TiCl_3 exhibit any bands around 418 cm^{-1} [79, 80]. The observed band at 939 cm^{-1} (Figure 8) can be assigned as $\nu(\text{Ti}-\text{O}=\text{C})$ [64].

It is peculiar that the ν_1 vibration mode of TiCl_4 at 386 cm^{-1} is not vanished completely in the 1:1-mixture of **2a** and TiCl_4 . Titanium is known to be able to form octahedral complexes [81]. When TiCl_4 would react with both oxygen atoms of one ketenacetale molecule the intensity of the ν_1 vibration mode should not decrease in such a drastic manner. However, if one TiCl_4 molecule would react with two ketenacetale molecules, it would be necessary to release two chloride anions. The formation of a chelate complex containing two ketenacetale molecules like **7** (cf. Scheme 9) would be a suitable explanation for the differing band intensities. This assumption can be supported by the observed band at 312 cm^{-1} in the spectrum of the **2a** + TiCl_4 mixture (cf. Figure 8). According to Badiger et al. [74] this band only appears in octahedral complexes.

The same measurements have been carried out with TMSOTf and a mixture of TMSOTf and ketenacetale **2a**. However, due to the strong fluorescence emission of TMSOTf, no satisfactory spectral data could be obtained.

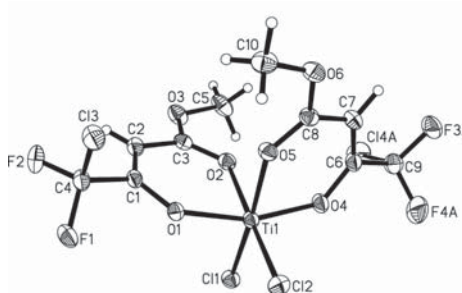


Scheme 9. Structures of the titanium bis-chelate complexes: according to spectroscopic findings (for **7**) and according to a X-ray crystal structure analysis (for **8a**, **8b**).

Single crystals of the bis-chelate complex **8a** could be isolated. Selected bond lengths and angles are given in Table 1. First of all, the molecular crystal structure shows that indeed a chelate complex has been formed. The titanium atom is coordinated by two oxygen atoms of the chelate ligand. Furthermore it is clearly seen that a species including more than one ketenacetale molecule as ligand is formed as already concluded from the spectroscopic

findings. The coordination geometry is distorted octahedral where the chlorine ligands are arranged in cis-configuration. The character of the bonds in the O1-C1-C2-C3-O2 unit, as well as in the O4-C6-C7-C8-O5 unit changes due to complexation with TiCl₄ compared to the starting material **2a** which reflect the activating effect of the TiCl₄ on the ketenacetale. Surprisingly, it is also observed that each ketenacetale molecule has lost one methyl group.

Table 1. Selected bond lengths [Å] and angles [°] in bis-chelate complex **8a**.

Ti1–O1	1.9088(12)	Ti1–O4	1.8826(12)	
Ti1–O2	2.0652(13)	Ti1–O5	2.0677(12)	
C1–O1	1.301(2)	C6–O4	1.308(2)	
C3–O2	1.246(2)	C8–O5	1.242(2)	
C2–C1	1.344(3)	C7–C6	1.338(2)	
C2–C3	1.429(3)	C7–C8	1.438(3)	
04–Ti1–O5	83.50(5)	01–Ti1–Cl1	96.70(4)	
02–Ti1–O4	83.30(5)	01–Ti1–Cl2	94.50(4)	
01–Ti1–O2	83.55(5)	04–Ti1–Cl2	97.70(4)	
Molecular structure of bis-chelate complex 8a . Displacement ellipsoids are drawn at the 30% probability level.				

Originally, the methyl groups were located as methoxy groups at the oxygen atoms O1 and O4. Obviously, methyl chloride is formed as a by-product during the formation of the bis-chelate complex **8a**. This is in contrast to similar five- and six-membered cyclic chelate complexes reported in the past [82–84] in which computer calculations describe methoxy, hydroxyl as well as benzyloxy groups as stable. Additionally these complexes have a mono-chelate-type structure in which no steric restrictions occur. In the case of the bis-chelate complex **8a** two chlorine atoms remain coordinated to the titanium atom. For steric reasons one methyl group is separated from each ketenacetale to facilitate the formation of the bis-chelate complex which is obviously the most stable product.

The distances of the Ti–O bonds are comparable with those described by Pärssinen et al. [81] for a dichloro-bis(diethylmalonato)titanium(IV) complex being Ti–O: 1.944(1) Å and 2.021(2) Å. The appearance of two different Ti–O distances confirms the assignments of the Raman spectra in which the vibrations at 939 cm⁻¹ (941 cm⁻¹ in the ATR-FTIR spectrum) and 576 cm⁻¹ have been assigned as $\nu(\text{Ti–O=C})$ and $\nu(\text{Ti–O–C})$.

The C–O (C1–O1, C6–O4) and C=O (C3–O2, C8–O5) bond lengths which were observed by X-ray crystal structure analysis confirm the conclusions made from the UV-vis and ATR-FTIR spectra referring to the formation of the bis-chelate complex **8a**. This is

reflected in the UV-vis spectrum which contains two transitions at 252 nm and 320 nm (cf. Figure 6C) as well as in the ATR-FTIR spectrum whereas the band of the $\nu(\text{C}=\text{O})$ vibration is split into two bands at 1638 cm^{-1} and 1615 cm^{-1} . (cf. Figure 7). Additionally the distances of C1-C1 and C6-C7 exhibit double bond character as well as the distances of C2-C3 and C7-C8 are in the range of a $\text{C}(\text{sp}^2)\text{-C}(\text{sp}^2)$ single bond [85].

The bis-chelate complex **8b** derived from a 1:1-mixture of ketenacetale **2b** and TiCl_4 in CH_2Cl_2 could also be isolated and single crystals of **8b** were obtained. The crystal structure of this complex is closely related to that of **8a** with similar bond lengths and angles [9]. The molecular structure with selected bond lengths and angles of **8b** are given in the appendix.

For a comprehensive ex situ characterisation the interactions between the second reactant – diene **1** – and the Lewis acids have to be considered as well. The 1:1-mixture of **1** with TiCl_4 in CH_2Cl_2 has a dark red colour. For this reason UV-vis and Raman spectroscopic analysis was not possible. Additionally, TMSOTf disturbs the Raman measurements, due to strong fluorescence. For this reason, only ATR-FTIR spectra are discussed.

The ATR-FTIR spectrum of 1,3-bis(silyloxy)-1,3-butadiene **1** (cf. Figure 9a) shows three intense bands at 1647 , 1089 , and 1015 cm^{-1} which can be assigned to $\nu(\text{C}=\text{C})$, $\nu_{\text{as}}(\text{C}-\text{O})$, and $\nu_{\text{s}}(\text{C}-\text{O})$, respectively. In the ATR-FTIR spectrum of the 1:1-mixture of **1** with TiCl_4 (Figure 9b) the typical $\nu_{\text{as}}(\text{C}-\text{O})$ and $\nu_{\text{s}}(\text{C}-\text{O})$ vibrations of the ether groups are shifted to lower wavenumbers and are found at 1064 and 954 cm^{-1} . The $\nu(\text{C}=\text{C})$ band is also shifted to essential lower wavenumbers. A broad band at 1533 cm^{-1} with a shoulder at 1580 cm^{-1} is observed indicating an electron delocalisation. Additional bands appear at 465 cm^{-1} (shoulder at 492 cm^{-1}) and 416 cm^{-1} indicating $\nu(\text{Ti}-\text{O})$ vibrations [86, 87]. Similar band positions were observed in the bis-chelate complex of the ketenacetale **2a** with TiCl_4 (493 cm^{-1} with a shoulder at 474 cm^{-1} and 414 cm^{-1} with a shoulder at 438 cm^{-1}). These findings suggest that the reaction of TiCl_4 with 1,3-bis(silyloxy)-1,3-butadiene **1** might result in the formation of a titanium bis-chelate complex, too. The proposed structure of this complex **9** is given in Scheme 10. If the complex contains also chlorine analogous to **8a** and **8b** cannot be determined from ATR data because the respective $\nu(\text{Ti}-\text{Cl})$ vibrations are found below 400 cm^{-1} . But this spectral range is not available by ATR. As mentioned above the measurement of the Raman spectra was not possible. Thus, the respective $\nu(\text{Ti}-\text{Cl})$ modes cannot be identified. Furthermore it has to be considered that under inert atmosphere, $\text{Ti}(\text{IV})$ can oxidise the diene **1** with formation of a bis-chelate by extrusion of 2 equivalents Me_3SiCl and

reduction of Ti(IV) to Ti(III) [88, 89]. The latter has a dark colour. However, the ATR spectroscopic findings clearly suggest the formation of a titanium bis-chelate complex like **9**, whereas the oxidation of **1** by TiCl_4 to some extent cannot be excluded.

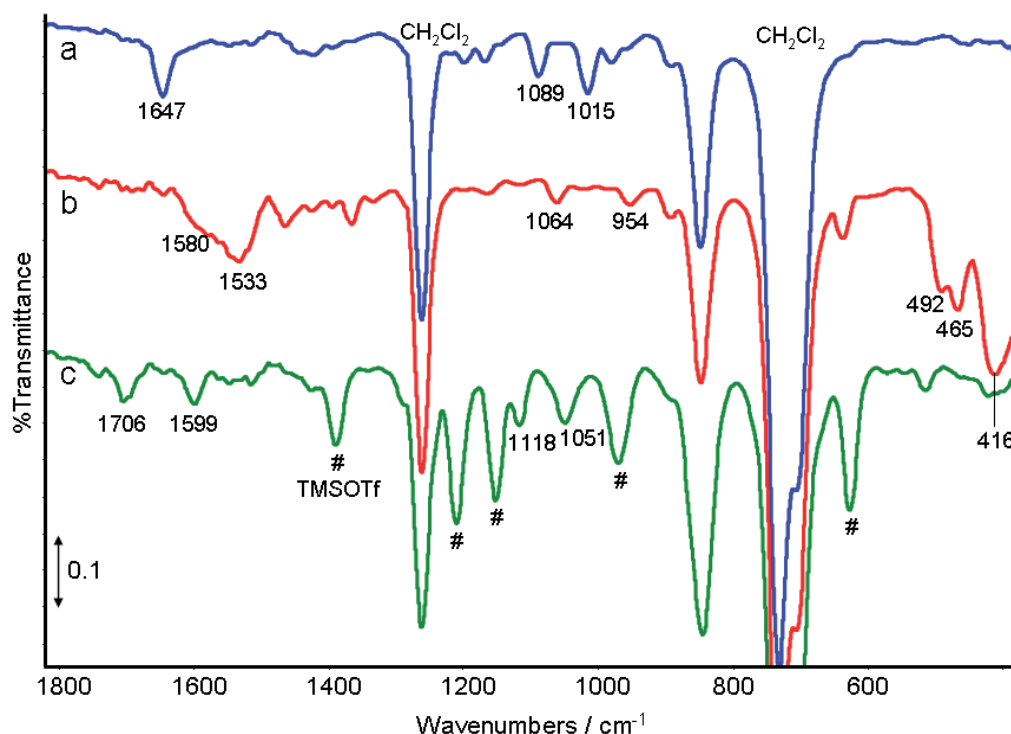
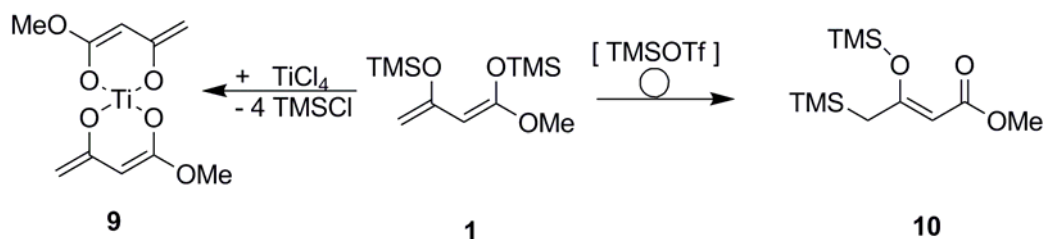


Figure 9. ATR-FTIR spectra of **1** (a) and 1:1-mixtures of **1** with TiCl_4 (b) and TMSOTf (c) in CH_2Cl_2 at $c=0.5 \text{ mol}\cdot\text{L}^{-1}$ (bands of TMSOTf and CH_2Cl_2 are signed).

The spectrum of the 1:1-mixture of **1** with TMSOTf shows new bands at 1706 cm^{-1} and 1599 cm^{-1} (cf. Figure 9c) which can be assigned to $\nu(\text{C}=\text{O})$ and $\nu(\text{C}=\text{C})$, whereas the $\nu_{\text{as}}(\text{C}-\text{O})$ and $\nu_{\text{s}}(\text{C}-\text{O})$ vibrations of the ether groups are shifted to higher wavenumbers (1118 and 1051 cm^{-1}). The formation of a carbonyl group indicates a reaction of **1** with TMSOTf forming a compound like **10** (cf. Scheme 10).



Scheme 10. Proposed reaction of **1** with TiCl_4 .

4.2 The in situ studies under reaction conditions

All experiments described above have been performed at room temperature. But according to the protocol of Bunescu et al. [7] the reaction was carried out in inert atmosphere starting at -78°C and warming up to room temperature over 12-14 hours. Thus, it has to be proven to which extent the temperature influences the reaction pathway. For checking this influence in situ studies using simultaneous UV-vis and ATR-FTIR spectroscopy were exemplarily performed with ketenactetale **2b**. Due to the ex situ studies it has to be proved if both ketenactetale **2a** and **2b** will react in the same way. A novel set-up was designed for realising these in situ investigations which allows the simultaneous registration of ATR-FTIR and UV-vis spectra using fiber optical probes (cf. Figure 3 and Scheme 4).

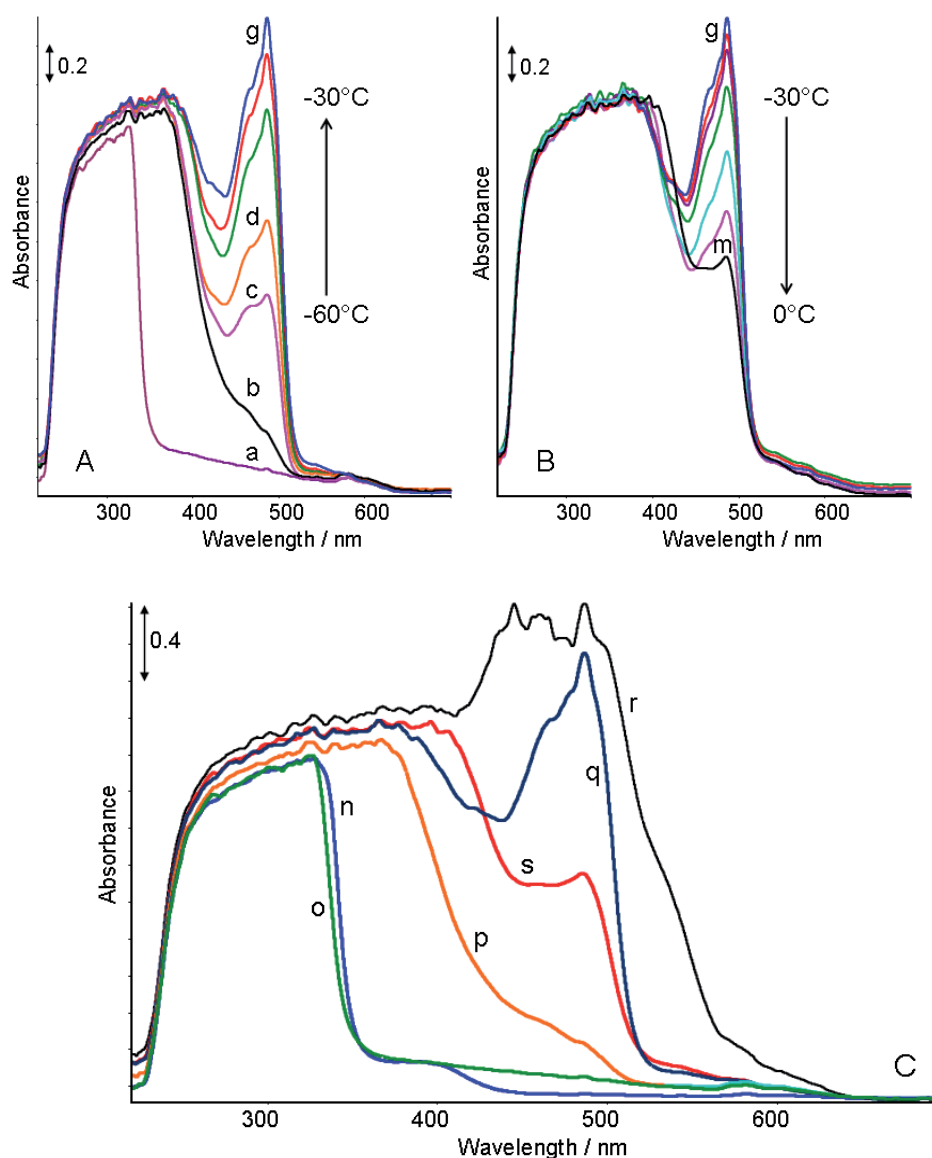


Figure 10. In situ UV-vis spectra of the TMSOTf-route. A: Ketenactetale **2b** + TMSOTf at -60°C (a), Ketenactetale **2b** + TMSOTf + **1** at -60°C , -55°C , -50°C , -45°C , -40°C , and -30°C (b-g). B: Ketenactetale **2b** + TMSOTf + **1** (molar ratio = 1:1:2 in CH_2Cl_2) at -30°C , -25°C , -20°C , -15°C , -10°C , -5°C , and 0°C (g-m). C: Comparison of the spectra of **2b** (n), **2b** + TMSOTf at -60°C (o), **2b** + TMSOTf + **1** at -60°C , -30 , 0°C (p-r), and of the reaction mixture after quenching with aqueous HCl (s).

The in situ UV-vis spectra measured during the warming of the reaction mixture from -60 to 0°C are shown in Figure 10. For clarity the temperature range has been separated from -60 to -30°C (Figure 10A) and from -30°C to 0°C (Figure 10B). Selected spectra of the different reaction steps including the final quenching with aqueous HCl are shown in Figure 10C. The reaction starts with pure ketenacetale **2b** in CH₂Cl₂. The addition of TMSOTf as well as cooling to -60°C has no significant effect on the position of the absorption edge. In contrast, the addition of diene **1** causes a strong shift of the absorption edge to longer wavelengths and a new band at 487 nm with a shoulder at 464 nm appears. The resolution of the latter band increases with increasing temperature (Figure 10A, b-g). This finding points to the existence of delocalised charges. It has to be mentioned that such a characteristic band was observed only in the in situ spectra of the whole reaction mixture. The ex situ prepared 1:1-mixture of TMSOTf and **1** shows a broad UV-vis band as well, but the absorption edge was observed at a lower wavelength and additional weak bands were observed at 450 nm and 500 nm. Surprisingly, the intensity of the band at 487 nm has a maximum at -30°C and decreases again when the reaction mixture was allowed to further warm to 0°C (Figure 10B), while the shoulder at 464 nm completely vanishes.

Possibly, the reaction proceeds by more than one step. The rising band intensity may indicate the first reaction step, while the subsequent decrease of the band at 487 nm may be related to the second step. The final treatment with aqueous HCl leads to a strong increase and broadening of the band between 440 and 490 nm with a shoulder at 540 nm (cf. Figure 10C, spectrum f). This might be caused by formation of an additional chromophore, like a carbonyl group for instance.

The in situ ATR-FTIR spectra (cf. Figure 11) confirm, in principle, the interpretation of the UV-vis spectra, but give also some additional information. Thus, the structure of the complex formed between **2b** and TMSOTf (cf. Scheme 10) changes during cooling from 0 to -60°C indicated by the appearance of a new band at 1643 cm⁻¹ (cf. Figure 11A). Normally, $\nu(\text{C}=\text{O})$ vibrations of silylestere appear in this region. The formation of a silylester might be explained by the assumption that MeOTf is cleaved from the complex like in structure **11** depicted in Scheme 11. Besides the $\nu(\text{C}=\text{O})$ band at 1643 cm⁻¹ additional bands appear at 1153 cm⁻¹, 1107 cm⁻¹, and 1032 cm⁻¹ which can be assigned to ν_{as} and $\nu_{\text{s}}(\text{Si}-\text{O}-\text{C})$ vibrations.

The addition of diene **1** to the reaction mixture (cf. Figure 11B) causes essential changes of the spectra: the $\nu(\text{C}=\text{O})$ band at 1643 cm⁻¹ shifts to 1705 cm⁻¹, and the $\nu(\text{C}=\text{C})$ band from 1556 cm⁻¹ to 1620 cm⁻¹. A structure proposal of the possibly formed intermediate

12 is given in Scheme 11. At the same time additional bands appear at 1189/1129 cm^{-1} and 843 cm^{-1} resulting from $\nu(\text{Si-O-C})$ and $\nu\text{Si}(\text{CH}_3)_3$ vibrations. This suggests that the constitution of the molecule is changed as result of the formal addition of the diene **1** whereas the typical functional groups obviously remain.

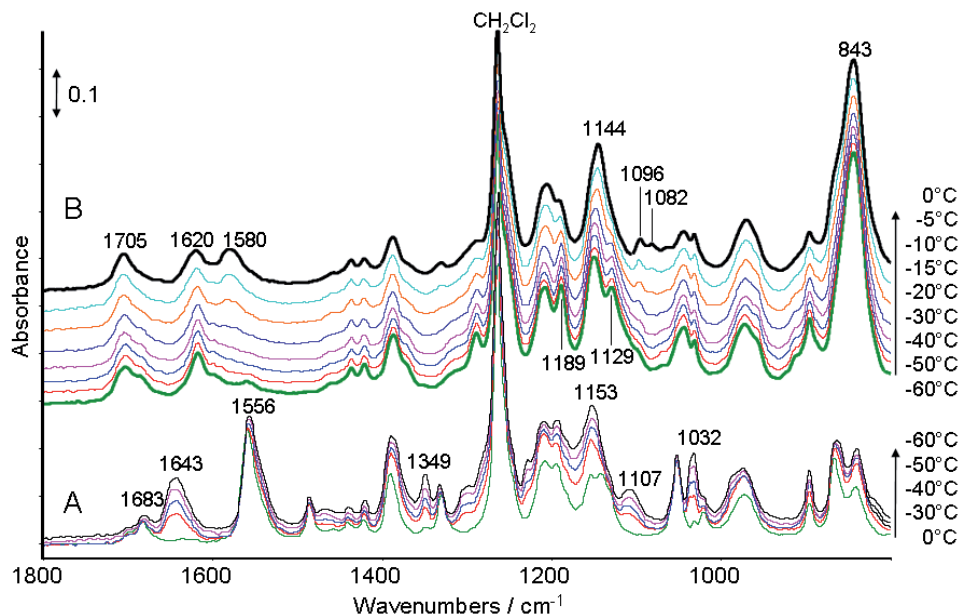
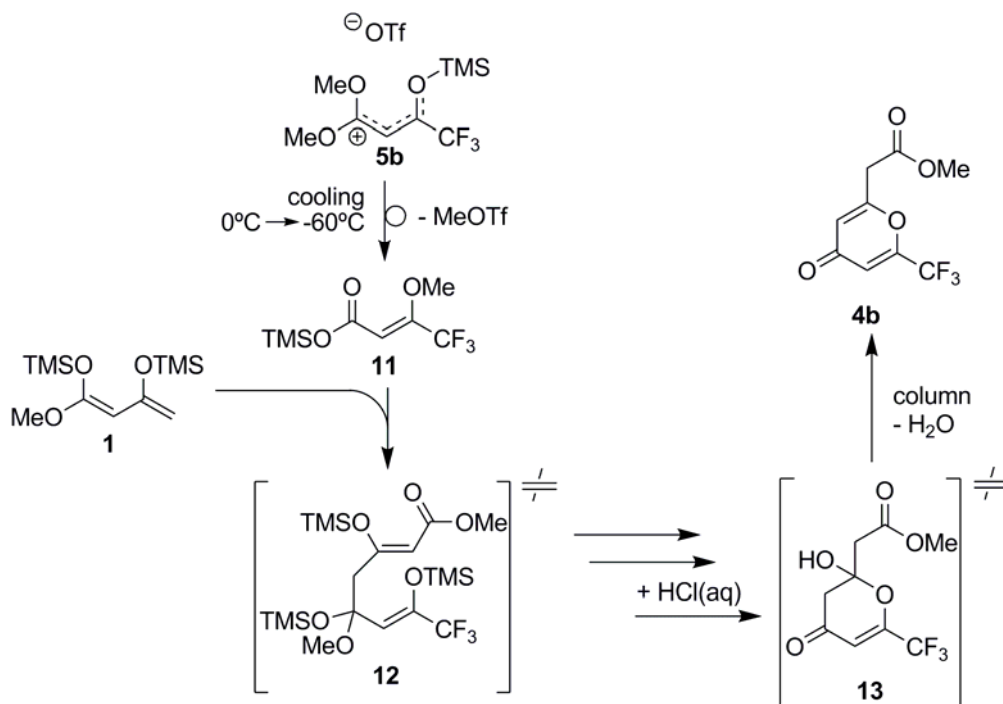


Figure 11. In situ ATR-FTIR spectra of the TMSOTf–route. A: Ketenactetale **2b** + TMSOTf at 0°C, -20°C, -30°C, -40°C, -50°C and -60°C B: Ketenactetale **2b** + TMSOTf + **1** (molar ratio = 1:1:2 in CH_2Cl_2) at -60°C, -50°C, -40°C -30°C, -20°C, -15°C, -10°C, -5°C, and 0°C.



Scheme 11. Proposed mechanism for the TMSOTf-route.

Between -30°C and 0°C new bands appear at 1580 cm^{-1} , 1096 cm^{-1} , and 1082 cm^{-1} with increasing intensity (cf. Figure 11B). Otherwise, the bands at 1189/1128 cm^{-1} loose intensity.

This observation points to changes of the $\nu(\text{C}=\text{C})$ and $\nu(\text{Si}-\text{O}-\text{C})$ modes and leads to the conclusion that the formation of a cyclic molecule as intermediate takes place accompanied by the cleavage of TMSOTf.

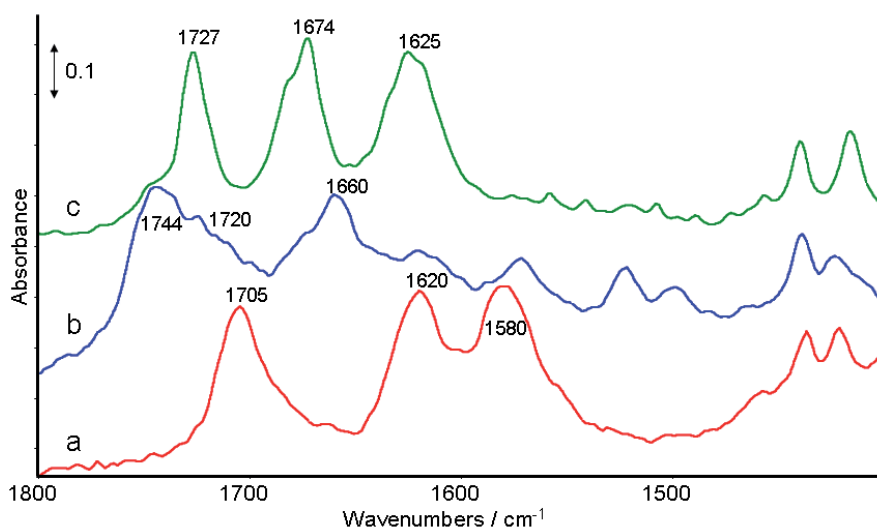


Figure 12. In situ ATR-FTIR spectra of the TMSOTf–route at the end of the reaction: ketenactetale **2b** + TMSOTf + **1** (molar ratio = 1:1:2 in CH_2Cl_2) at 0°C before (a) and after quenching with aqueous HCl (b), ex situ ATR-FTIR spectrum of the main product **4b** after work-up the flash chromatography (c).

By quenching the reaction mixture with aqueous HCl two new bands appear at 1744 cm^{-1} and 1660 cm^{-1} with shoulders around 1720 cm^{-1} and 1676 cm^{-1} , respectively (cf. Figure 12a,b). All bands stem from different carbonyl groups. The comparison of the spectrum of the product obtained by HCl quenching (precursor product, cf. Figure 12b) with the spectrum of the pure solvent-free final product **4b** (cf. Figure 12c), obtained after work-up by flash chromatography, is interesting. In the spectrum of the precursor product the bands of product **4b** can be also observed, possibly overlaid by bands of an additional side product. A proposed structure for this side product is given in Scheme 11 as compound **13**. It cannot be clearly decided whether the product undergoes a reaction during the flash chromatography or is simply separated. A possible mechanism for the TMSOTf route based on the in situ spectroscopic results is given in Scheme 11.

The experiment described above has been repeated using TiCl_4 instead of TMSOTf. The in situ UV-vis spectra recorded during warming of the mixture of ketenactetale **2b**, TiCl_4 and diene **1** (from -60°C to 0°C) are displayed in Figure 13.

The addition of diene **1** provokes no spontaneous deviation in the UV-vis spectrum at -60°C . Only after 30 minutes a shift of the absorption edge to longer wavelengths was observed (cf. Figure 13b). Simultaneously, the absorbance increases rapidly and the bands become noisy. The shift of the absorption band to longer wavelengths can be interpreted as

extended delocalisation of π -electrons. However, the spectrum does not stem from a 1:1-mixture of **1** and TiCl_4 because an ex situ experiment showed that such mixture is not

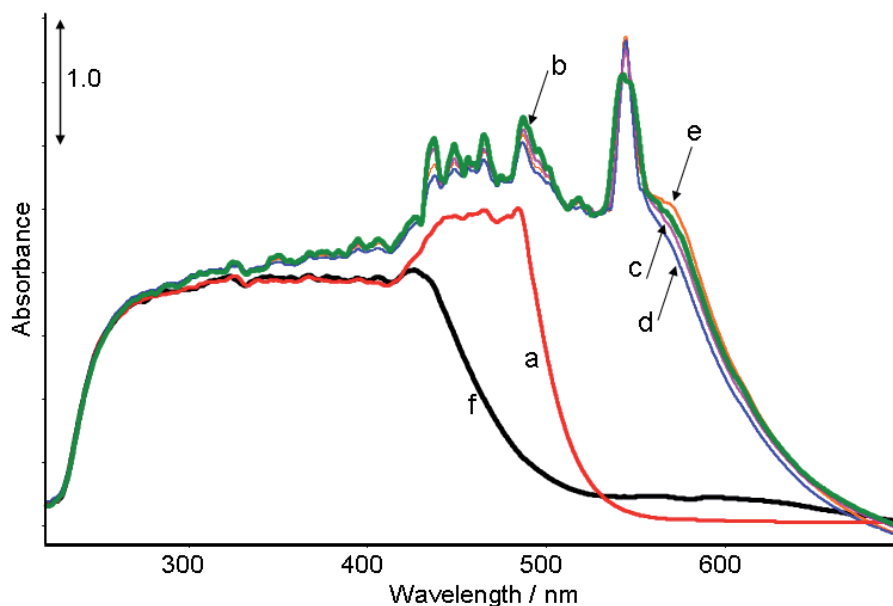


Figure 13. In situ UV-vis spectra of the TiCl_4 -route. Ketenactetale **2b** + TiCl_4 at -60°C (a) **2b** + TiCl_4 + **1** (molar ratio = 1:1:2 in CH_2Cl_2) at -60°C (b), -40°C (c), -20°C (d), 0°C (e), and of the reaction mixture after quenching with aqueous HCl (f).

measurable with the current equipment, due to a very poor signal-to-noise ratio. The warming of the reaction mixture results only in a marginal change of the position of the absorption edge. Obviously, merely one addition product is formed which is stable over the whole temperature range from -60°C to 0°C . Quenching of the reaction mixture with aqueous HCl causes a strong shift of the absorption edge to shorter wavelengths (cf. Figure 13f).

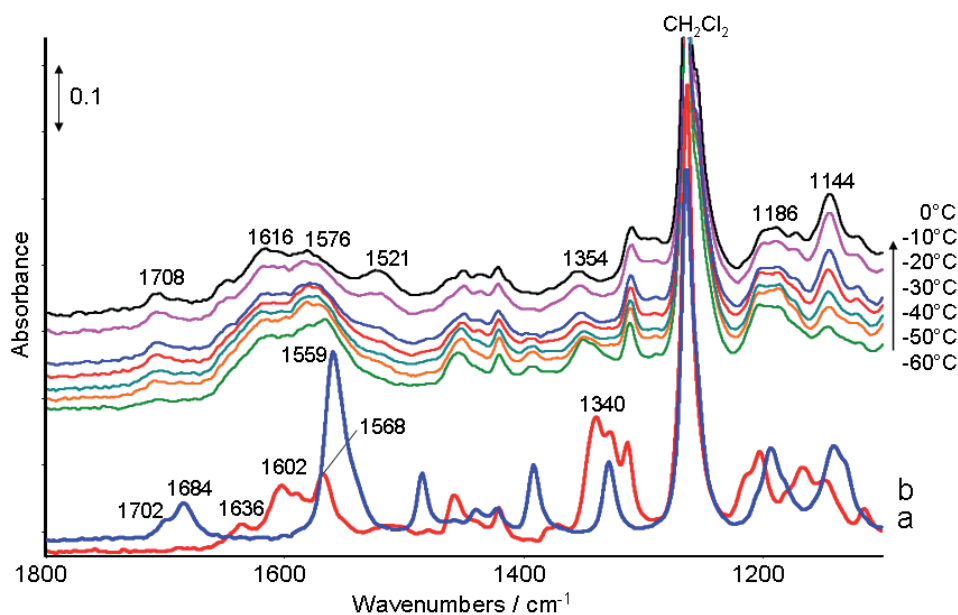


Figure 14. In situ ATR-FTIR spectra of the TiCl_4 -route. Ketenactetale **2b** at 20°C (a), Ketenactetale **2b** + TiCl_4 at -60°C (b), Ketenactetale **2b** + TiCl_4 + **1** (molar ratio = 1:1:2 in CH_2Cl_2) at -60°C , -50°C , -40°C , -30°C , -20°C , -10°C and 0°C .

Inspection of the in situ ATR-FTIR spectra (Figure 14a,b) shows that bis-chelate complex **8b** is initially formed. This is indicated by the disappearance of the $\nu(\text{C}=\text{O})$ vibration mode 1684 cm^{-1} (shoulder at 1702 cm^{-1}) and the simultaneous appearance of the bands at 1636 cm^{-1} and 1602 cm^{-1} (cf. Figure 14b). Furthermore the $\nu(\text{C}=\text{C})$ band is shifted from 1559 cm^{-1} to 1568 cm^{-1} while its intensity is decreased. With cooling to -60°C the spectrum of the bis-chelate complex does not change.

The addition of diene **1** leads to new bands at 1616 cm^{-1} , 1186 cm^{-1} and 1096 cm^{-1} (not shown). The band at 1340 cm^{-1} with a shoulder at 1328 cm^{-1} vanishes. Warming of the reaction mixture from -60°C to 0°C results in the appearance of new bands in the region of $\nu(\text{C}=\text{O})$, $\nu(\text{C}=\text{C})$, and $\nu(\text{C}-\text{O}-\text{C})$ vibrations at 1708 cm^{-1} , 1521 cm^{-1} , and 1144 cm^{-1} , respectively. It seems that rearrangements of various bonds within an intermediately formed complex occur which cannot be assigned in detail.

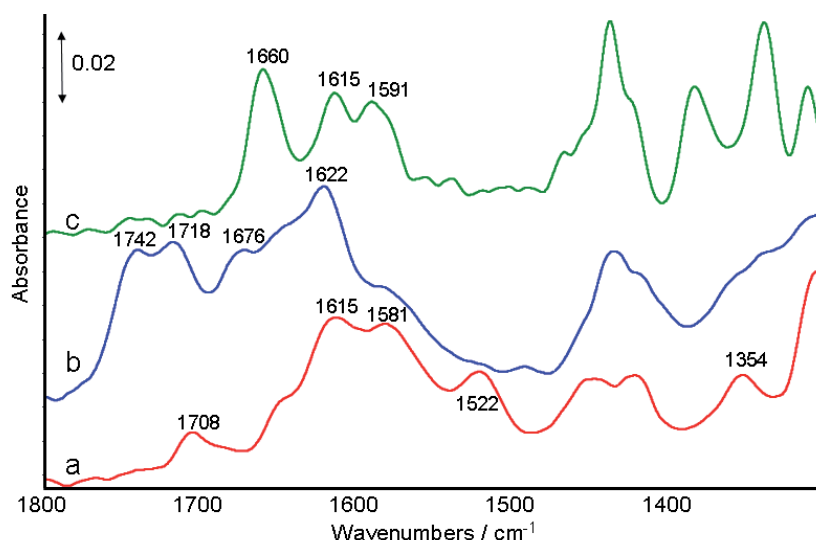


Figure 15. In situ ATR-FTIR spectra of the TiCl_4 -route at the end of the reaction. Ketenactetale **2b** + TiCl_4 + **1** (molar ratio = 1:1:2 in CH_2Cl_2) at 0°C before (a) and after quenching with aqueous HCl (b), ex situ ATR-FTIR spectrum of the product **3b** after work-up the flash chromatography (c).

By addition of aqueous HCl two prominent carbonyl bands appear at 1742 cm^{-1} and 1718 cm^{-1} and another one at 1676 cm^{-1} (cf. Figure 15), while bands at 1581 cm^{-1} , 1522 cm^{-1} , and 1354 cm^{-1} vanish. The present $\nu(\text{C}=\text{C})$ band at 1615 cm^{-1} is slightly shifted to 1622 cm^{-1} . Furthermore, a new band is observed at 1050 cm^{-1} with a shoulder at 1015 cm^{-1} (not shown in Figure 15). Comparison of the spectrum of the precursor product with the spectrum of the final pure salicylate **3b** (Figure 15 b, c) clearly shows that the structure of the precursor product differs from the final product. This suggests that the latter is formed by a reaction taking place during the aqueous work up. The $\nu(\text{C}=\text{O})$ band of salicylate **3b** appears at 1660 cm^{-1} which is in the typical region of carbonyl vibrations of α -ketoesters.

4.3 Conclusion 1

By means of different ex situ and in situ spectroscopic methods the mode of action of both Lewis acids TiCl_4 and TMSOTf utilised in the [3+3] cyclisation reaction of a diene **1** and a ketenacetale **2a** and **2b** could be elucidated. The formation of different products dependent on the type of Lewis acid used can be explained by two completely different reaction pathways which are mainly directed by the specific interaction of the Lewis acids with the ketenacetale.

It could be shown by ATR-FTIR and UV-vis spectroscopy that TMSOTf interacts with only one site of the ketenacetale while TiCl_4 forms a bis-chelate complex. The formation of the bis-chelate complex is obviously favoured by the ability of TiCl_4 to realise various coordination possibilities. The formation of the bis-chelate complex was additionally confirmed by Raman spectroscopy. Thus, the respective vibrations of Ti–O and Ti–Cl bonds could be clearly identified. The spectroscopic findings were confirmed by single crystal X-ray structure analysis which reveals the formation of a bis-chelate complex. Such complexes were formed with both used ketenacetals as confirmed by their molecular structures. This means that both ketenacetals react in the same way with TiCl_4 .

Coupled ATR-FTIR/UV-vis spectroscopic investigations were carried out in a novel homemade reaction cell to monitor the reaction between -60°C and $+20^\circ\text{C}$ enabling comprehensive insight in the reaction progress. In situ UV-vis spectroscopic investigations evidenced that the TiCl_4 -route proceeds via one reaction step while the TMSOTf-route comprises two steps. Unfortunately it is not possible to discriminate if the second step is limited by thermodynamics or kinetics.

In situ ATR-FTIR spectroscopic investigations showed that the temperature affects the formation and structural changes of different intermediates, in particular during the TMSOTf-route. Both, the final quenching of the reaction mixture with aqueous HCl as well as the applied work-up procedure lead to changes in terms of product formation and distribution. It seems that the chosen work-up procedure can influence product formation, too.

4.4 Transfer of the obtained results to similar systems

The previous investigation showed that the driving force for the product selectivity depends on the formation of the formed intermediate complexes between the applied acids and the reactants. The obtained conclusions can be used for the improvement of processes and including similar substances in the system. Three tasks should be investigated for the transfer of the previous conclusions:

1. Utilisation of aluminium(III)chloride as Lewis acid

Analogue to TiCl_4 , AlCl_3 is also known to form chelate complexes with bidentate ligands like acetyl acetate. However, aluminium is a main group element without d-electrons. Thus, the comparison of AlCl_3 with TiCl_4 allows estimating the influence of d-electrons referring to spectroscopic characterisation as well as to reaction performance.

2. From single phase to multi-phase systems: Application of solid Lewis acids

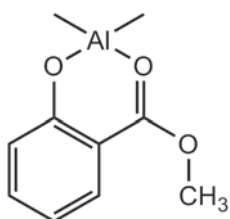
TiO_2 and Al_2O_3 are known as solid Lewis acids and are widely applied as supports in the production of heterogeneous catalysts. After elucidating the potential of TiCl_4 and AlCl_3 to act as mediating acid in liquid phase, these two solid acids were tested in the reaction, too. The characterisation of surface adsorbates may give information about the reaction mechanism.

3. Introduction of N-salicylideneaniline **14** as substrate for the reaction

The ketenacetale **2b** and N-salicylideneaniline have similar structure elements where N-salicylideneaniline has a $\text{C}=\text{N}$ double bond instead of a $\text{C}=\text{O}$ double bond and the corresponding functional group in 4-position is changed from a methoxy group to a hydroxyl group. Considering that N-salicylideneaniline can act as bidentate ligand in coordination compounds, the potential to utilise this substrate for the cyclisation reaction was studied.

4.5 Utilisation of aluminium(III)chloride as Lewis acid

Figure 16 shows the ATR-FTIR spectra recorded in situ during the reaction of **2b** with **1** in the presence of AlCl_3 . The first spectrum (Figure 16a) shows **2b** dissolved in CH_2Cl_2 at 20°C . Important bands occur at 1684 cm^{-1} with a shoulder at 1702 cm^{-1} which belong to the $\nu(\text{C}=\text{O})$ vibration and at 1559 cm^{-1} which can be assigned to a $\nu(\text{C}=\text{C})$ vibration. When AlCl_3 is added to **2b** and the reaction mixture is cooled to -60°C , the band of the $\nu(\text{C}=\text{O})$ vibration is shifted to lower wavenumbers and appears at 1628 cm^{-1} with increased intensity (cf. Figure 16b). This shift is characteristic for the interaction between a carbonyl group and a Lewis acid.



Pasynkiewicz et al. [90]

A similar observation is reported by Pasynkiewicz et al. [90]. They reported a band at 1628 cm^{-1} in the spectrum of a monomeric aluminium methyl 2-hydroxybenzoate chelate complex. Hence, it is likely that the interaction of **2b** with AlCl_3 takes place via the carbonyl group, too. New bands occur at 1351 and 1166 cm^{-1} which can be assigned to $\nu(\text{C}-\text{O}-\text{C})$

and $\nu(\text{C-O-Al})$ vibrations [90]. Simultaneously the intensity of the band of the $\nu(\text{C=C})$ vibration becomes decreased and the band is slightly shifted to 1557 cm^{-1} which was observed as well when **2b** forms a bis-chelate complex with TiCl_4 [9].

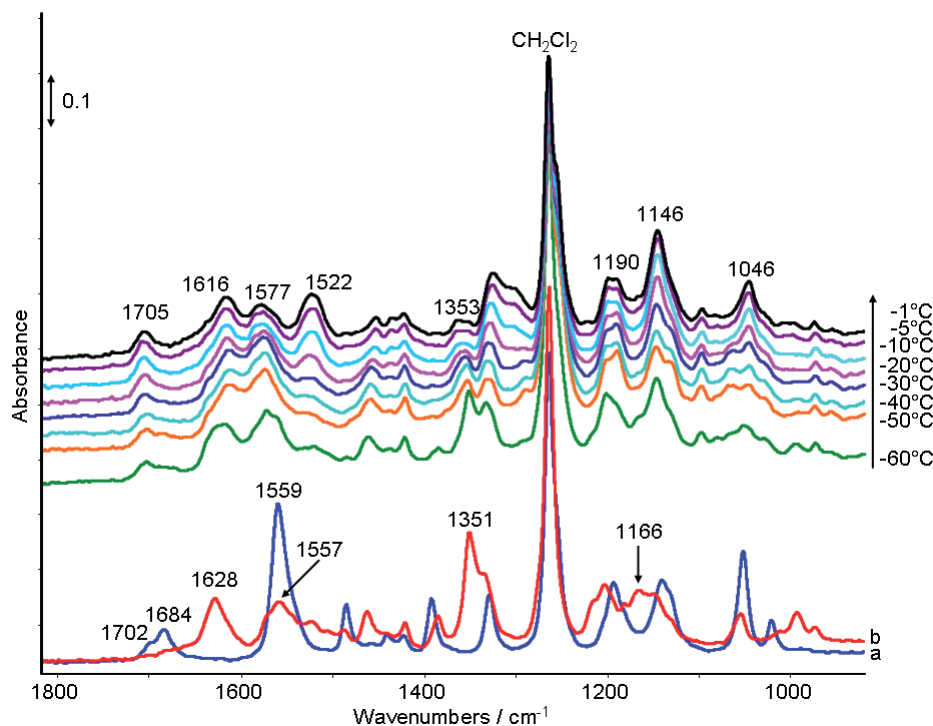


Figure 16. In situ ATR-FTIR spectra of the AlCl_3 mediated reaction: (a) **2b** in CH_2Cl_2 ($c = 0.5\text{ mol}\cdot\text{L}^{-1}$) at 20°C without AlCl_3 , (b) **2b** + AlCl_3 at -60°C in 1:1-mixture (molar ratio); and of **2b** + AlCl_3 + **1** as 1:1:2-mixture (molar ratio) at -60 , -50 , -40 , -30 , -20 , -10 , -5 and -1°C .

Table 2. Positions and assignments of bands observed during reaction.

2b + AlCl_3 + 1 ν / cm^{-1}	2b + TiCl_4 + 1 ν / cm^{-1} [9]	Assignment
1705	1708	$\nu(\text{C=O})$
1616	1616	$\nu(\text{C=C})$
1577	1576	$\nu(\text{C=C})$
1522	1521	$\nu(\text{C=C})$
1351	1354	$\nu_{\text{as}}(\text{C-O-C})$
1190	1186	$\nu(\text{C-O-M})$ (M = Al, Ti)
1146	1144	—
1046	—	—

The in situ measured spectra of the reaction mixture after dosing of **1** at -60°C to the 1:1-mixture of **2b** and AlCl_3 are shown in Figure 16 as well. The positions of the characteristic bands occurring during reaction indicate that the reaction mechanism is similar to the TiCl_4 -

mediated reaction as shown in the previous section [9]. Table 2 shows the comparison of characteristic bands occurring in the AlCl_3 and in the TiCl_4 mediated reactions. It is obvious that the positions of the bands are very similar.

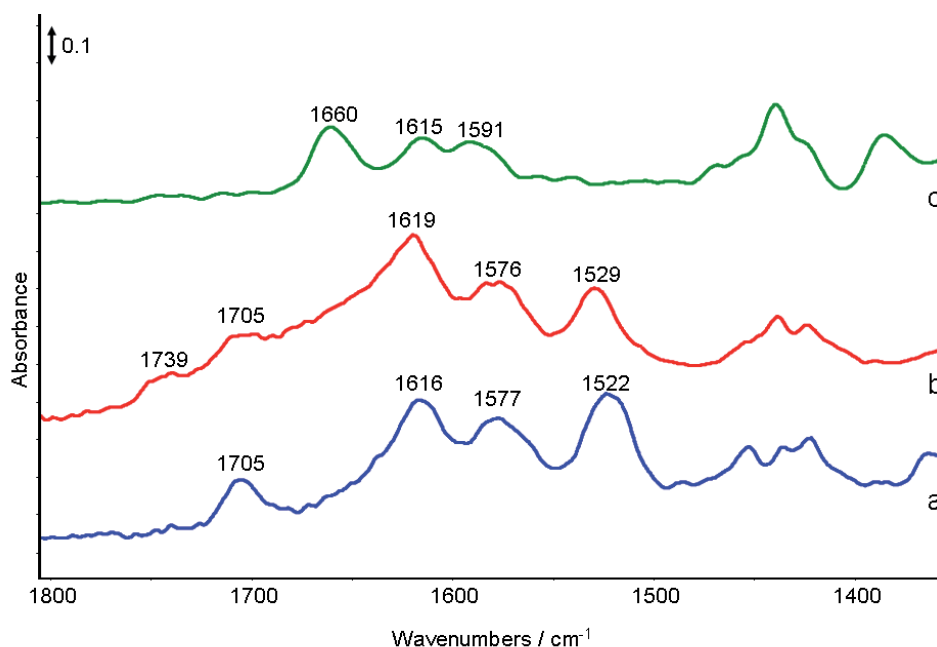


Figure 17. In situ ATR-FTIR spectra of the AlCl_3 mediated reaction at the end: **2b** + AlCl_3 + **1** as 1:1:2-mixture (molar ratio) at -1°C (a) before and (b) after quenching with $\text{HCl}(\text{aq})$; (c) ex situ spectrum of **3b** after work-up with flash chromatography shown for comparison.

The similarity of the AlCl_3 and in the TiCl_4 mediated reactions can be studied as well when the reaction is quenched with aqueous HCl at the end. The last spectrum before quenching (cf. Figure 17a) and the spectrum after quenching (cf. Figure 17b) are similar to spectra recorded during the TiCl_4 mediated reaction. Contrary to the TiCl_4 mediated reaction, the conversion is higher when AlCl_3 is utilised under the same reaction conditions (AlCl_3 : 69% / TiCl_4 : 42%).

Table 3. Positions and assignments of bands observed after quenching with aqueous HCl .

2b + AlCl_3 + 1 + $\text{HCl}(\text{aq})$	2b + TiCl_4 + 1 + $\text{HCl}(\text{aq})$	Assignment
ν / cm^{-1}	ν / cm^{-1} [9]	
1739	1742	$\nu(\text{C}=\text{O})$
1705	1718	$\nu(\text{C}=\text{O})$
—	1676	$\nu(\text{C}=\text{C})$
1619	1618	$\nu(\text{C}=\text{C})$
1576	1581	$\nu(\text{C}=\text{C})$
1529	—	$\nu(\text{C}=\text{C})$

The observed band positions during the AlCl_3 and TiCl_4 mediated reactions are shown in Table 3 where the similarity is obvious again. Finally, the spectrum of the pure product obtained after work-up with flash chromatography is shown for comparison in Figure 17 (cf. Figure 17c). The obtained spectrum is comparable with that spectrum taken from the product after the work-up with flash chromatography in the TiCl_4 mediated reaction. This means that the work-up procedure is an important step for the final product formation in the AlCl_3 mediated reaction as well as in the TiCl_4 mediated route.

In order to elucidate the electronic nature of the reaction intermediates in situ UV-vis-transmission spectroscopy was applied. Figure 18 shows the in situ measured UV-vis-transmission spectra during reaction. Due to the relatively high concentration the UV-vis spectra have an unusual shape. However, the spectrum of **2b** (cf. Figure 18a) shows at 20°C a broad band with maximum at 335 nm and a weak one at 380 nm which might represent $\pi \rightarrow \pi^*$ and $n \rightarrow \pi^*$ transitions, respectively.

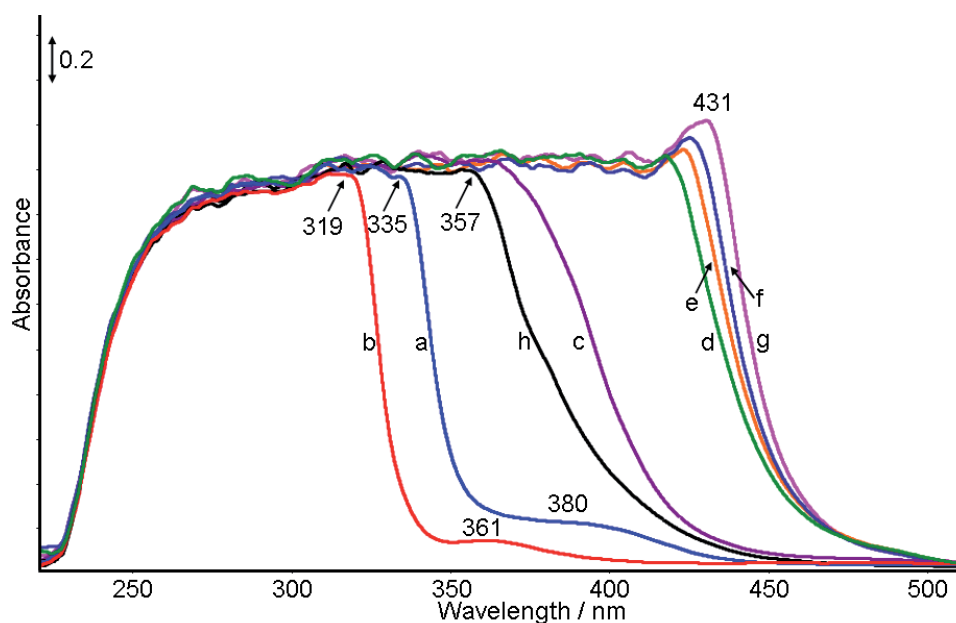


Figure 18. In situ-UV-vis-transmission spectra of the AlCl_3 -mediated conversion of **1** and **2b** to **3b**: (a) 1 equiv. **2** in CH_2Cl_2 ($c = 0.5 \text{ mol}\cdot\text{L}^{-1}$) at 20°C before and (b) after addition of 1 equiv. AlCl_3 at -60°C; mixture of **2** + AlCl_3 + **1** (molar ratio 1:1:2) (c) -60°C, (d) at -50°C, (e) at -40°C, (f) at -30°C, (g) at -20°C; (h) after quenching with $\text{HCl}(\text{aq})$.

Both signals shift to shorter wavelengths when AlCl_3 is added and the temperature is decreased and appear finally at 319 nm and 361 nm at -60°C (cf. Figure 18b). At this point the volume contraction of the solvent has to be considered. Due to lowering the temperature the volume decrease which causes an increase of concentration. An increased concentration can provoke a shift to longer wavelengths at this concentration level. But, here the opposite behaviour can be observed. This might be caused by a stronger interaction between **2b** and

AlCl_3 with decreasing temperature. The addition of **1** at -60°C provokes immediately a strong shift to longer wavelengths (cf. Figure 18c) which is almost completed after 20 minutes (cf. Figure 18d). The maximum is shifted with increasing temperature and reaches its maximum of 431 nm (cf. Figure 18e-g). Finally, the quenching with $\text{HCl}(\text{aq})$ provokes a shift of the maximum to 357 nm (cf. Figure 18h).

The in situ measured UV-vis spectra indicate that the number of reaction steps in the AlCl_3 mediated reaction is the same as for the TiCl_4 mediated reaction. The shift to shorter wavenumbers after mixing **2b** with AlCl_3 is surprising because it is contrary to the investigations with TiCl_4 . In the TiCl_4 route a strong shift to higher wavelengths could be observed when **2b** was mixed with TiCl_4 due to the formation of a bis-chelate complex. The Ti-atom is bonded to the oxygen of the carbonyl group as well as to the oxygen atom of one methoxy group. Due to the delocalisation of π -electrons an additional chromophore is created which cause the shift of the absorption band to longer wavelengths in the UV-vis spectrum of the chelate complex. Hence, the shift to shorter wavelengths in the UV-vis spectrum of the **2b**- AlCl_3 mixture indicates a different electronic state. This would fit to the fact that the UV-vis spectra indicate the influence of temperature in the formation of the AlCl_3 -complex. This was not observed in the formation of the TiCl_4 complex **8b** as shown in the previous section [9].

For a better assignment of the bands occurring in the UV-vis spectra of **2b** and in the 1:1-mixture of **2b** with AlCl_3 , diluted solutions have been measured (cf. Figure 19), too. The spectrum of **2b** shows one discrete band with a maximum at 278 nm when the concentration level is $5 \cdot 10^{-4} \text{ mol} \cdot \text{L}^{-1}$. But also the spectrum of the 1:1-mixture of **2b** and AlCl_3 in CH_2Cl_2 ($c = 5 \cdot 10^{-4} \text{ mol} \cdot \text{L}^{-1}$) shows one band at 275 nm. This band is slightly more intense than the band occurring in the spectrum of **2b** alone.

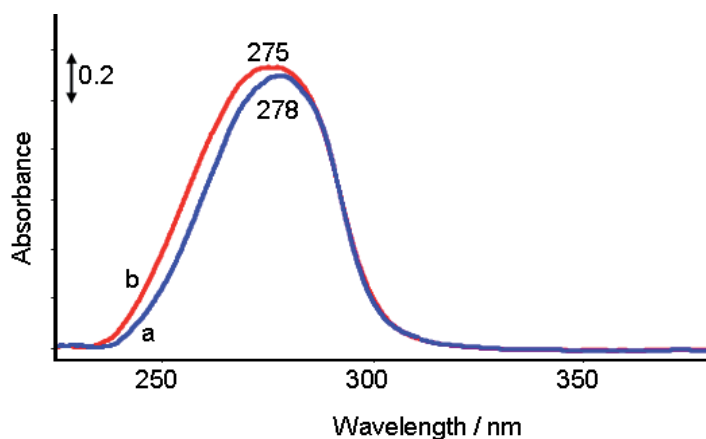


Figure 19. Ex situ UV-vis spectra of **2b** (a) and **2b** + AlCl_3 (b) in CH_2Cl_2 ($c = 5 \cdot 10^{-4} \text{ mol} \cdot \text{L}^{-1}$).

But it is questionable if this difference indicates a significant change in the electronic structure or an interaction between **2b** and AlCl_3 . On the other hand a band which is characteristic for AlCl_3 cannot be observed. This band would occur at 240 nm [91]. Hence, an interaction between **2b** and the AlCl_3 is likely.

One possible explanation for the shape of the UV-vis spectrum of the 1:1-mixture of **2b** and AlCl_3 might be the absence of $d\pi$ -electrons in the AlCl_3 -complex. Holm and Cotton [92] as well as Nakamoto et al. [93, 94] point out in their studies that $d\pi$ - $d\pi$ and $d\pi$ - $p\pi$ interactions are important factors in the bond formation between metal and donor system. These interactions lead to bonds with resonance structures which is also known as metalaromaticity [95]. The Al–O bond in $\text{Al}(\text{acac})_3$ is characterised as strongly covalent bond [93]. The missing $d\pi$ -electrons cause that less resonance structures appear and all bonds remain localised. Nakamoto et al. [93, 94] describe such complexes where the electrons remain localised in the ligand skeleton of the chelate ring as “weak complexes”. Contrary in strong chelate complexes the π -electrons and the d-electrons of the metal atom tend to be more or less delocalised in the whole chelate ring. Consequently, the electronic structure is less changed in the weak chelate complex, and the UV-vis spectrum of the mixture of **2b** and AlCl_3 shows no significant difference at room temperature. Furthermore, the interaction is obviously not strong enough to form a second chromophore like shown for the 1:1-mixture of **2a** and TiCl_4 in CH_2Cl_2 [9]. Otherwise a second band or a shoulder should be observable.

4.6 Supplementary ex situ investigations

Up to this point the observations show that the mechanism is not really clear as could be expected from the in situ obtained ATR-FTIR spectra of the reaction which are very similar to the TiCl_4 -route. Although the major part of the AlCl_3 -mediated reaction is rather similar to the TiCl_4 mechanism there are some details which are different. The UV-vis spectra indicate that the AlCl_3 -complex formed during reaction does not seem to be exactly an analogue of the TiCl_4 -complex which is formed during the TiCl_4 mediated reaction. In order to elucidate these details additional ex situ measurements have been performed. Raman spectroscopy would be an adequate method because it provides information about the low frequency area where the vibrations of metal-non-metal bonds are located. Unfortunately no usable spectra could be obtained because of the fluorescence of the samples. Hence, the analysis has been carried out with ATR-FTIR spectroscopy.

Figure 20 shows the ex situ measured ATR-FTIR spectra of **1** and a 1:1-mixture of **1** and AlCl_3 . Due to the interaction with AlCl_3 the bands at 1647, 1088, and 1013 cm^{-1} which are assigned to $\nu(\text{C}=\text{C})$, $\nu_{\text{as}}(\text{C}-\text{O}-\text{C})$ and $\nu_{\text{s}}(\text{C}-\text{O}-\text{C})$ vibration modes, shift to other positions. In the mixture the bands of the $\nu_{\text{as}}(\text{C}-\text{O}-\text{C})$ and $\nu_{\text{s}}(\text{C}-\text{O}-\text{C})$ vibration modes can be observed at 1144 cm^{-1} with shoulder at 1122 cm^{-1} and at 1048 cm^{-1} . The bands of the $\nu(\text{C}=\text{C})$ vibrations

occurs at 1605 and 1526 cm^{-1} . Interestingly, these bands have a rather distinct shape and are not blurred due to delocalised charges like in the complex of **1** with TiCl_4 [9].

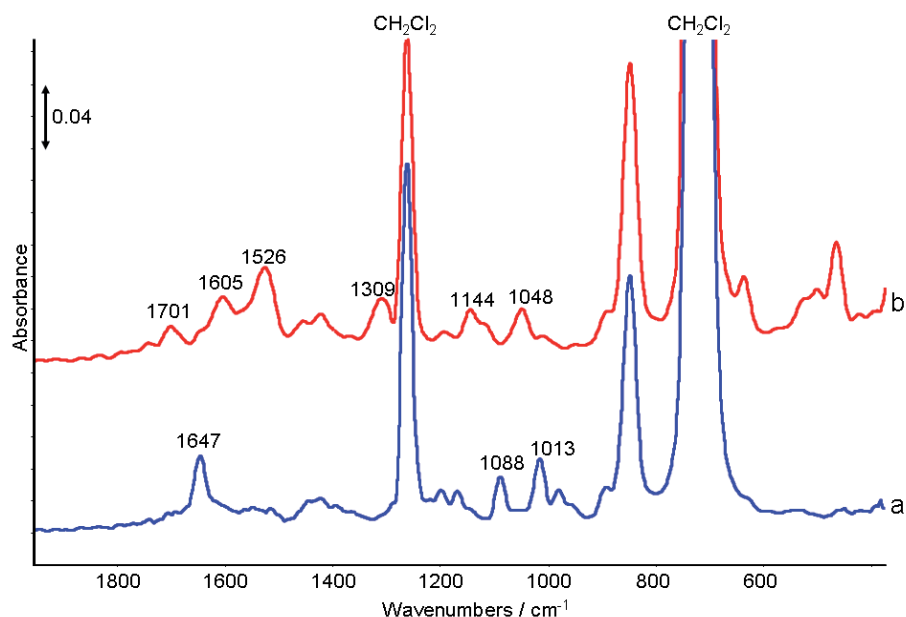


Figure 20. Ex situ ATR-FTIR spectra of **1** (a) and the 1:1-mixture (molar ratio) with AlCl_3 (b) in CH_2Cl_2 ($c = 0.5 \text{ mol}\cdot\text{L}^{-1}$).

This supports the previous conclusion that AlCl_3 has a similar role as TiCl_4 in this reaction but reacts slightly different with **1** and **2b**. The explanation of this behaviour could be that amount of delocalised electrons is lower when AlCl_3 is applied as concluded from the UV-vis-transmission spectra. Finally, the appearance of the band at 1701 cm^{-1} in the spectrum of the mixture shows that also a side product containing a carbonyl group is formed.

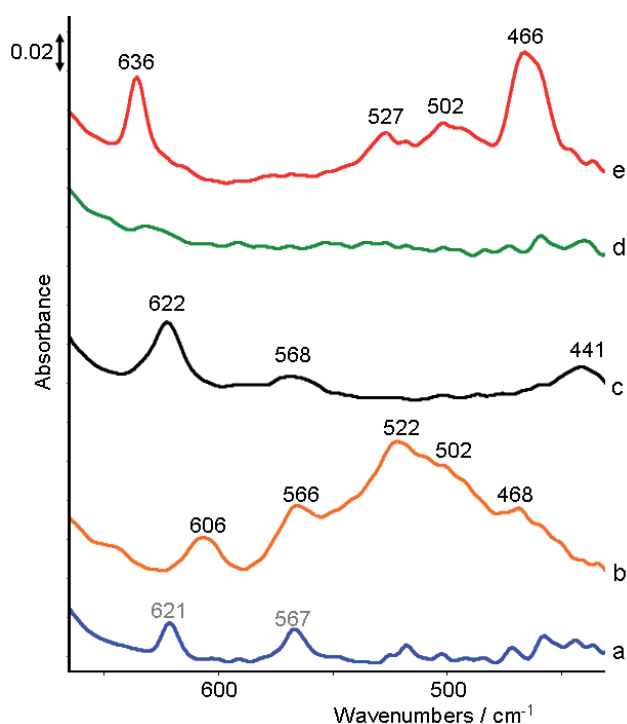


Figure 21. Ex situ ATR-FTIR spectra of **2b** (a), **2b** + AlCl_3 (b), AlCl_3 (c), **1** (d), **1** + AlCl_3 (e) in CH_2Cl_2 ($c = 0.5 \text{ mol}\cdot\text{L}^{-1}$).

The spectra of **1**, **2b** and their 1:1-mixtures with AlCl_3 in the low-frequency area are displayed in Figure 21. The spectrum of AlCl_3 dissolved in CH_2Cl_2 is shown for comparison with bands occurring at 622, 568, and 441 cm^{-1} . The band at 622 cm^{-1} can be assigned to the ν_8 and the band at 441 cm^{-1} to the ν_{13} vibration mode of Al_2Cl_6 [96]. The other band might root from impurities.

The spectrum of **1** shows no significant bands between 650 and 425 cm^{-1} . But mixing **1** with AlCl_3 provokes the appearance of new bands at 636, 527, 502, and 466 cm^{-1} . Also the spectrum of **2b** shows only bands at 621 and 567 cm^{-1} . In the spectrum of the mixture of **2b** with AlCl_3 a strong band at 522 cm^{-1} with a shoulder at 502 cm^{-1} and more bands at 606, 566, and 468 cm^{-1} can be seen.

Due to the lack of reference data it is difficult to make certain assignments for the bands. But the observed changes in the spectra reflect the interaction of **1** as well as **2b** with AlCl_3 . Despite different intensities the new bands occurring in both mixtures appear at comparable positions. Thus, the type of interaction should be similar as it was found in the mixtures of **1** and **2b** with TiCl_4 [9], too. The nature of the interaction is obviously a donor-acceptor-type interaction. It is known that $[\text{AlCl}_3]_2$ can be split by donors like R_3N to $\text{R}_3\text{N}\cdots\text{AlCl}_3$ [97, 98].

It is not possible to draft a distinct structure for the intermediate formed between **2b** and AlCl_3 like **8a** and **8b** in the TiCl_4 -mediated reaction. This is because no molecular structure from single crystals could be obtained and the observed bands in the spectra are not specific enough. The formation of TMSCl seems to be important for the formation of the intermediate. But, AlCl_3 provides only three chloride atoms instead of four like TiCl_4 . Hence, the stoichiometric factors are different which prevent to draft a distinct structure for an intermediate. Additionally, aluminium has the tendency to form chlorine-bridged dimers which complicates to draft a proposed intermediate. Similar problems occur for the description of the intermediate formed between **1** and AlCl_3 .

4.7 From single-phase to multi-phase systems: utilisation of solid Lewis acids

The utilisation of solids offers new possibilities in terms of catalyst separation and handling. For elucidating the potential for this reaction, sulphate-free TiO_2 and Al_2O_3 were selected as solid acids. The selection is based on the fact that the reaction works successfully in liquid phase with TiCl_4 as well as with AlCl_3 . Furthermore the adsorption of diketones on TiO_2 nano-particles has been studied already with FTIR spectroscopy [99]. Finally, alumina has been applied successfully in organic synthesis as moderating acid [100, 101]. Another important point for the selection was that both solid acids possess only Lewis acid centres.

Both solids were applied for the conversion of **1** and **2b** to **3b**. First experiments gave yields of 13% for TiO₂ and 17% for Al₂O₃, respectively [102].

The UV-vis spectra are taken of **2b** which was adsorbed on the solid acids (cf. Figure 22). Spectra of the pure metal oxides have been taken as well for comparison. The pure Al₂O₃ shows two weak and broad bands at 272 nm and 368 nm. Because Al₂O₃ is known as UV-vis inactive, these bands have their origin in additives which are commonly used for the preparation of Al₂O₃. Due to the weakness of the bands they should not disturb further analysis.

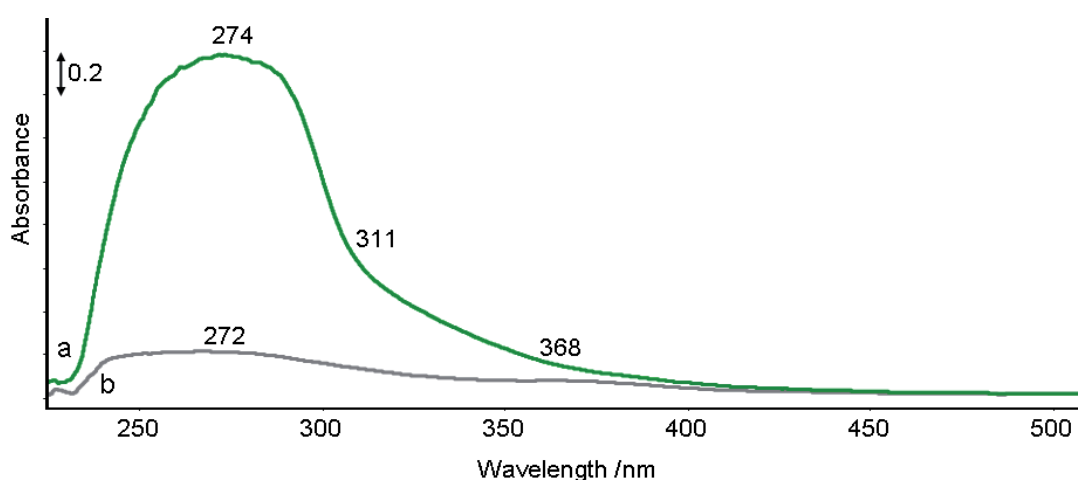


Figure 22. UV-vis-DRS spectra of **2b** adsorbed on Al₂O₃ (a) and of pure Al₂O₃ (b).

On Al₂O₃ **2b** could be detected nicely with UV-vis-DRS spectroscopy (cf. Figure 22). An intense band with maximum at 274 nm indicates the presence of adsorbed **2b**. The maximum is similar as for pure **2b** and its 1:1-mixture with AlCl₃ in CH₂Cl₂ with a concentration of 5·10⁻⁴ mol·L⁻¹. The band of the UV-vis-DRS spectrum of the adsorbed **2b** is broader and more intense than in the spectrum taken with the transmission probe in solution. This might be an effect of concentration and measuring mode.

Contrary, TiO₂ shows a broad with an absorption edge at 352 nm (spectrum not displayed). This intense band roots from a charge transfer transition. Additional signals which would indicate the presence of **2b** could not be observed. In a further experiment the TiO₂ was taken as white standard instead of BaSO₄ which is used for this purpose commonly. But also in this experiment no significant signal of **2b** could be detected.

The FTIR-transmission spectra have been obtained from self-supporting wafers of Al₂O₃ on which the reactants **1** or **2b** have been separately adsorbed. Spectra of solutions of **2b** and **1** in CH₂Cl₂ are shown for comparison (cf. Figure 23).

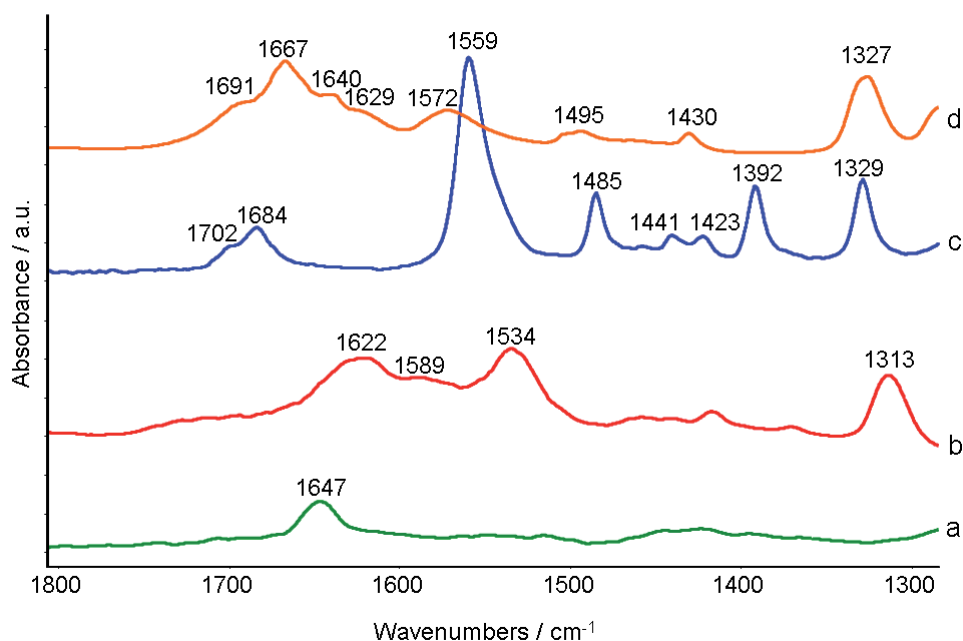


Figure 23. ATR-FTIR spectrum of **1** in CH_2Cl_2 ($c=0.5 \text{ mol}\cdot\text{L}^{-1}$) (a) and FTIR-transmission spectrum of **1** adsorbed on Al_2O_3 (b); ATR-FTIR spectrum of **2b** CH_2Cl_2 ($c=0.5 \text{ mol}\cdot\text{L}^{-1}$) (c) and FTIR-transmission spectrum of **2b** adsorbed on Al_2O_3 (d); FTIR-transmission spectra measured from self-supporting wafer.

The spectrum of adsorbed **1** shows similarities to the spectrum of the species formed by interaction of **1** with AlCl_3 in liquid phase (cf. Figure 20). The spectrum of adsorbed **1** in Figure 23 has strong bands at 1313 cm^{-1} and 1534 cm^{-1} which appear at 1309 cm^{-1} and 1526 cm^{-1} in the spectrum of the mixture of **1** with AlCl_3 (cf. Figure 20). Another strong band occurs in the spectrum of the adsorbed **1** at 1622 cm^{-1} containing a shoulder at 1589 cm^{-1} . The corresponding band occurs in the 1:1-mixture of **1** and AlCl_3 in CH_2Cl_2 at 1605 cm^{-1} . Hence, solid Al_2O_3 interacts in a comparable way with **1** as AlCl_3 in liquid phase.

The FTIR-transmission spectrum of adsorbed **2b** shows a strong band at 1667 cm^{-1} with shoulders at 1691 cm^{-1} , 1640 cm^{-1} and 1629 cm^{-1} . The signals at 1691 cm^{-1} and 1625 cm^{-1} are already assigned to vibrations of the carbonyl groups of pure **2b** (1691 cm^{-1}) and the AlCl_3 -complex (1625 cm^{-1}). According to Pasykiewicz et al. [90] and to Denyshevskii et al. [103] the band at 1640 cm^{-1} is prominent for the vibration of a carbonyl group which is bounded to an aluminium atom. An assignment for the band at 1667 cm^{-1} has not been made up to now but it is likely that also this band is prominent for a $\nu(\text{C}=\text{O})$ vibration. The shift and the splitting of the carbonyl band of **2b** at $1702 / 1684 \text{ cm}^{-1}$ to lower wavenumbers reflect that an interaction of **2b** with Al_2O_3 surface takes place.

The appearance of four signals for the $\nu(\text{C}=\text{O})$ vibration indicates that **2b** may adsorb in different manner on the surface of Al_2O_3 . The band at 1667 cm^{-1} with the shoulder at 1691 cm^{-1} may be prominent for physisorbed **2b**. Due to the weak interaction with the surface of

the Al_2O_3 the vibrational state of the $\nu(\text{C}=\text{O})$ mode is changed only slightly. Contrary the shoulders at 1640 and 1625 cm^{-1} might be prominent for chemisorbed **2b**. Here the carbonyl group is involved strongly in the adsorption mechanism.

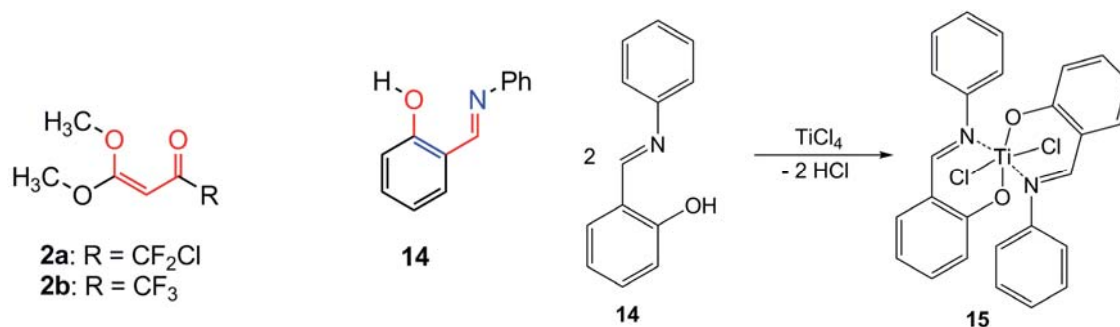
The $\nu(\text{C}=\text{C})$ vibration appears at 1572 cm^{-1} with decreased intensity. Contrary to the formation of the chelate complex between **2b** and AlCl_3 in solution a shift of the band to higher wavenumbers can be observed.

Two weak bands can be observed at 1495 cm^{-1} with shoulder at 1503 cm^{-1} and at 1430 cm^{-1} . These bands could be prominent for the methoxy groups whereas the first band can be assigned to $\delta_{\text{as}}(\text{CH}_3)$ vibration mode and the second as $\delta_{\text{s}}(\text{CH}_3)$ vibration mode. The strongly decreased intensity indicates that the methoxy group is involved in the adsorption process as well. Due to the lack of bands for comparison it is difficult to provide a more details how the methoxy groups are involved in the adsorption process. But, the strong decrease of band intensity might be evidence that the adsorption has rather character of chemisorption.

The band at 1327 cm^{-1} can be assigned to $\nu(\text{C}-\text{F})$ vibration. Position and intensity remain rather unchanged compared to the ATR-FTIR spectrum of solid **2b**.

4.8 Introduction of N-salicylideneaniline **14** as substrate for the reaction

The application of N-salicylideneaniline **14** instead of ketenacetals like **2a** and **2b** as substrate in the reaction is interesting because of the similar structure elements (cf. Scheme 12). **14** is able to form with TiCl_4 chelate-type complexes like **15** (cf. Scheme 13).



Scheme 12. Similar structures of the ketenacetale and N-salicylideneaniline.

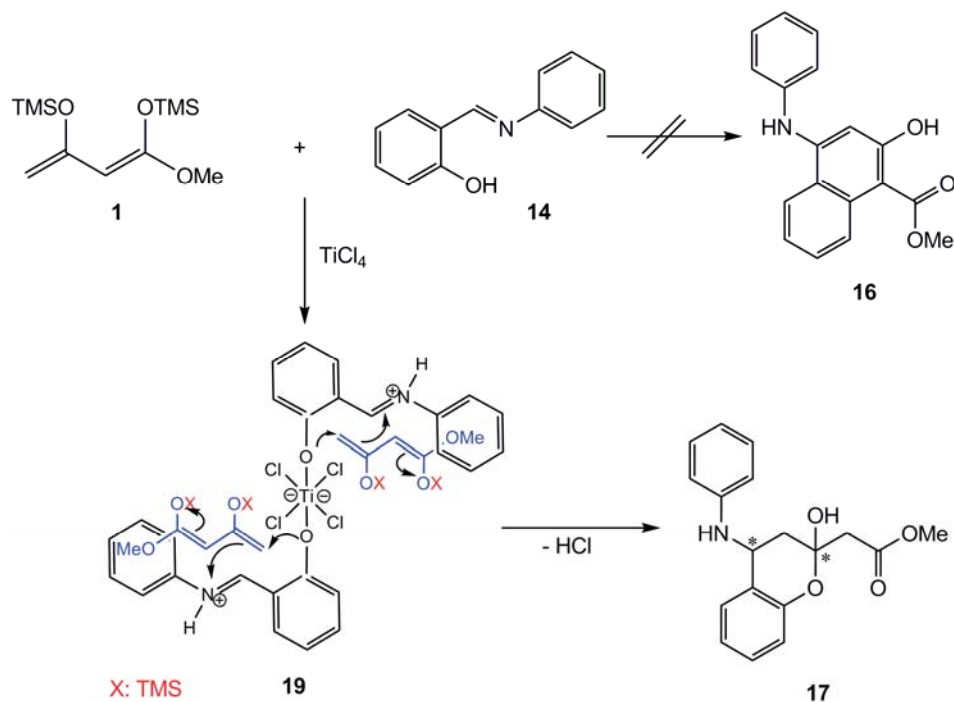
Scheme 13. Proposed reaction product **15** obtained from **14** and TiCl_4 referring to the UV-vis-DRS spectra.

According to the results of the previous sections a naphthene-type product like **16** (cf. Scheme 14) is expected to be formed when the reaction is carried out under the same conditions as for the production of **3a** or **3b**.

But instead of the formation of **16** a chromane-type product **17** was obtained after reaction with a yield of 82% after 4 h reaction time and work-up with flash chromatography.

Compared with the obtained yield of 38% after 4 h the reaction of **2b** with **1** the reaction of **14** with **1** proceeds more effective.

The product **17** exhibits two steric centres: one at the C1-atom and one at the C3-atom. The diastomeric ratio determined by X-Ray analysis was found to be for SS/RR : SR/RS = 60 : 40. For SS : RR as well as for SR : RS the ratio is 50 : 50 [104].



Scheme 14. Proposed reaction mechanism for the TiCl_4 -mediated cyclocondensation reaction between **1** and **14**.

For the elucidation the interactions between **14** and TiCl_4 a mixture of both compounds was prepared in a ratio of 2:1 in CH_2Cl_2 . The concentration of $0.5 \text{ mol}\cdot\text{L}^{-1}$ was similar to the concentration of the reactants during reaction. After mixing both components a dark-red precipitate immediately occurred which make it impossible to investigate this precipitate by UV-vis-transmission and Raman spectroscopy in liquid phase. Therefore, the precipitate was isolated and dried and investigated in solid state.

In a second experiment **14** and TiCl_4 were mixed in a ratio of 1:1 in CH_2Cl_2 in a concentration of $0.5 \text{ mol}\cdot\text{L}^{-1}$. Also in this case a dark-red precipitate occurred which was isolated and analysed in the same way as the precipitate of the 2:1 mixture. The obtained ATR-FTIR, UV-vis-DRS and Raman spectra as well as the obtained XRD-patterns showed no significant deviations between both samples. Obviously, always two molecules of **14** interact with one TiCl_4 molecule.

The UV-vis-DRS spectrum of the solid dark-red substance formed from the 2:1-mixture of **14** with TiCl_4 (cf. Figure 24a) shows a broad band containing two maxima at 286 nm and 484 nm and a shoulder at 533 nm. The UV-vis-DRS spectrum of pure solid **14** (cf.

Figure 24b) has a different shape compared to spectra which are recorded in diluted solutions. This is caused by bulk effects like intermolecular hydrogen bonding. The spectrum shows three maxima at 257 nm, 300 / 315 nm and 395 nm. The band at 257 nm could be assigned to $\sigma \rightarrow \pi^*$ transition and the band at 300 nm and 315 nm to $\pi \rightarrow \pi^*$ transitions which have their origin from the phenyl rings of **14**. Certainly the band at 395 nm belongs to a $\pi \rightarrow \pi^*$ transition as well. A proper assignment seems to be difficult in this case because the band of the $\pi \rightarrow \pi^*$ transition of the benzyl ring of the imine form occurs at 339 nm while the long-wave band of the quinoid tautomer occurs at 427 nm [105, 106].

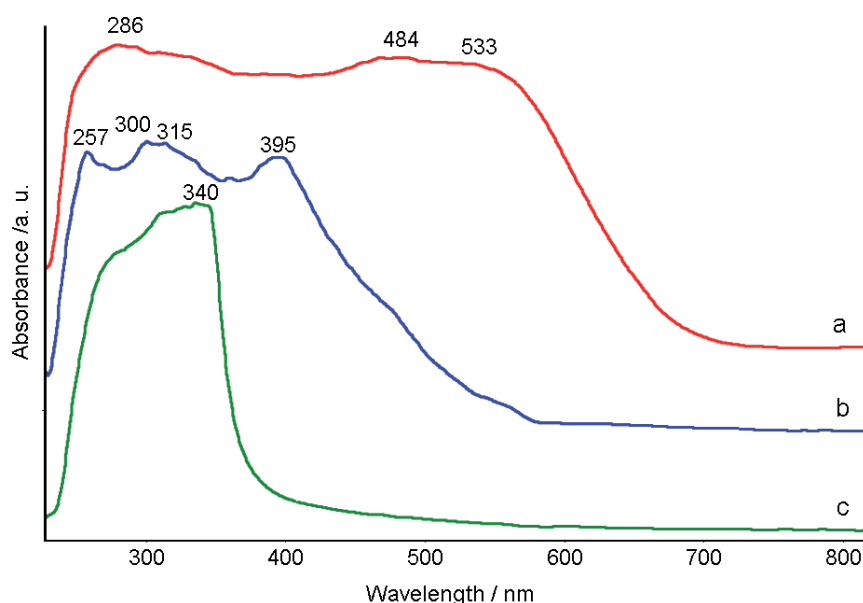


Figure 24. Ex situ UV-vis-DRS spectra of the solid 2:1 mixture of **14** and TiCl_4 (a) and the solid **14** alone (b). The UV-vis-transmission spectrum of TiCl_4 dissolved in CH_2Cl_2 ($c=0.5 \text{ mol}\cdot\text{L}^{-1}$) is shown for comparison (c).

According to the previous results the shift to longer wavelengths could indicate the formation of a bis-chelate complex like structure **15** in Scheme 13. Such compound was described by Biradar and Kulkarni [107], but the colour was yellow. This is contrary to the dark-red colour of the obtained precipitate in this study and suggests that the obtained dark-red precipitate has another structure than **15**. However, an examination of the preparation methods of **15** and related compounds [74, 107-110] revealed that for obtaining the desired chelate compound a final treatment of the reaction mixture with bases like NEt_3 or heating is necessary to remove HCl . This was not done in this investigation which implicates that the formed complex contains more chlorine.

In Table 4 the calculated element percentages for different assumed compositions of the complex between **14** and TiCl_4 are compared with the experimental values. The obtained values clearly show that the composition of the dark-red precipitate is not comparable with **15** and seems to have rather the empirical formula $\text{C}_{26}\text{H}_{22}\text{N}_2\text{O}_2\text{Cl}_4\text{Ti}$. The differences between

calculated and experimental mass percentages indicate that new compound is not pure. However, the N/Cl ratio is 1:2 which points to the formation of $C_{26}H_{22}N_2O_2Cl_4Ti$.

Table 4. Calculated and obtained element percentages for different assumed compositions of the complex between **14** and $TiCl_4$.

Composition	Ti (%)	Cl (%)	N (%)	Ratio Ti/Cl/N
$C_{26}H_{20}N_2O_2Cl_2Ti$ [107]	8.82	13.08	5.16	1.0 : 2.0 : 2.0
$C_{26}H_{22}N_2O_2Cl_4Ti$ (calc.)	8.21	24.29	4.80	1.0 : 4.0 : 2.0
Complex [14 + $TiCl_4$] (exp.)	9.50	23.80	4.66	1.0 : 3.4 : 1.7

The Raman and ATR-FTIR spectra of the dark-red precipitate and the ATR-FTIR spectrum of **14** in different spectral ranges are shown in Figure 25. Due to the strong fluorescence of pure **14** no Raman spectrum could be obtained from this substance. The spectrum of solid **14** (cf. Figure 25A, spectrum a) shows characteristic bands at 1613, 1587, 1568, and 1273 cm^{-1} which correspond to $\nu(C=N)$, $\nu(Ph-N)$, $\nu(Ph-C)$, and $\nu(C-O)$ vibrations, respectively [109, 111, 112]. In the spectrum of the dark-red precipitate (cf. Figure 25A, spectrum b) a band at 1638 cm^{-1} is observed (1641 cm^{-1} in the Raman spectrum, cf. Figure 25c), which can be assigned to the shifted $\nu(C=N)$ vibration mode caused by the protonation of the $C=N$ double bond in **14**. Such effect has already been observed by studying the interaction of imines with Lewis-acidic heterogeneous catalysts [40]. Obviously, the interaction between the Lewis acid $TiCl_4$ and **14** takes place in a similar way.

The spectrum of the precipitate shows more strong bands located at 1600 and 1588 cm^{-1} in the ATR-FTIR spectrum and at 1602 and 1589 cm^{-1} in the Raman spectrum (cf. Figure 25A, spectra b and c). They can be assigned to $\nu(Ph-N)$ and $\nu(Ph-C)$ vibration modes. These bands are shifted due to protonation as well because the charge stabilisation takes place via the complete azomethine moiety [113]. A further new band occurs at 1544 cm^{-1} in the ATR-FTIR and 1549 cm^{-1} in the Raman spectrum, respectively. This band was also observed when imines adsorb on the surface of solid Al_2O_3 and can be assigned to a $\nu(C=C)$ vibration induced by formation of a protonated azomethine moiety [40, 114].

The ATR-FTIR spectrum of solid **14** (cf. Figure 25A, spectrum a) shows another strong band at 1273 cm^{-1} which is observed in the spectrum of the precipitate (cf. Figure 25A, spectrum b), too. This band can be assigned to $\delta(OH)$ [115] or $\nu(C-O)$ vibration [109]. However, this band was not observed in the Raman spectrum (cf. Figure 25A, spectrum c). Instead a very strong band can be observed at 1302 cm^{-1} which is not present in the corresponding ATR-FTIR spectrum.

Reference spectra of **14** dissolved in CCl_4 (cf. Appendix p. G) confirm this conclusion. Here the ATR-FTIR spectrum shows a strong band at 1286 cm^{-1} and a very weak band at 1322 cm^{-1} . The corresponding Raman spectrum of **14** shows a weak band at 1286 cm^{-1} and a strong band at 1322 cm^{-1} . This suggests that the observed vibration in the Raman spectrum is IR-inactive.

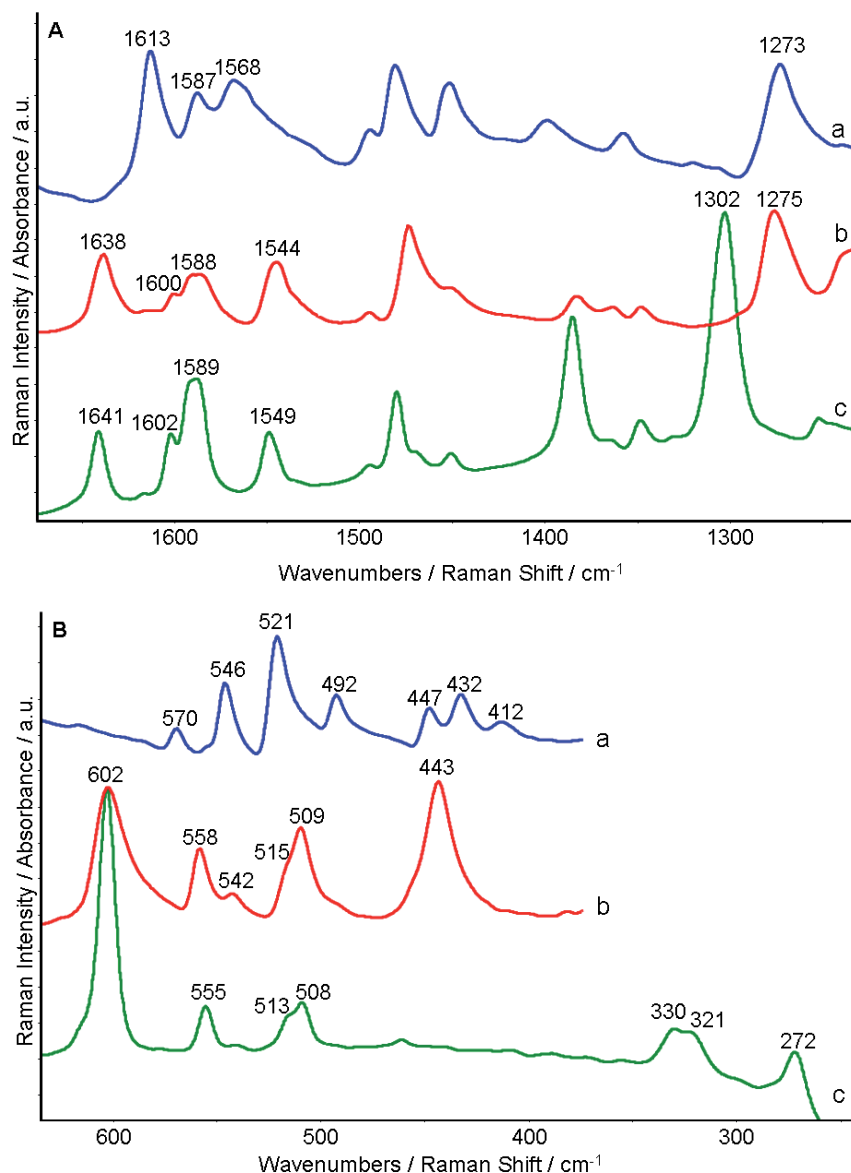
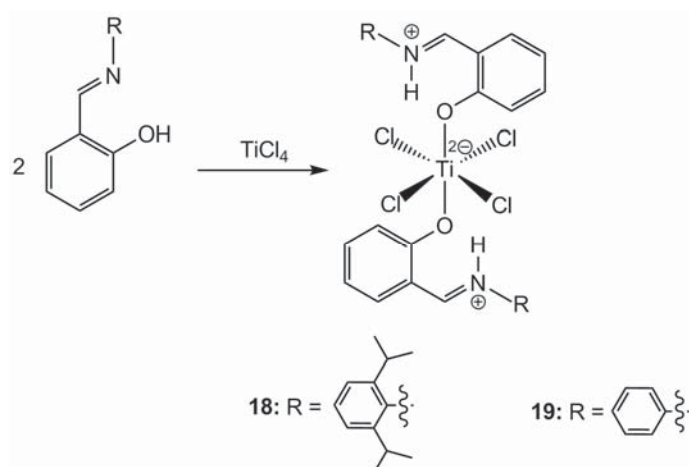


Figure 25. Ex situ ATR-FTIR spectrum of solid **14** alone (a), ex situ ATR-FTIR (b) and ex situ Raman spectra (c) of the dark-red precipitate from the 2:1 mixture of **14** and TiCl_4 (molar ratio). (A) spectral range $1650\text{--}1250\text{ cm}^{-1}$, (B) spectral range $625\text{--}(400)\text{--}250\text{ cm}^{-1}$.

In the low-frequency range (cf. Figure 25B) a new strong band occurs at 602 cm^{-1} in the ATR-FTIR and Raman spectra of the dark-red precipitate from the mixture **14** and TiCl_4 . This band might be prominent for a $\nu(\text{Ti}\text{--}\text{O})$ vibration observed also in trichlorotitanium(IV) alkoxides [116]. The bands at $330/321\text{ cm}^{-1}$ in the Raman spectrum (cf. Figure 25B spectrum c) can be assigned to $\nu(\text{Ti}\text{--}\text{Cl})$ vibrations [74, 116]. Alternatively, this band could be also be

assigned to the ν_1 and the band at 272 cm^{-1} to the ν_2 vibration of TiCl_6^{2-} [117]. But the formation of TiCl_6^{2-} in significant amounts would occur only if **14** and TiCl_4 are mixed in 1:1 ratio and complex **15** would be the resulting main product and this is not the case. Characteristic bands of TiCl_4 or TiCl_3 [77, 80, 117] do not appear in the spectra, and there were no hints for TiCl_3 from XRD analysis. The absence of Ti(III)-species has been proved also by EPR spectroscopy.

Summarised, the vibrational spectra indicate that the C=N double bond of **14** is involved in the interaction with TiCl_4 . The formation of Ti–O bonds proceeds obviously under participation of the OH group of **14**. Otherwise the elementary analysis reveals the formation of a complex of TiCl_4 with two imine molecules.



Scheme 15. Schematic structure of the 2:1 complex according [110].

Strauch et al. [110] reported about formation and structural properties of salicylaldiminato complexes of titanium. They described the structure of the red 1:2 complex **18** (cf. Scheme 15) which was formed by the reaction of TiCl_4 with two molar equivalents of N-(2,6-diisopropylphenyl)salicylimine in CH_2Cl_2 . The molecular structure of this compound indicates that two imines are bonded via their oxygen atoms to the titanium atom. All four chlorine atoms are bonded to the titanium atom leading to an octahedral coordination sphere of the titanium atom. The proton of the hydroxyl group has migrated to the nitrogen atom and is bonded via the electron lone pair of the nitrogen atom.

Starting from imine **14** used in this work the respective complex **19** with comparable structure should be obtained. The comparison of the IR spectroscopic data described for **18** with the data obtained for the dark-red precipitate from the mixture **14** and TiCl_4 (cf. Table 5) reveals that both substances are very similar to each other. Due to the very poor solubility of **19** in various solvents a further characterisation by the means of NMR spectroscopy or X-ray structure analysis was not possible.

Table 5. Selected IR frequencies (cm^{-1}) of the solid complexes **18** and **19** (cf. Scheme 15).

18 [110]	19 [104]	Assignment
1635 (vs)	1638	$\nu(\text{C}=\text{N})$
1549 (s)	1545	$\nu(\text{Ph}-\text{NH}^+)$
1469 (vs)	1474	
1386 (m)	1384	
1332 (w)	1347	
1283 (vs)	1276	$\nu(\text{C}-\text{O})$
1144 (m)	1147	
916 (m)	912	
798 (s)	801	
753 (m)	756	
613 (s)	602	$\nu(\text{Ti}-\text{O})$

To get insight into the overall reaction in situ ATR-FTIR spectroscopic investigations were performed studying exemplarily the TiCl_4 -mediated reaction between 1,3-bis(silyloxy)-1,3-butadiene **1** and N-salicylideneaniline **14**. The investigation was carried out under the same reaction conditions which were used in the previous experiments (cf. Scheme 7). The application of in situ UV-vis-transmission spectroscopy failed because the red precipitate (**19**) formed at the beginning of reaction between **14** and TiCl_4 perturbed the measurements.

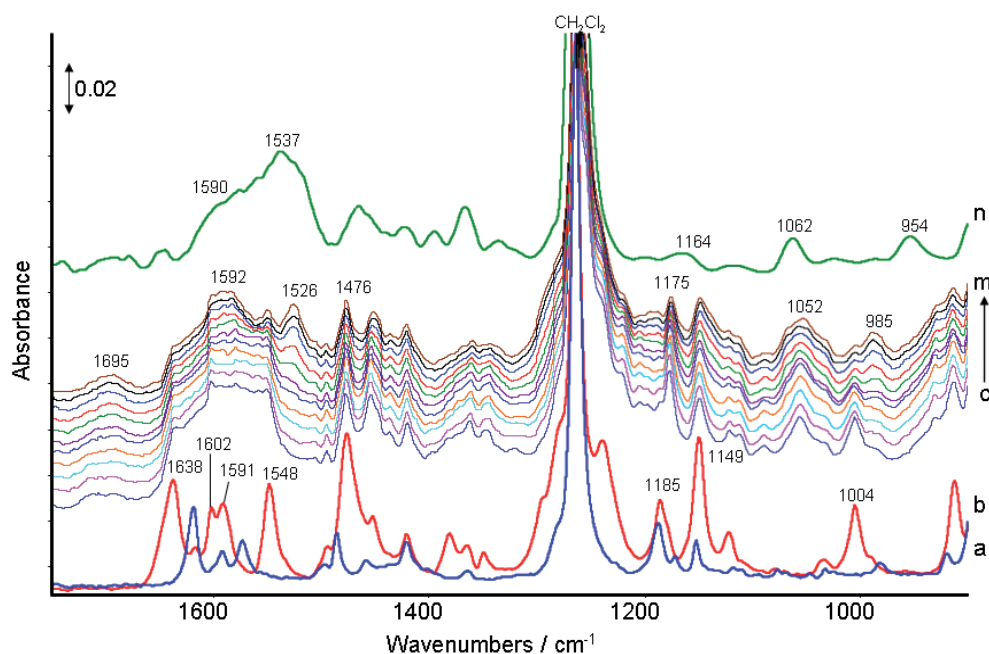


Figure 26. In situ ATR-FTIR spectra of the TiCl_4 mediated reaction between **14** and **1** in CH_2Cl_2 as solvent: (a) **14** at 0°C ; (b) **14** + TiCl_4 (1:1 molar ratio) at -60°C ; (c) – (m) **14** + TiCl_4 + **1** (1:1:2 molar ratio) at -50 , -40 , -35 , -30 , -25 , -20 , -15 , -10 , -5 , -3 and -2°C ; (n) spectrum of **1** + TiCl_4 (1:1 molar ratio) for comparison.

The situ ATR-FTIR spectra obtained during reaction of **14** and **1** are displayed in Figure 26. The spectra of **14** in CH₂Cl₂ at 0°C (cf. Figure 26 a), of the mixture of **14** and TiCl₄ at -60°C (cf. Figure 26b), and of **1** in CH₂Cl₂ at 25°C (cf. Figure 26 n) were included for comparison. The spectrum of **14** dissolved in CH₂Cl₂ (cf. Figure 26a) is comparable with that measured in the solid state (cf. Figure. 25A). Merely the band of the $\nu(\text{C}=\text{N})$ vibration is shifted from 1613 cm⁻¹ to 1617 cm⁻¹ because the intermolecular interactions occurring in solution are weaker than in solid state [106]. The addition of TiCl₄ to **14** effects characteristic shifts (cf. Figure 26b) which were discussed already. This interaction occurs independently from the temperature in CH₂Cl₂. For this reason only the spectrum of the 1:1-mixture of **14** with TiCl₄ at -60°C is exemplarily shown in Figure 26n.

By addition of **1** at -50°C the resulting spectrum of the reaction mixture (cf. Figure 26c) can be perceived as a summation of spectrum b (**14** + TiCl₄) with spectrum n (**1** + TiCl₄) (cf. Figure 26). With increasing temperature the band at 1004 cm⁻¹ decrease, and a new band at 985 cm⁻¹ appears. Additionally, a band at 1526 cm⁻¹ arises at -15°C but the assignment is difficult to make. However, from the bands in the range 1060 - 950 cm⁻¹ some conclusions can be made concerning the changes of the $\nu(\text{C}-\text{O})$ vibrations.

The band at 1004 cm⁻¹, observed in Figure 26b, results from $\nu(\text{C}-\text{O})$ vibrations where the oxygen is coordinated to Ti (cf. **19** in Scheme 15). The bands at 1062 cm⁻¹ and 954 cm⁻¹ in Figure 26n can be assigned to $\nu_{\text{as}}(\text{C}-\text{O})$ and $\nu_{\text{s}}(\text{C}-\text{O})$ of the complex which is formed between **1** and TiCl₄. The possible structure of which (**9**) is given in Scheme 10.

During heating the complete reaction mixture bands at 1052, 1004, and 985 cm⁻¹ can be observed where only the first band does not change in intensity. At the end of reaction at -2°C only the bands at 1052 cm⁻¹ and 985 cm⁻¹ remain which can be related to $\nu_{\text{as}}(\text{C}-\text{O})$ and $\nu_{\text{s}}(\text{C}-\text{O})$ of a titanium complex similar to **9** and **19**. Obviously, TiCl₄ interacts with both reactants without preferring one of them. It should be mentioned at this point that the dark-red precipitate **19** which is formed at the beginning of reaction is slowly dissolved after addition of **1** and warming the reaction mixture. This suggests that reactant **1** interacts with complex **19** under partial elimination of TMSCl forming a new intermediate complex where **1** additionally coordinates via the released oxygen atoms to titanium. As a result two $\nu(\text{C}-\text{O})$ vibrations at 1052 cm⁻¹ and 985 cm⁻¹ are observable the band positions of which differ from those observed for complex **9** and **19**.

According the synthesis protocol the reaction mixture is quenched with aqueous HCl at the end of the reaction. Thus, the reaction was stopped after 4 hours at a temperature of 0°C, and aqueous HCl was added. The respective ATR-FTIR spectra of the reaction mixture

before and after quenching are shown in Figure 27. The most interesting features are the new bands at 1745 and 1719 cm^{-1} which indicate the formation of different carbonyl groups in this reaction step (cf. Figure 27b). After work-up with flash-chromatography, only one intensive carbonyl band at 1707 cm^{-1} is seen while the carbonyl bands at 1745 and 1719 cm^{-1} are vanished (cf. Figure 27c).

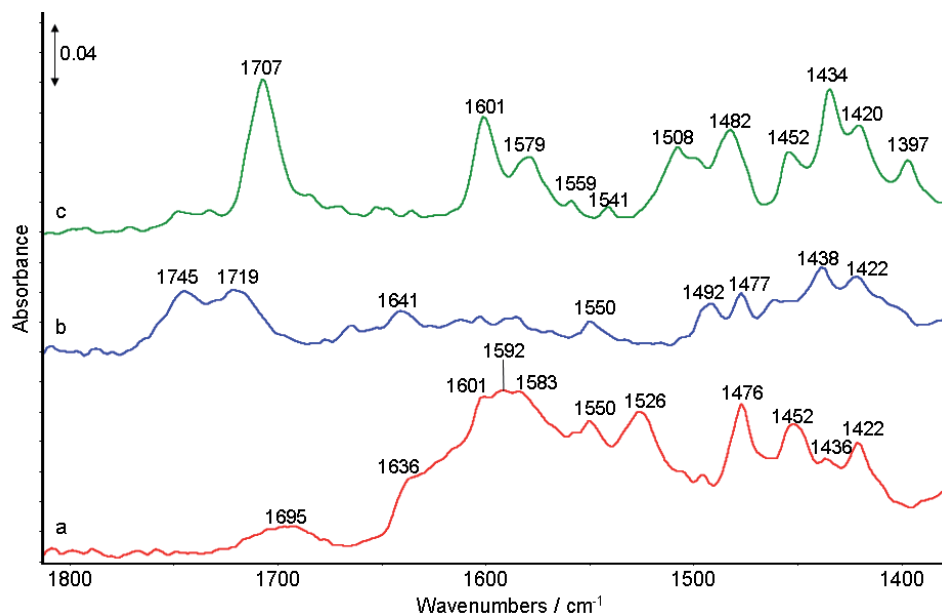


Figure 27. In situ-ATR-FTIR spectra obtained at the end of the reaction: (a) before and (b) after quenching with HCl(aq); (c) ATR-FTIR spectrum of the isolated solid product **17** after work-up with flash chromatography.

This demonstrates very clearly as already observed in the reaction of the ketenacetale **2b** with **1** that the work-up procedure is part of the reaction and influences significantly formation and nature of the final product. It is confirmed by X-ray analysis that the formed product **17** has a chromane-type structure substituted with an acetic acid methylester group, a hydroxyl group and an anilino group [104]. While the anilino group and the aromatic ring of the chromane-structure originally stem from the salicylideneaniline molecule, the oxygen-containing ring of the chromane-structure is formed by participation of both reactants. The acetic acid methylester group comes from **1**.

The formation of the chromane derivate **17** instead of a naphthalene derivate like **16** (cf. Scheme 14) can be explained by the nature of the intermediate formed titanium complex **19** which directs the formal addition of **1**. A possible transition state of the titanium complex is schematically shown in Scheme 14. The favoured elimination of TMSCl promotes a rearrangement of the rests on both terminal oxygen atoms of the titanium complex **19** in the presence of **1** leading finally, after work up with HCl and flash chromatography, to two molecules of **17**.

4.9 Influence of the reaction time

In Table 6 the yields of **3b**, **4b** and **17** obtained after 4 hours from the in situ experiments are compared with yields obtained by reference experiments carried out according to the protocol of Bunescu et al. [7]. It can be seen that the reaction was almost finished already after 4 hours when TMSOTf or **14** have been used. The rate of the reaction carried out with TiCl₄ seems to be lower which is indicated by the decreased yield. Interestingly, the use of AlCl₃ gives a slightly higher yield after 4h compared to TiCl₄, and after 14 hours the yield is significantly higher when the reaction is performed with AlCl₃. This is obviously caused by the stability of the intermediates which are formed between the Lewis acids and **1** or **2b**.

In the case of the utilisation of Al₂O₃ and TiO₂ no in situ experiments were carried out. The values of the reference experiments are shown in Table 6 for the sake of completeness.

Table 6: Yields obtained from the in situ experiments and reference experiments.

Experiment	Product	Yields / %	
		in situ monitoring (4h reaction time)	Reference experiments* (14h reaction time)
2b + TMSOTf + 1	4b	62	63
2b + TiCl ₄ + 1	3b	38	45-50
2b + AlCl ₃ + 1	3b	44	63
2b + TiO ₂ + 1	3b	—	13
2b + Al ₂ O ₃ + 1	3b	—	17
14 + TiCl ₄ + 1	17	82	85

*: The reference experiments were carried out by S. Reimann.

Additionally, the results indicate that the heating rate during the reaction is not an essential parameter as expected. Although a cooling to at least -50°C is required to reach adequate yields, the results indicate that the heating can proceed faster than in the reference experiments carried out according to the protocol of Bunescu et al. [7]. This implicates that the reaction time can be chosen below 14h. The minor influence of reaction temperature is also proved by simultaneously temperature measurements inside and outside the reactor during the reaction monitoring with optical spectroscopy. The temperature profiles are shown exemplary in Figure 28 by the means of the TiCl₄-experiment. The addition of **1** at -60°C provokes a rise of the temperature of approximately 20°C. This is caused because **1** is not cooled before and has room temperature when it is added to the reaction mixture. However, this rise does to seem to have a negative effect on the reaction yield and the temperature difference between reactor and cooling bath decreases with time.

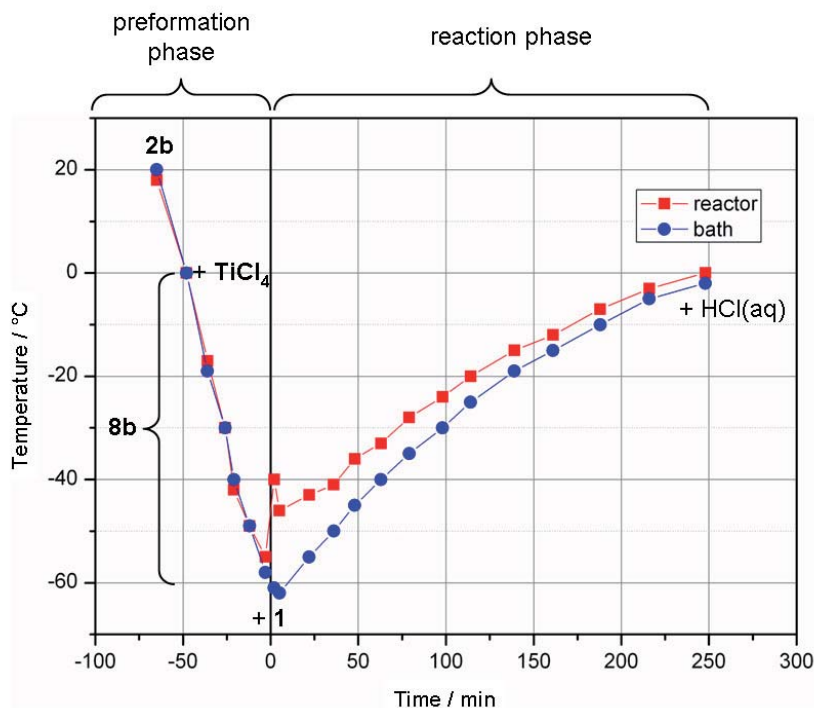


Figure 28: Temporal temperature development during the reaction measured inside the reactor and in the cooling bath: exemplary shown on the temperatures occurring in the **2b** + TiCl_4 + **1**-experiment; similar values obtained during the other in situ monitoring experiments.

4.10 Conclusion 2

The use of other Lewis acids like AlCl_3 , Al_2O_3 and TiO_2 in the cyclisation reaction was successfully proved. In the case of AlCl_3 the reaction mechanism is mostly similar to the mechanism which occurs when TiCl_4 is applied. However, smaller differences could be identified in the activation mode of **1** and **2b** with AlCl_3 by ATR-FTIR spectroscopy. The measured UV-vis spectra show major differences referring to the electronic state of the $d\pi$ -electrons in the formed complex. In general, **2b** does not seem to form such defined complexes with AlCl_3 as with **2b** with TiCl_4 in form of **8b**. However, the obtained yield with AlCl_3 was better than in case of TiCl_4 .

Al_2O_3 and TiO_2 can also be used as Lewis acid but the obtained yields are poor. This could be caused by mass transfer limitation. Obviously it is more difficult for the reactants to interact with a solid surface than with a dissolved metal cation due to steric hindrance. Furthermore, the amount of required activation energy for the reaction might be higher when solid acids like Al_2O_3 and TiO_2 are used. Thus, the complex adsorption / desorption behaviour of **1** and **2b** on the solids is an important factor as well. Interestingly, there is only a small difference between the obtained yields of **17** when the more acid Al_2O_3 or less acid TiO_2 is applied. Adsorbates could be detected only on Al_2O_3 . This shows a different adsorption / desorption behaviour on the solids. However, all these aspects have not been further investigated. Thus, a more exact discussion is difficult.

Although **14** has a great potential to form bis-chelate complexes the investigations show that the interaction with TiCl_4 occurs exclusively via the oxygen atom under the selected reaction conditions. This has been shown on the solid complex by ex situ UV-vis-DRS, ATR-FTIR and Raman spectroscopy as well as by in situ ATR-FTIR spectroscopy in the reaction slurry. Due to precipitation of the complex during the reaction a sufficient analysis by in situ UV-vis-transmission spectroscopy was not possible. However, the analysis by in situ ATR-FTIR spectroscopy showed clearly that also under reaction conditions only the oxygen atom of **14** interacts with TiCl_4 . For this reason the chromane-derivate **17** and no naphthalene-derivate **16** is obtained as reaction product. The yield of 82% is good but the product **17** contains two stereo centres which lead to a mixture of diastereomers. Although a diastereomere-pure reaction would be more preferable this study shows a fast and easy way for the synthesis of such complex molecules.

The presented current study showed that coupled in situ ATR-FTIR / UV-vis spectroscopy enables insight into the reaction mechanism. The linking of the in situ analysis with ex situ investigations is necessary for a proper interpretation of the measured in situ spectra. The obtained molecular structures from single crystal X-ray analysis in the case of **8a** and **8b** contribute essentially to the interpretation of the ex situ spectra. Furthermore, the results of the ATR-FTIR, UV-vis and Raman spectra measured ex situ in liquid phase are helpful for the interpretation of the spectra taken from adsorbates on the solids. The FTIR and UV-vis spectra of liquid and solid samples are comparable to each other which open the possibility to compare the mechanisms of single-phase and multi-phase systems. Constricting factors are the occurrence of fluorescence which perturbs Raman spectroscopy and of precipitates which perturbs UV-vis-transmission spectroscopy.

The in situ investigations also demonstrated that the reaction times can be reduced (cf. Table 6). Referring to the in situ ATR-FTIR spectra of the conversion of **14** with **1** (cf. Figure 26) it seems that the reaction takes place much faster than in the other experiments. Furthermore, the reaction temperature seems to play only a role when TMSOTf is used in the reaction of **14** and **2b**. From the spectroscopic point of view the temperature provokes no changes in the formation of **8a**, **8b**, **19** and the complex between **2b** and AlCl_3 . Additionally, the reaction of **19** with **1** seems to be less temperature depended as well.

Besides the optimisation of reaction time and temperature the further application would be the inclusion of other nitrogen-containing substrates and other Lewis acids in this type of reaction. A systematic test of other metal halides with respect to main group and

transition metals might be promising for increasing the yield. The use of the solid acid AlF_3 would be interesting as well because this acidic is even more acid than Al_2O_3 . However, mass transfer limitations and adsorption effects play an important role when solid acids are used which have to be considered in each case.

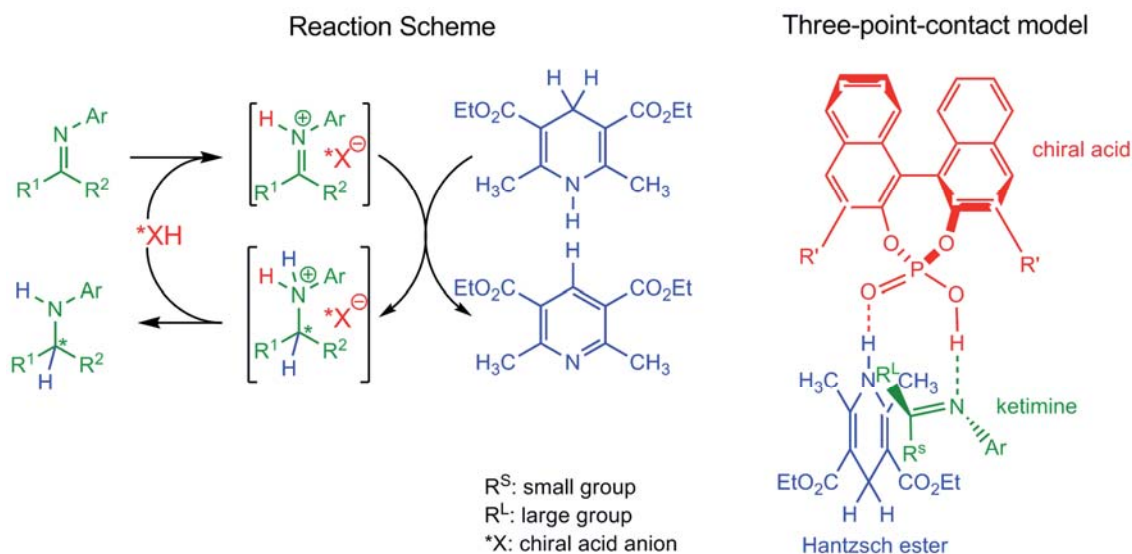
5. Heterogeneously catalysed asymmetric hydrogenation of imines: Reaction monitoring and mechanistic studies

The production of enantiopure amines deserved growing attention in the last years because chiral amines have a great potential as building blocks in drug synthesis as well as ligands in homogeneous catalysis [118, 119]. The heterogeneously catalysed asymmetric hydrogenation of C=N-double bonds is still a challenge. In the past, the majority of such hydrogenation reactions were found to be not stereoselective. Early works of Kindler et al. [120] described racemic hydrogenation catalysed by palladium black which was used in organic synthesis. Asymmetric hydrogenation of imines was restricted to homogeneous catalysis for many years. Novel approaches for the synthesis of such amines have been developed in organocatalysis [121-124] as well as in transition metal catalysis [125-127] wherein imines are important key-intermediates. The transition metal based approaches for catalysts for the asymmetric hydrogenation of acyclic imines can be divided into catalysts which work with molecular hydrogen and catalysts which are suitable for transfer hydrogenation. Several catalysts based on iridium, rhodium, ruthenium and palladium provide excellent yields for the asymmetric hydrogenation of acyclic imines applying molecular hydrogen, while the metal-based transfer hydrogenation catalysts give rather poor results [125]. However, these catalysts are expensive and difficult to prepare.

In heterogeneous catalysis, implementation of chirality was achieved by a combination of metal catalysts with chiral auxiliaries [128]. The application of supported noble metals (e.g. Pt, Pd) or Raney nickel combined with chiral modifiers such as cinchona alkaloids or tartrate, which are known to be asymmetric catalysts in the asymmetric hydrogenation of C=O double bonds, [129-132] did not result in high enantiomeric excesses using imines [133] as substrates. This may be caused by the E/Z-tautomerism of imines which was mentioned by Chan et al. [134] and Verdaguer et al. [135].

A new approach of stereoselective transfer hydrogenation of imines was the application of chiral phosphoric acid esters as organocatalysts [136-138]. The mechanism is based on the assumption that the ketimine is protonated by the chiral Brønsted acid which acts as catalyst. The resulting diastereomeric iminium ion pairs which may be stabilised by hydrogen bonding react with different reaction rates with the Hantzsch dihydropyridine giving an enantiomerically enriched amine and a pyridine derivative [136-138]. The exact mechanism is still under discussion, however, theoretical studies based on DFT methods [139,

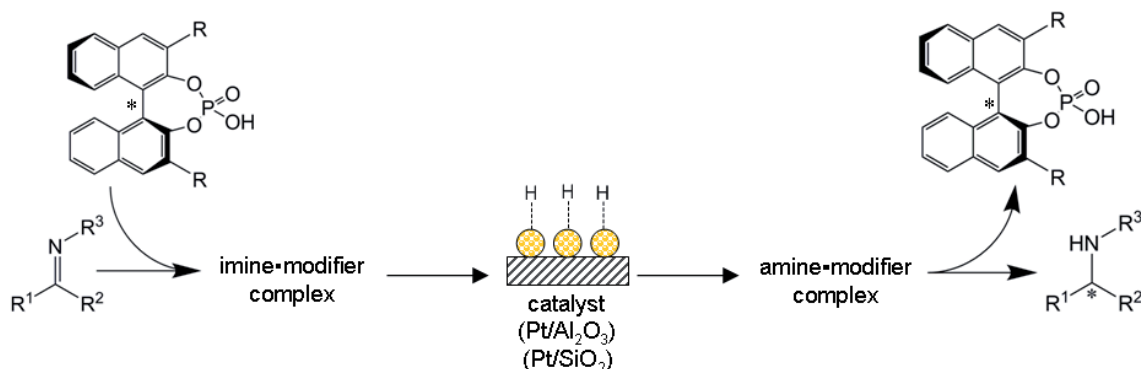
140] indicate a “three-point-contact model” (cf. Scheme 16). In consequence, the catalyst was classified to the group of difunctional organocatalysts [141].



Scheme 16. General reaction scheme of the organocatalytic transfer hydrogenation reactions.

The current investigation combines the organocatalytic with the heterogeneous catalytic approach. This gives the possibility to substitute the expensive Hantzsch dihydropyridine as hydrogen source by molecular hydrogen. While the molecular hydrogen shall be activated by a supported noble metal catalyst, the enantioselectivity is provided by chiral phosphoric acid esters. Two strategies are possible to realise this concept (cf. Figure 29):

Strategy 1: Hydrogenation of a diastereomeric complex



Strategy 2: Chiral modification of the surface of the catalyst

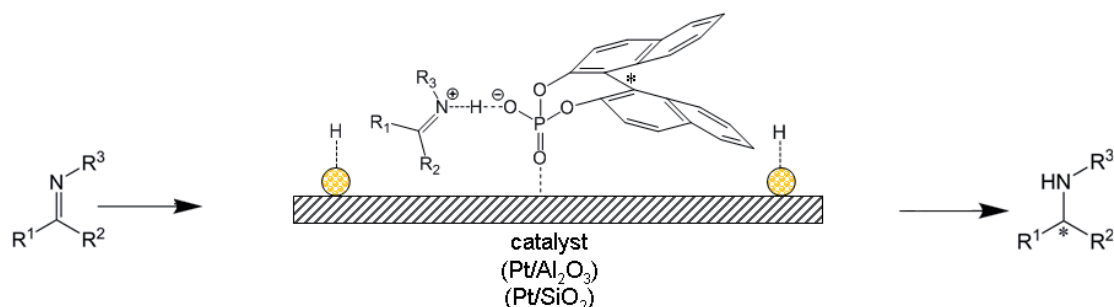


Figure 29. Strategies for the catalyst design for the heterogeneously catalysed asymmetric hydrogenation of imines to amines.

The first strategy is based on the formation of a diastereomeric ion pair in liquid phase between substrate and chiral modifier. The diastereomeric ion pair adsorbs together at the catalyst where the imine part is converted to an amine. In the last step the chiral modifier is separated from the product.

The second strategy is based on the immobilisation of the chiral modifier on the surface of the catalyst. Due to this there is no separation of modifier and product in liquid phase necessary and the amount of chiral modifier is presumably lower than in the other strategy. The diastereomeric ion pair will be formed in the vicinity of the catalyst surface where the hydrogenation takes place.

In general, the formation of an ion pair is the initial step in both strategies. Important questions are the behaviour of the diastereomeric ion pair in the vicinity of the surface of the catalyst and how to immobilise the chiral modifier on the surface of the catalyst. Therefore, the following investigations should elucidate the interactions between the substrate, the chiral modifier and the solid catalyst. The results may show which of both strategies is more adequate for the development of a heterogeneously catalysed asymmetric hydrogenation reaction.

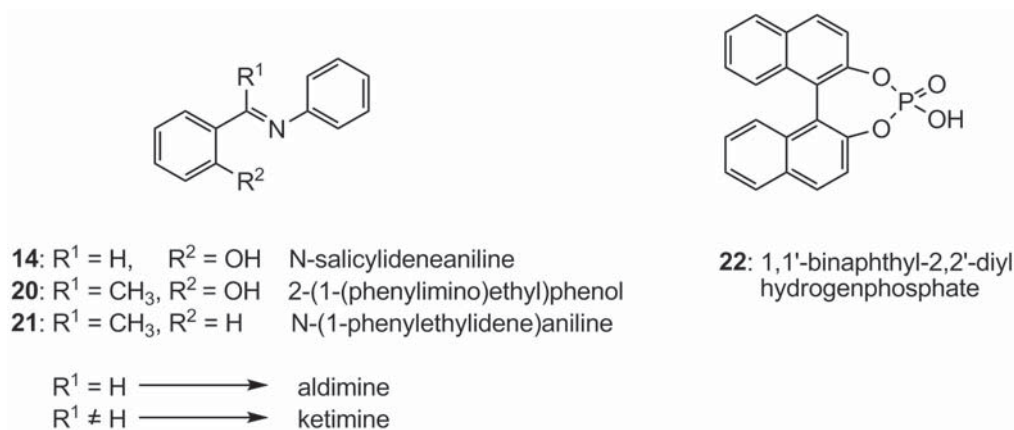
For a proper in situ analysis the knowledge of the spectroscopic properties of the reactants is essential. Here, the characterisation of the compounds is the basis of the investigation, followed by the study of interactions between them. The following chapters focus on the interaction of selected imines with the chiral modifier in liquid phase and the interaction of the imines and the chiral modifier with the surface of suitable hydrogenation catalysts.

5.1 Interaction of selected imines with the chiral modifier in liquid phase

Contrary to the protonation of ketimines ($R-N=CR_2$) the protonation of non-prochiral aldimines ($R-N=CH-R$) has been exhaustively investigated [142]. The difference between aldimines and ketimines concerning the molecular structure is shown in Scheme 17. Typically, the protonation of aldimines provokes a shift of the band of the $\nu(C=N)$ vibration to higher wavenumbers. This is a surprising fact. Normally, it would be expected that the $\nu(C=N)$ vibration is shifted to lower wavenumbers in the presence of a proton because the electron density of the $C=N$ double bond is lowered by the positive charge which decreases the double bond character. But in the experiment the opposite behaviour is observed: a shift of the band to higher wavenumbers indicates that the $C=N$ double bond becomes stronger in the

presence of a positive charge. This unusual behaviour has been explained with the rehybridisation model [113]. This model is based on the following assumptions:

1. The electrons of the n-orbital lone pair of the nitrogen forms a σ -bond to the proton which gives rise to a $\delta(\text{NH})$ vibration.
2. Rehybridisation of the nitrogen atom causes an increase of the force constant of the C=N double bond (s character of the bond increases, nitrogen atom rehybridises from sp^2 to sp).
3. Coupling of the $\nu(\text{C}=\text{N})$ and $\delta(\text{NH})$ vibrations causes a shift of $\nu(\text{C}=\text{N})$ to higher wavenumbers.
4. Deviation of vibrational states in the azomethine moiety [143].



Scheme 17. Schemes of the aldimine **14**, the ketimines **20** and **21** and of the model chiral modifier **22**.

Several studies show that the mechanism is sensitive to the structure of the applied aldimines, the strength of the used acid and also the type of solvent. If strong acids were used, the protonation was complete in the case of simple imines, independent on the nature of the solvent [144]. However, when the imine structure becomes more complex, the “levelling effect” of solvents becomes important [145]. This effect is caused by the extend of solvation of the ionic species. The protonated aldimine and the corresponding acid anion are surrounded by a solvent shell. Due to the solvent properties this solvent shell can differ which influences the charge stabilisation.

Only few studies exist about the protonation of ketimines. Allen and Roberts [146] studied the protonation of ketimines with trifluoroacetic acid by ^{15}N -NMR and UV-vis spectroscopy. Also Olah and Kreienbühl [147] studied the protonation of some ketimines in some extremely strong acids systems with ^1H NMR spectroscopy using SO_2 as diluent.

The following chapter will be focussed on the description of the interactions between imines **20**, **21** and chiral modifier **22** and the catalyst which are important for the elucidation of the catalytic cycle.

In order to investigate the interactions between the chiral modifier and ketimines in different solvents, three model substances were selected (cf. Scheme 17). Ketimine **21** was chosen because it is widely used as benchmark imine for the asymmetric hydrogenation with homogeneous catalysts. The phosphoric acid ester **22** is similar so the acids which are used as organocatalysts by Rueping et al. [136, 137] and Hoffmann et al. [138] in the transfer hydrogenation reaction of imines to amines. But contrary to the acids applied as organocatalysts, **22** has no bulky substituents in 4,4'-position. However, this should have no major influence on the acid strength and consequently the protonation ability because the acid proton is not localised close to the 4,4'-position. Furthermore a racemic mixture of **22** was applied for the investigations because it is not possible to distinguish between (R)- and (S)-enantiomers or different diastereomere pairs by the used spectroscopic methods. Hence, it is a suitable test substance for the protonation of ketimines.

The influence of solvents on the interaction between **21** and **22** has to be considered as well. Referring to the organocatalytic transfer hydrogenation of imines Hoffmann et al. [138] obtained the greatest enantiomeric excess in toluene and Rueping et al. [136] in benzene. Low or even no yields and no enantiomeric excess were obtained in methanol and ethanol while chlorinated solvents as CH_2Cl_2 and CHCl_3 gave modest yields and enantiomeric excesses. Considering these results the solvent should have a significant influence. For this reason the behaviour of **21** was exemplarily studied in different solvents. The studies have been carried out with ATR-FTIR and Raman spectroscopy. Both methods provide equal results which allows a commutative use of the spectra obtained from both methods.

Figure 30 shows the bands of the $\nu(\text{C}=\text{N})$, $\nu(\text{Ph}-\text{N})$ and $\nu(\text{Ph}-\text{C})$ vibrations of **21** in selected solvents. A distinct solvatochromatism can be observed indicated by different band positions of the $\nu(\text{C}=\text{N})$ vibration: 1640 cm^{-1} in CH_2Cl_2 , but 1630 cm^{-1} in $\text{CF}_3\text{CH}_2\text{OH}$. $\text{CF}_3\text{CH}_2\text{OH}$ is well known for its ability to form intermolecular hydrogen bonds with respective substrates. Hence, the appearance of the $\nu(\text{C}=\text{N})$ vibration at lower wavenumbers points to the formation of an intermolecular hydrogen bond between solvent and solute. In CH_3OH the band of the $\nu(\text{C}=\text{N})$ vibration is splitted. The band positions at 1640 and 1629 cm^{-1} indicate that a mixture of both states occurring in CH_2Cl_2 and $\text{CF}_3\text{CH}_2\text{OH}$ are present in CH_3OH . Typically, solvent-solute interactions are described as dipole-dipole interactions [148]. A more exact description based on non-empirical constants is difficult [149]. A proper

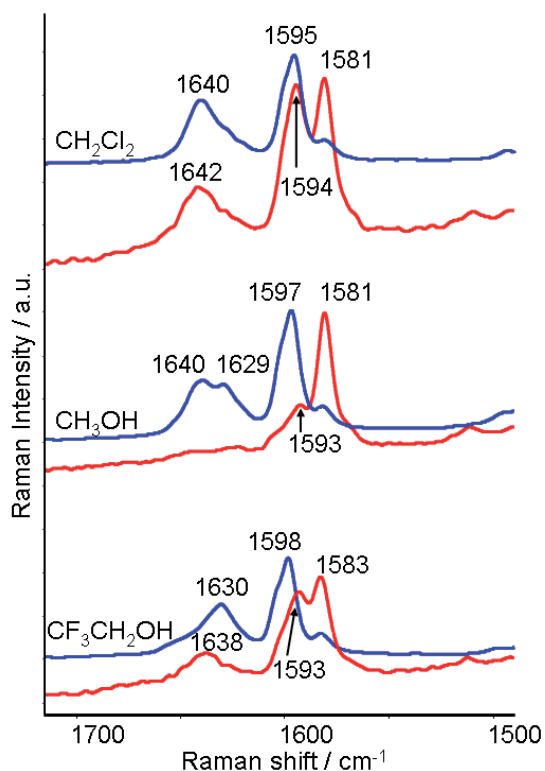


Figure 30: Raman spectra of **21** alone (blue) and equimolar mixtures of **21** and **22** (red) in selected solvents ($c = 0.5 \text{ mol}\cdot\text{L}^{-1}$).

prediction of solvent effects is neither possible on the basis of simple physical solvent characteristics, nor on theoretical expressions which could be used for calculations. Consequently, most solvent effects are described on the basis of empirical parameters of solvent polarity. In this case the description according to the Kamlet-Taft LSER (linear solvation energy relationships) equation (cf. Equation 3) can be made. Values for π^* , α and β are given in Table 7. Considering that α is prominent for the formation of hydrogen bonds from solvent to solute (HBD), the band position of the $\nu(\text{C}=\text{N})$ vibration can be indeed explained as an effect of hydrogen bond formation. The band is shifted to lower wavenumbers with increasing value of α .

$$XYZ = XYZ_0 + a\alpha + b\beta + s(\pi^* + d\delta) \quad (3)$$

- XYZ : band parameter where solvatochromatism takes place
 XYZ_0 : band parameter where solvatochromatism does not take place
 a, b, d, s : solvent-independent coefficients which reflect the susceptibility of the polarity terms upon XYZ
 π^* : polarity / polarisability
 α : hydrogen bond donor (HBD) ability
 β : hydrogen bond acceptor (HBA) ability
 δ : polarisability correction term (1.0 for aromatic, 0.5 for polyhalogenated and zero for nonchlorinated aliphatic solvents)

α and β give opportunity to distinguish between solvent-to-solute and solute-to-solvent hydrogen bond

Table 7. Empiric parameters of selected solvents referring to Kamlet et al. [148].

solvent	Kamlet-Taft parameters		
	π^*	α	β
CH ₃ OH	0.60	0.93	(0.62)
CF ₃ CH ₂ OH	0.73	1.51	0.00
CH ₂ Cl ₂	0.82	(0.30)	0.00
C ₇ H ₈ (Toluene)	0.54	0.00	0.11
C ₆ H ₆	0.59	0.00	0.10
CHCl ₃	0.58	(0.44)	0.00

The bands of the $\nu(\text{Ph-N})$ and $\nu(\text{Ph-C})$ vibrations are less influenced by the solvent. The band of the $\nu(\text{Ph-N})$ vibration occurs at 1595 cm^{-1} in CH_2Cl_2 , at 1597 cm^{-1} in CH_3OH , and at 1598 cm^{-1} in $\text{CF}_3\text{CH}_2\text{OH}$. The band of the $\nu(\text{Ph-C})$ vibration is less intense and occurs at 1581 cm^{-1} in CH_2Cl_2 and CH_3OH and at 1583 cm^{-1} in $\text{CF}_3\text{CH}_2\text{OH}$.

The investigation of the interactions between **21** and **22** was started in CH_2Cl_2 because this solvent does not form any hydrogen bonds to the solute. It is surprising that the band of the $\nu(\text{C=N})$ vibration remains nearly unchanged when **21** is mixed with **22** in an equimolar ratio in CH_2Cl_2 (cf. Figure 30). Also the $\nu(\text{Ph-N})$ vibration does change much due to protonation. The intense band at 1581 cm^{-1} results from **22**.

The interaction of **21** with **22** in $\text{CF}_3\text{CH}_2\text{OH}$ is similar to that in CH_2Cl_2 . Due to the presence of **22** the intermolecular hydrogen bond between **21** and the solvent is broken and the $\nu(\text{C=N})$ vibration appears at 1638 cm^{-1} which is approximately the same position as in CH_2Cl_2 .

As already mentioned above the band of the $\nu(\text{C=N})$ vibration of **21** is expected to be shifted to higher wavenumbers during interaction with acids. This is well known for the interaction of aldimines with acids. The shift is caused by rehybridisation of the nitrogen atom and deviation of the vibrational state of the azomethine moiety. But such a shift cannot be observed in the Raman spectra (cf. Figure 30) taken from the 1:1-mixtures of **21** and **22** in CH_2Cl_2 or $\text{CF}_3\text{CH}_2\text{OH}$ (the shift in $\text{CF}_3\text{CH}_2\text{OH}$ caused by the broken solvent-to-solute hydrogen bond shall be negotiated in this point). Obviously other mechanisms than rehybridisation take place for the charge stabilisation.

The interaction between **21** and **22** in CH_3OH is different. Due to interaction of **21** with **22** the $\nu(\text{C=N})$ band is completely vanished. This might be caused by a different charge stabilisation mechanism. The vanished $\nu(\text{C=N})$ band might indicate a partial break of the C=N double bond where the π -electrons of the double bond interact with **22** and form a carbocation. CH_3OH is a polar solvent which is able to stabilise polar species like ions with a solvate-shell. Furthermore the presence of a methyl group at the α -carbon atom of the C=N double bond enables the formation of a tertiary carbocation which can be better stabilised by hyperconjugation than a secondary carbocation which would result from the protonation of an aldimine.

Comparing the band positions of the $\nu(\text{C=N})$ vibration of **21** during interaction with **22** in the very polar solvent $\text{CF}_3\text{CH}_2\text{OH}$ and in the less polar solvent CH_2Cl_2 , the charge stabilisation mechanism takes place in a similar way. Fluorinated alcohols are well known to have special properties [150]. It seems that the solvatochromic parameter β (HBA) is the

limiting factor. Contrary to CH_3OH the value for this parameter is low for CH_2Cl_2 and $\text{CF}_3\text{CH}_2\text{OH}$. As a result, positively charged species such as protonated **21** cannot be solvated and a contact ion pair might be formed.

The spectroscopic results of the previous section could imply that the protonation does not take place in CH_2Cl_2 and $\text{CF}_3\text{CH}_2\text{OH}$ because the bands of the $\nu(\text{C}=\text{N})$, $\nu(\text{Ph}-\text{N})$ and $\nu(\text{Ph}-\text{C})$ vibrations do not change significantly during interaction with the acid. On the other hand there are additional vibrations which have to be considered. Thus, the characteristic vibrational bands of the PO_3H group of **22**, including the bands of the $\nu(\text{P}=\text{O})$, $\nu(\text{P}-\text{OH})$, and $\nu(\text{P}-\text{O}-\text{C})$ vibrations, should change when **22** dissociates. These vibrations occur mainly between 1250 cm^{-1} and 800 cm^{-1} as shown in Figure 31. They are not observable in $\text{CF}_3\text{CH}_2\text{OH}$ or CH_3OH due to strong solvent bands. But CH_2Cl_2 has only one band at 896 cm^{-1} which makes an investigation of the state of **22** possible.

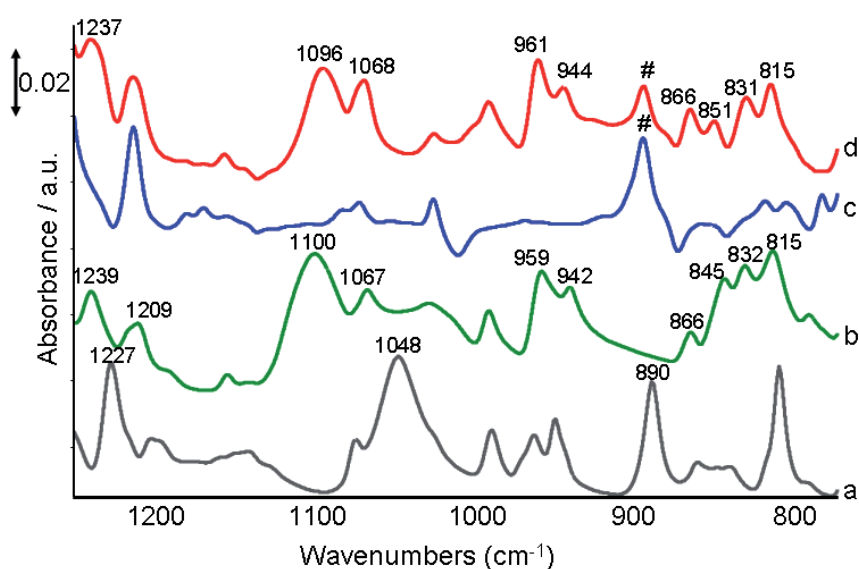


Figure 31. ATR-FTIR spectra of pure **21**, pure **22** and their mixtures: solid samples: (a) **22**, (b) 1:1-mixture of **22** and KOH; samples measured in CH_2Cl_2 at $c=0.5\text{ mol}\cdot\text{L}^{-1}$: (c) imine **21** and (d) 1:1-mixture of **21** and **22** (band of CH_2Cl_2 is marked with #).

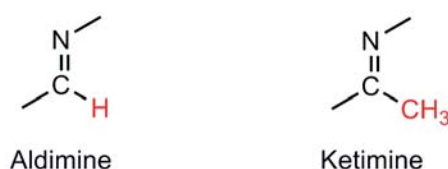
Up to now no complete band assignment of **22** or the corresponding acid anion is available. Therefore, the ATR-FTIR spectra of **22** (cf. Figure 31a) and of an 1:1-mixture of **22** and KOH (cf. Figure 31b) were measured. The mixture was prepared by dissolving **22** and KOH in equimolar amounts in CH_2Cl_2 followed by removal of the solvent by evaporation. Both spectra are measured in solid state because **22** cannot be properly dissolved in CH_2Cl_2 . Surprisingly, the salt of **22** (cf. Figure 31b) has a good solubility in CH_2Cl_2 . But, for a better comparison the spectrum of the solid salt is shown.

The spectrum of **22** (cf. Figure 31a) shows three characteristic bands at 1227 cm^{-1} , 1048 cm^{-1} , and 890 cm^{-1} . These vibrations can be assigned to $\nu(\text{C-O})$, $\nu(\text{P-O-C}_{\text{arom}})$, and $\nu((\text{HO})\text{P-O-C}_{\text{arom}})$ [151, 152]. When **22** is treated with KOH these vibrations are vanished in the spectrum (cf. Figure 31b).

Instead, new vibrations appear at 1239 cm^{-1} and 1209 cm^{-1} which might be assigned to the $\nu_{\text{as}}(\text{PO}_2^-)$ vibration and at 1100 cm^{-1} and 1067 cm^{-1} which might be the $\nu_{\text{s}}(\text{PO}_2^-)$ vibration. The splitting the $\nu_{\text{s}}(\text{PO}_2^-)$ and $\nu_{\text{as}}(\text{PO}_2^-)$ vibrations might be an effect of Fermi resonance. Other typical bands appear at 959 cm^{-1} and 942 cm^{-1} which could be dedicated to $\nu(\text{P-O-C})$ vibrations and at 866 cm^{-1} , 845 cm^{-1} , 832 cm^{-1} and 815 cm^{-1} which are obviously ring deformation vibrations of the aromatic rings. The appearance of these bands is very characteristic for the formation of the acid anion (cf. Figures 31b and 31d).

Comparing the spectra of the 1:1-mixture of **21** and **22** (cf. Figure 31d) and the 1:1-mixture of **22** and KOH (cf. Figure 31b) that the same features are observable. This indicates that **22** is dissociated during interaction with **21**.

Thus, the situation in CH_2Cl_2 is the following: the imine vibrations between 1700 cm^{-1} and 1500 cm^{-1} indicate no interaction between **21** and **22** (cf. Figure 30: Raman spectra). In contrast, the acid vibrations between 1250 cm^{-1} and 800 cm^{-1} (cf. Figure 31: ATR-FTIR spectra) indicate interaction. But these two opposed observations can be explained. First of all the rehybridisation effect has to be examined in more detail. As mentioned before the charge stabilisation by the rehybridisation effect is based on the coupling of the $\nu(\text{C=N})$ and $\delta(\text{NH})$ vibrations which causes a shift of the $\nu(\text{C=N})$ vibration band to higher wavenumbers, a change of the force constant of the C=N double bond due to rehybridisation of the nitrogen atom and a deviation in the vibrational states of the complete azomethine moiety. It has to be considered that a change in the mass distribution may have great impact on the vibrational states of the molecule (cf. Scheme 18).



Scheme 18: Structures of azomethine and azomethyl groups.

The hydrogen atom in the aldimine has a fraction of 3.8 wt% of the azomethine group while for the ketimine the methyl group which is located in the same position has a fraction of 36.6 wt%. It has been shown in previous works that the azomethine moiety is very sensitive to

changes in mass. If the mass is varied by substitution of the hydrogen atom by a deuterium atom, the shift of the $\nu(\text{C}=\text{N})$ vibration is decreased by $\sim 30 \text{ cm}^{-1}$ to $0\text{-}10 \text{ cm}^{-1}$ [153-157]. Even the unprotonated $\nu(\text{C}=\text{N})$ vibration is very sensitive to mass changes like substitution of atoms by isotopes as deuterium or ^{15}N [112]. Thus, the rehybridisation mechanism is very sensitive to changes in mass. If a single hydrogen atom is replaced by a methyl group (which is fifteen times heavier), the rehybridisation mechanism becomes inefficient and other mechanisms for charge stabilisation are favoured.

Such a different stabilisation can occur via a backbond to the anion of the acid. This interaction is based on the “levelling effect” which was described first by Blatz et al. [158]. They explained solvatochromic shifts of the absorption maxima in the UV-vis spectrum of protonated N-retinylidene-n-butylamine by different distances between the protonated imine and the acid anion when the solvents are varied. The importance of this effect on the protonation of imines referring to proton transfer (localisation of the proton between acid anion and imine), has been outlined in the studies of Bissonnette et al. [145, 159]. It is evident that in “non-levelling” solvents like CH_2Cl_2 a charge stabilisation occurs via charge transfer between protonated imine and acid anion. This requires a relatively small distance between

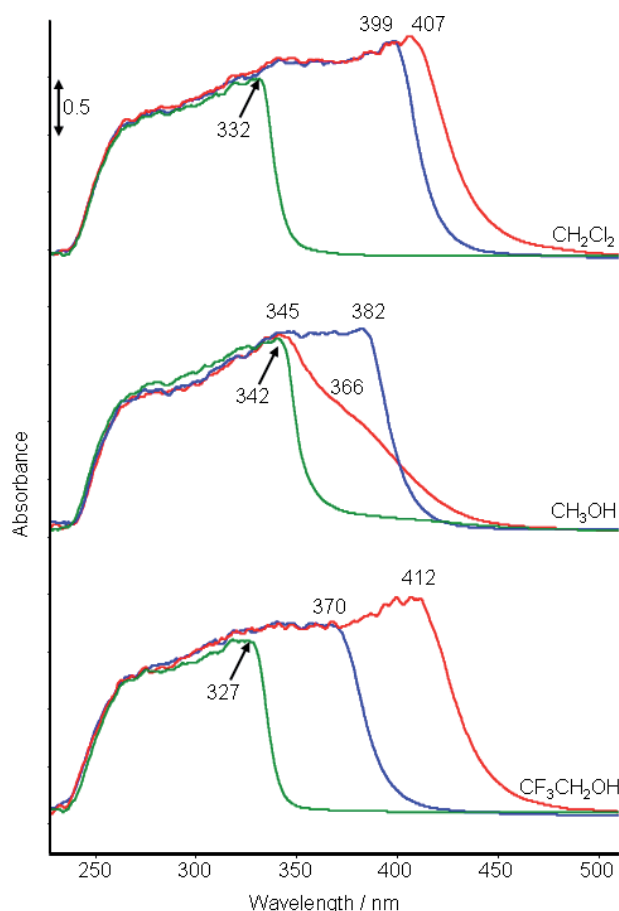


Figure 32. UV-vis spectra of **21** alone (blue), **22** alone (green) and 1:1-mixtures (molar ratio) of **21** and **22** (red) in selected solvents ($c=0.5 \text{ mol}\cdot\text{L}^{-1}$).

the anion and the protonated imine. According to the previous conclusions this should be the case in CH_2Cl_2 and likely as well in $\text{CF}_3\text{CH}_2\text{OH}$. On the other hand this effect should not be present in CH_3OH . Another method for the observation of interactions between charged species is UV-vis spectroscopy which was used to elucidate the presence of a backbond in the current study.

Figure 32 shows the UV-vis spectra of **21** in the three solvents CH_2Cl_2 , CH_3OH and $\text{CF}_3\text{CH}_2\text{OH}$. The absorption maximum of **21** appears in CH_2Cl_2 at 399 nm. In CH_3OH and $\text{CF}_3\text{CH}_2\text{OH}$ the maximum is shifted with increasing

HBD α values (cf. Table 7) to shorter wavelengths and appears at 382 nm and 370 nm, respectively. As already observed in the Raman spectra (cf. Figure 30) a solvochromic shift takes place.

In order to study the interaction between **21** and **22**, the spectra of **21** and **22** alone and of the 1:1 mixtures of both compounds are also included in Figure 32. Referring to Brocklehurst [160] the absorption maximum should shift to longer wavelengths when **21** is interacting with an acid. This was shown on *N*-benzylideneaniline mixed with sulphuric acid in ethanol. The maximum of the band of **22** occurs in the UV-vis spectra at shorter wavelengths than the maximum of **21**. Thus, the band of a protonated species should not be overlaid by the band of **22**.

A shift to longer wavelengths is observable for the 1:1-mixture of **21** and **22** in case of CH_2Cl_2 and $\text{CF}_3\text{CH}_2\text{OH}$ with the absorption maxima at 407 nm in CH_2Cl_2 and at 412 nm in $\text{CF}_3\text{CH}_2\text{OH}$. The extent of shifting and the increasing intensity suggest that an interaction between protonated imine and acid anion via a charge transfer. This requires a short distance between the charged species and occurs in solvents which poorly solvate charged species (cf. Figure 33).

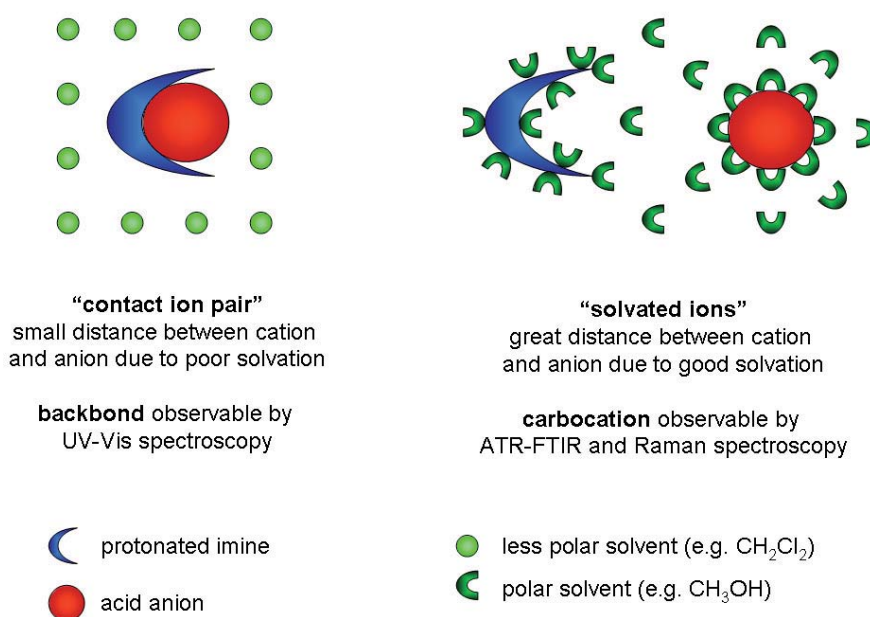


Figure 33. Different modes of solvation: contact ion pair in CH_2Cl_2 and solvated ions in CH_3OH .

In contrast, this effect does not take place in CH_3OH . Here the absorption maximum of the 1:1 mixture is shifted to lower wavelengths and appears at 345 nm. An additional shoulder can be observed at 366 nm (cf. Figure 31). The shift to shorter wavelengths might indicate a larger distance between the acid anion and the protonated imine due to the levelling effect of CH_3OH (cf. Figure 33). Hence no charge transfer is possible. These results confirm the

conclusions made from the Raman spectra that a different charge stabilisation mechanism takes place in CH₃OH.

Recently, Fleischmann et al. [161] published a study on the interaction of similar aldimines and ketimines with a similar acid. The interaction was studied in deuterated toluene by NMR spectroscopy. They report the parallel existence of ion pairs (N–H⁺⋯O[–]) in which the proton is located near to the nitrogen atom of the imine, and hydrogen bonding ($\bar{N} \cdots \text{HO}$) in which the proton is localised closer to the acid. The extent of both kinds of interactions depends on temperature. But this has been shown already by Le-Thanh et al. [144] for the interaction of N-propylidene propanamine with mineral acids.

In the current study the presence of hydrogen bonding in the interaction of **21** with **22** could not be observed with the applied methods. On the other hand the presence of the backbond in the ion pair is not mentioned by Fleischmann et al. [161]. This shows that the nature of the interaction is rather complex and its description depends also on the applied analytical methods. A direct comparison of the results obtained from NMR spectroscopy with the results obtained from optical spectroscopy seems to be difficult in particular when different solvents and reagents are used.

5.2 Interaction of selected imines with the catalyst surface

The adsorption of N-salicylideneaniline **14**, 2-(1-(phenylimino)ethyl)phenol **20** and N-(1-phenyl-ethylidene)aniline **21** (cf. Scheme 17) on Pt/Al₂O₃ and Pt/SiO₂ was investigated, too. Imines are bases and interact with Lewis acids as well as with Brønsted acids [162]. This leads to the question if imines interact with solid Lewis acids in the same manner as with Lewis acids in liquid phase. Furthermore, adsorbates can play a role within the reaction mechanism and can contribute to the deactivation of the catalyst.

Two catalysts have been applied for this study: an Lewis acid Pt/Al₂O₃ catalyst and a rather neutral Pt/SiO₂ catalyst. Different supports might have an effect on the adsorption of the substrates at the metal surface as well as on the support itself.

Because **14** is well characterised by UV-vis and FTIR spectroscopy the adsorption studies of imines were started with this non-prochiral imine. FTIR-transmission spectroscopy from self-supporting wafers of the catalyst is a suitable method to show how **14** adsorbs on the Lewis acid catalyst Pt/Al₂O₃ [40].

Figure 34 shows the spectra of **14** adsorbed on Pt/Al₂O₃, Al₂O₃ and Pt/SiO₂ and the ATR-FTIR spectrum of **14** dissolved in CCl₄ (*c* = 0.5 mol·L⁻¹). The bands at 1620, 1593,

1573, and 1283 cm^{-1} (cf. Figure 34a) can be assigned to $\nu(\text{C}=\text{N})$, $\nu(\text{Ph}-\text{N})$, $\nu(\text{Ph}-\text{C})$ and $\nu(\text{Ph}-\text{OH})$ vibrations [105, 109, 163]. Compared with other aldimines the band of the $\nu(\text{C}=\text{N})$ occurs at a relatively low wavenumbers which is caused by the formation of an intramolecular hydrogen bond formed between the hydrogen atom of the hydroxyl group and the nitrogen atom ($-\text{O}-\text{H}\cdots\text{N}$) [163]. When **14** is separately adsorbed on $\text{Pt}/\text{Al}_2\text{O}_3$, these bands vanish and new characteristic bands occur at 1638, 1603, 1539, and 1213 cm^{-1} . The band at 1638 cm^{-1} can be assigned to the $\nu(\text{C}=\text{N})$ vibration shifted to higher wavenumbers due to interaction of the nitrogen atom with the Lewis acid support. The band shift is obviously caused by a mechanism which is similar to the rehybridisation effect which occurs when aldimines interact with protons. This is also in line with results already described by Ortiz-Hernandez and Williams [114] of the investigation of butyronitrile adsorption and hydrogenation on $\text{Pt}/\text{Al}_2\text{O}_3$ using ATR spectroscopy. Thus, the presence of an adsorbed imine intermediate was suggested by the appearance of bands in the $\text{C}=\text{N}$ and $\text{N}-\text{H}$ stretching regions whereas a characteristic intense band at 1635 cm^{-1} was observed resulting from an imine-type intermediate. The new band occurring at 1539 cm^{-1} was also observed by Ortiz-Hernandez and Williams [114] in the adsorption of butyronitrile and is assigned to a band characteristic for adsorbed aldimines. The band at 1603 cm^{-1} (cf. Figure 34b) is a band which appears also in the corresponding amine and can be assigned to $\nu(\text{C}=\text{C})$ vibration of the aromatic rings. Finally the band at 1213 cm^{-1} might be the $\nu(\text{Ph}-\text{OH})$ vibration shifted to lower wavenumbers due to adsorption.

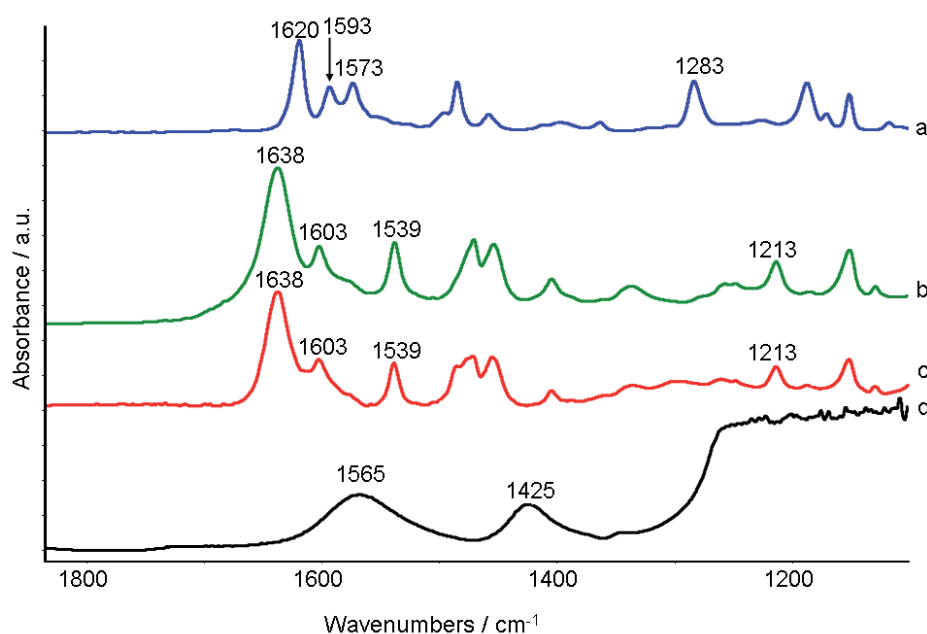


Figure 34. (a) ATR-FTIR spectrum of **14** in CCl_4 ($c=0.5 \text{ mol}\cdot\text{L}^{-1}$); FTIR-transmission spectra (measured from self-supporting wafer) of separately adsorbed **14**: (b) difference spectrum of **14** on $\text{Pt}/\text{Al}_2\text{O}_3$ (spectrum of pure $\text{Pt}/\text{Al}_2\text{O}_3$ subtracted), (c) difference spectrum of **14** on Al_2O_3 (spectrum of pure Al_2O_3 subtracted) and (d) difference spectrum of **14** on Pt/SiO_2 (spectrum of pure Pt/SiO_2 subtracted).

Another band can be observed clearly at 364 nm. The intensity of this band is less strong compared the band of the second $\pi \rightarrow \pi^*$ transition at 315 nm but can be assigned to $\pi \rightarrow \pi^*$ transition as well. Another very weak broad band occurs around at 505 nm which might indicate that the negative charge at the oxygen atom is partly delocalised. Thus, the intermolecular hydrogen bond of **14** formed between the hydrogen atom of the hydroxyl group and the nitrogen atom [163] is broken in adsorbed **14**.

The spectrum of **14** adsorbed on Pt/Al₂O₃ is very similar to the spectrum of **14** adsorbed on Al₂O₃. The band at 271 nm might be a combination of the two $\sigma \rightarrow \pi^*$ transitions and the band at 345 nm a combination of the two $\pi \rightarrow \pi^*$ transitions. Also here a weak shoulder can be observed at 505 nm.

The results obtained from the UV-vis-DRS and FTIR-transmission spectra indicate that both, the nitrogen atom and the oxygen atom (cf. Scheme 19), are involved in the adsorption mechanism of **14** on Pt/Al₂O₃ as well as on Al₂O₃ which seems to be the same. Presumably, the proton is removed from the hydroxyl group and is stabilised by interaction with the oxidic oxygen atoms of the support. The negative charged oxygen atom of **14** interacts with the coordinatively unsaturated aluminium atoms of the Lewis acid support. Additionally, the electron lone pair of the nitrogen atom interacts with the aluminium atoms of the Lewis acid support as well.

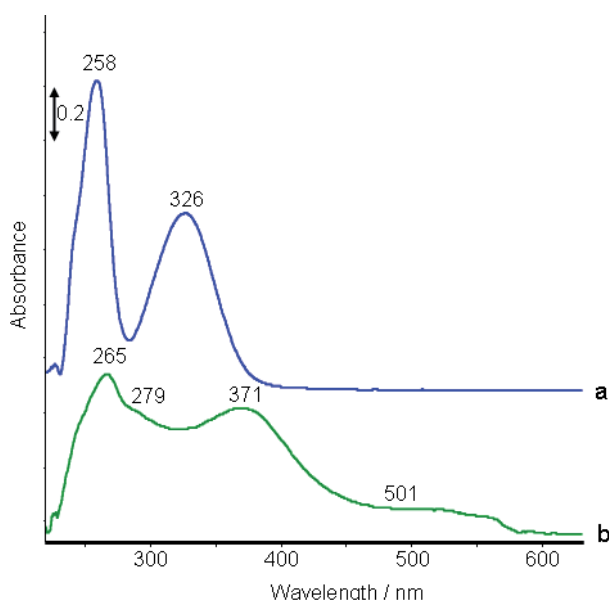


Figure 36. UV-vis-transmission spectra of **20** dissolved in (a) CH₂Cl₂ ($c = 5 \cdot 10^{-4} \text{ mol} \cdot \text{L}^{-1}$) and (b) UV-vis-DRS spectrum of **20** adsorbed on Pt/Al₂O₃.

is less intense than the band of the $\sigma \rightarrow \pi^*$ transition.

Figure 36 shows the UV-vis-DRS spectrum of **20** adsorbed on Pt/Al₂O₃. The UV-vis spectra of **20** taken in CH₂Cl₂ is shown for comparison as well. The structure of **20** is similar to **14** but has a methyl group instead of a hydrogen atom at the α -carbon atom of the C=N double bond. Analogous to **14**, **20** can potentially interact via two sites – the nitrogen and the oxygen atom – on the catalyst surface. Contrary to the spectrum of **14** in CH₂Cl₂ the spectrum of **20** shows only two bands at 258 nm and 326 nm which can be assigned to $\sigma \rightarrow \pi^*$ and $\pi \rightarrow \pi^*$ transitions. Surprisingly the band of the $\pi \rightarrow \pi^*$ transition

The spectrum of **20** adsorbed on Pt/Al₂O₃ shows a band at 265 nm with a shoulder at 279 nm. Similar to the spectrum of adsorbed **14**, these bands can be assigned to $\sigma \rightarrow \pi^*$ transitions. The band at 371 nm should be the same $\pi \rightarrow \pi^*$ transition which appears in adsorbed **14** at 364 nm. Position and relative intensity of both bands are rather similar to each other. Again a weak band appears at 501 nm (505 nm in adsorbed **14**). Hence, referring to the UV-vis-DRS spectra, the adsorption behaviour of **14** and **20** is comparable to each other. In order to validate the previous conclusions, Pt/Al₂O₃ containing adsorbed **20** was pressed to a self-supporting wafer and analysed with FTIR-transmission spectroscopy.

The spectrum of **20** adsorbed on Pt/Al₂O₃ measured from a self-supporting wafer is shown in Figure 37. An ATR-FTIR spectrum of **20** dissolved in CCl₄ is shown for comparison as well. This ATR-FTIR spectrum shows bands at 1614, 1594, and 1574 cm⁻¹ which can be related to the $\nu(\text{C}=\text{N})$, $\nu(\text{Ph}-\text{N})$, and $\nu(\text{Ph}-\text{C})$ vibration modes. The band of the $\nu(\text{C}=\text{N})$ vibration occurs at a relatively low position which is caused by the formation of an intramolecular hydrogen bond like observed in the spectrum of in **14** (cf. Figure 34). One of the three bands at 1310, 1255, and 1206 cm⁻¹ should be the $\nu(\text{Ph}-\text{OH})$ vibration. The position of the band at 1206 cm⁻¹ is too low considering that the $\nu(\text{Ph}-\text{OH})$ vibration of **14** occurs at 1283 cm⁻¹ (cf. Figure 35). The band at 1255 cm⁻¹ has too low band intensity and an asymmetric shape. Therefore, the band at 1310 cm⁻¹ should be the $\nu(\text{Ph}-\text{OH})$ vibration.

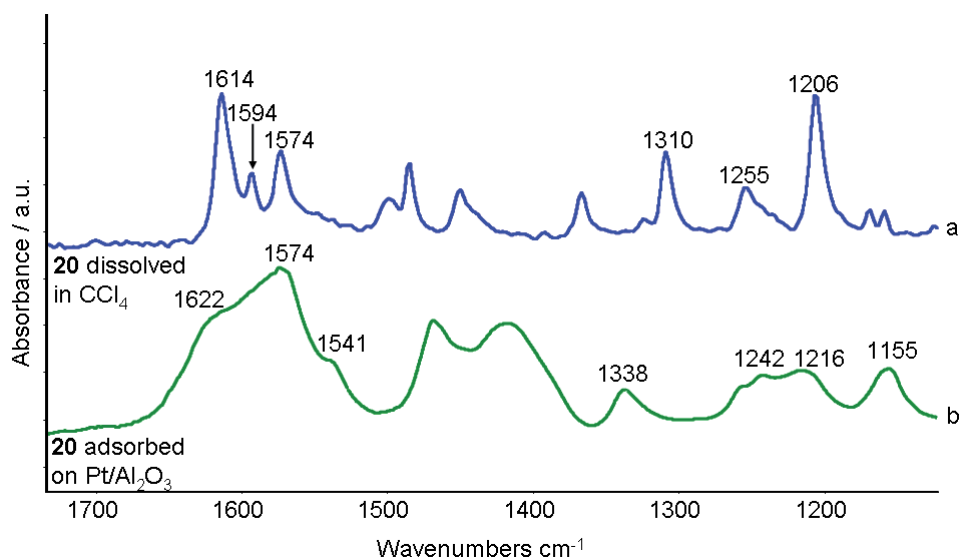


Figure 37. (a) ATR-FTIR spectrum of **20** dissolved in CCl₄ ($c=0.5 \text{ mol}\cdot\text{L}^{-1}$) and (b) difference FTIR-transmission spectrum of **20** separately (measured from self-supporting wafer) adsorbed on Pt/Al₂O₃ (the spectrum of pure Pt/Al₂O₃ is subtracted).

The spectrum of adsorbed **20** shows a band at 1622 cm⁻¹ which is partly overlaid by an intense band occurring at 1574 cm⁻¹. This band overlays also a band at 1541 cm⁻¹. Other

bands occur at 1338, 1242, 1316, and 1155 cm^{-1} . Considering the fact that the formation of a hydrogen bond shifts the band position of the $\nu(\text{C}=\text{N})$ vibration of about 8-10 cm^{-1} to lower wavenumbers, the band at 1622 cm^{-1} could be the $\nu(\text{C}=\text{N})$ vibration of **20** where the intramolecular hydrogen bond (formed via $\text{N}\cdots\text{H}-\text{O}$) in the molecule is obviously broken by adsorption.

The band at 1574 cm^{-1} is presumably a combination of the $\nu(\text{Ph}-\text{N})$ and $\nu(\text{Ph}-\text{C})$ vibration modes. The position of the band at 1541 cm^{-1} is very similar to the position of the characteristic band of adsorbed imines which was also observed in the adsorption of **14** at 1539 cm^{-1} (cf. Figure 35b and 34c) and in the adsorption of butyronitrile at 1535 cm^{-1} [40, 114]. The band of the $\nu(\text{Ph}-\text{OH})$ vibration occurring at 1310 cm^{-1} of **20** in CCl_4 is vanished completely and should be shifted to lower wavenumbers like shown for adsorbed **14** (cf. Figure 34). Hence, the band at 1338 cm^{-1} can be excluded as $(\text{Ph}-\text{O})$ vibration of adsorbed **20**. Furthermore, the bands at 1242 and 1216 cm^{-1} seem to be the same bands which occur at 1255 and 1206 cm^{-1} in CCl_4 . This leads to the conclusion that the band at 1155 cm^{-1} should be prominent for the $(\text{Ph}-\text{O})$ vibration of adsorbed **20**. Generally, the results of the FTIR-transmission spectrum fit to the results of the UV-vis-DRS spectrum of **20** adsorbed on $\text{Pt}/\text{Al}_2\text{O}_3$. Furthermore, the adsorption behaviour of **20** on $\text{Pt}/\text{Al}_2\text{O}_3$ is comparable with that of **14**.

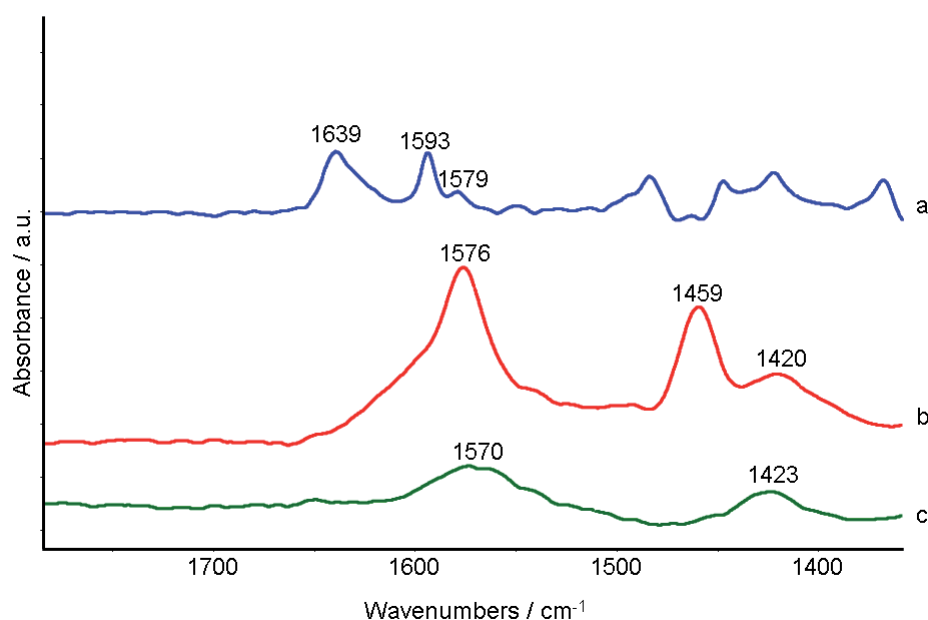


Figure 38. (a) ATR-FTIR spectrum of **21** in CH_2Cl_2 ($c = 0.5 \text{ mol}\cdot\text{L}^{-1}$); difference FTIR-transmission spectra of **21** (measured as self-supporting wafer): (b) adsorbed on $\text{Pt}/\text{Al}_2\text{O}_3$ (spectrum of pure $\text{Pt}/\text{Al}_2\text{O}_3$ subtracted) and (c) **21** adsorbed on Pt/SiO_2 (spectrum of pure Pt/SiO_2 subtracted).

The spectra of adsorbed **21** on $\text{Pt}/\text{Al}_2\text{O}_3$ and Pt/SiO_2 are shown in Figure 38. The spectrum of **21** in CH_2Cl_2 ($c = 0.5 \text{ mol}\cdot\text{L}^{-1}$) is included for comparison. Characteristic bands occur at 1639,

1593, and 1579 cm^{-1} which can be assigned to the $\nu(\text{C}=\text{N})$, $\nu(\text{Ph}-\text{N})$ and $\nu(\text{Ph}-\text{C})$ vibration modes. Contrary to the previous examples the FTIR-transmission spectrum of **21** adsorbed on $\text{Pt}/\text{Al}_2\text{O}_3$ (cf. Figure 38b) shows only three broad bands at 1576 , 1459 , and 1420 cm^{-1} . A distinct assignment of these bands is not possible. The FTIR-transmission spectrum of **21** adsorbed on Pt/SiO_2 (cf. Figure 38c) shows even only two broad bands at 1570 and 1423 cm^{-1} .

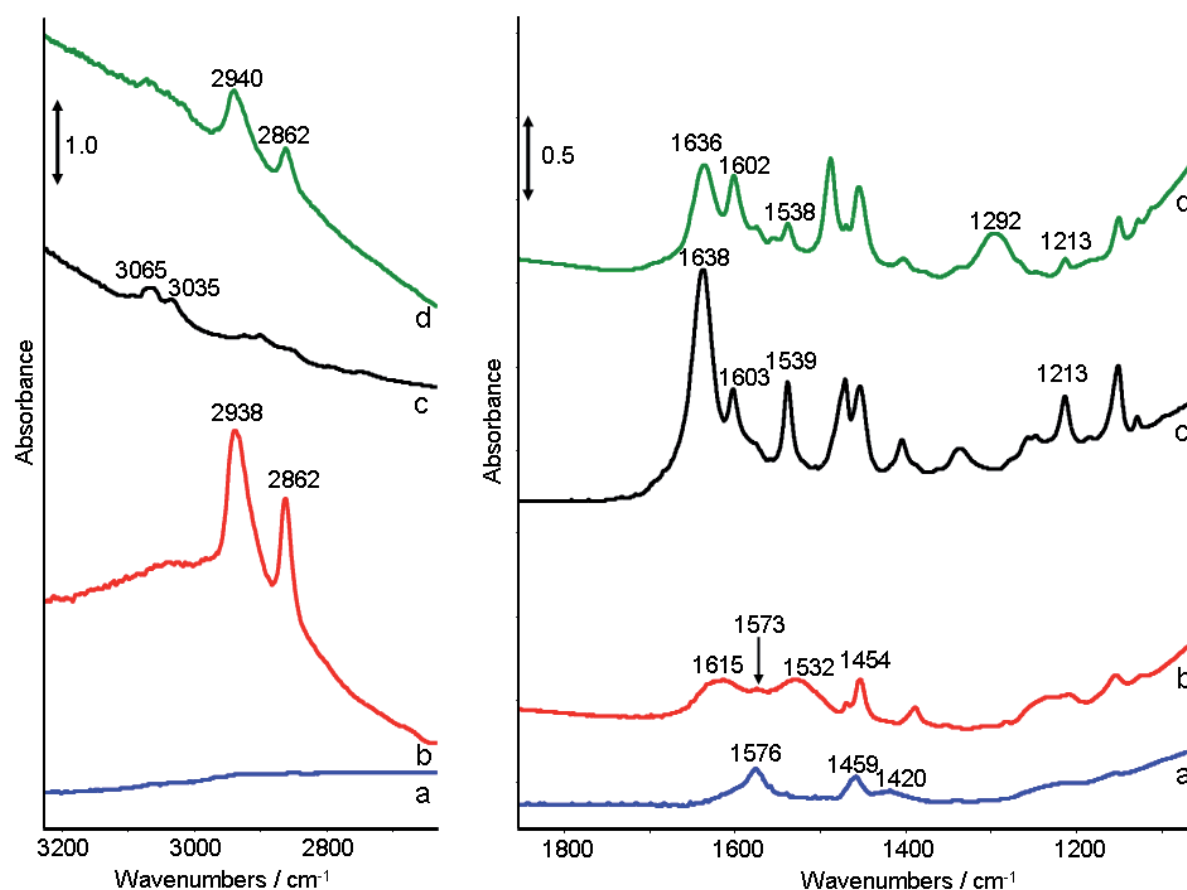


Figure 39. Difference FTIR-transmission spectra of adsorbed imines (measured from self-supporting wafer): (a) **21** adsorbed on $\text{Pt}/\text{Al}_2\text{O}_3$ before and (b) after hydrogenation reaction; (c) **14** adsorbed on $\text{Pt}/\text{Al}_2\text{O}_3$ before and (d) after hydrogenation reaction; all spectra after subtraction of the spectrum of pure $\text{Pt}/\text{Al}_2\text{O}_3$.

Up to this point the discussion was about imines separately adsorbed on catalysts and analysed before the hydrogenation reaction took place. The spectra taken from used catalysts after the hydrogenation reaction of **14** and **21** took place are displayed in Figure 39. The spectra of the separately adsorbed imines are shown for comparison (cf. Figures 39a and c). In the case of adsorbed **21** the changes after reaction are rather obvious: new bands occur at 2938 , 2862 , 1615 , and 1532 cm^{-1} (cf. Figure 39b). The bands at 2938 and 2862 cm^{-1} can be assigned to $\nu_{\text{as}}(\text{C}-\text{H})$ and $\nu_{\text{s}}(\text{C}-\text{H})$ vibration modes. This indicates that one or both phenyl rings of **21** are reduced to cyclohexyl rings during the hydrogenation reaction. The other two bands at 1615 and 1532 cm^{-1} indicate a rearrangement of the adsorbed molecule. On the first view the differences in the case of adsorbed **14** after reaction are not so distinct compared

with adsorbed **21** (cf. Figure 39d). Three additional bands at 2940, 2862, and 1292 cm^{-1} can be observed. The appearance of bands at 2940 and 2862 cm^{-1} indicate the hydrogenation of at least one phenyl ring as also observed in case of **21**. In general, the hydrogenated species seem to have less desorption tendency than the imines. Otherwise the spectra of the imines and not of the hydrogenation products would be observed on the catalysts.

Summarising the results of these experiments it can be stated that imines adsorb on the Lewis acid $\text{Pt}/\text{Al}_2\text{O}_3$ catalyst in a different manner than on the neutral Pt/SiO_2 catalyst. The nature of the support has fundamental influence on the adsorption behaviour. The band intensities of the spectra indicate that the amount of adsorbed species is less on Pt/SiO_2 . The additional hydroxyl group in the structure of **14** and **20** has also influence on the adsorption mode and provokes the adsorption via two sites of the molecule.

Referring to the $\text{Pt}/\text{Al}_2\text{O}_3$ -catalyst the spectra of adsorbed **14** and **20** are more structured than the spectrum of adsorbed **21** which interacts with the catalyst only via the nitrogen atom. The spectrum of **14** adsorbed on Pt/SiO_2 indicates that a different adsorption mode takes place. This is presumably an effect of the separation of the proton of the hydroxyl group by abstraction by the catalyst which does not take place on Pt/SiO_2 -catalyst. The spectra of the used catalyst show that the adsorbed species are partially hydrogenated but still present on the surface of the catalyst.

5.3 Interaction of the chiral modifier **22** with the catalyst surface

For the utilisation of **22**-type phosphoric acids as chiral modifier in heterogeneously catalysed reactions the interactions between the solid catalyst and such acids have to be considered.

Figure 40 shows UV-vis-DRS spectra of pure **22** and **22** adsorbed on $\text{Pt}/\text{Al}_2\text{O}_3$ and on Al_2O_3 . For comparison the spectrum of the 1:1-mixture of **22** and KOH is included. The spectrum of pure **22** is characterised by one broad band with maximum at 303 nm. The spectrum of **22** adsorbed on $\text{Pt}/\text{Al}_2\text{O}_3$ (cf. Figure 40d) shows a maximum at 303 nm, too. In addition, to this band a second band appears at 368 nm. The spectrum of **22** adsorbed on pure Al_2O_3 was taken as well in order to elucidate if the adsorption takes place on the pure acidic support. The spectrum (cf. Figure 40c) shows bands at 303 nm and 368 nm. Referring to the spectrum of the 1:1-mixture of **22** with KOH (cf. Figure 40b) the band at 368 nm is prominent for the anion of dissociated **22**. This implicates a reaction of **22** with the catalyst. Obviously **22** dissociates by adsorption. Because this band was observed in the spectra of both solids,

Pt/Al₂O₃ and Al₂O₃, it can be concluded that the support is responsible for the dissociation of **22**.

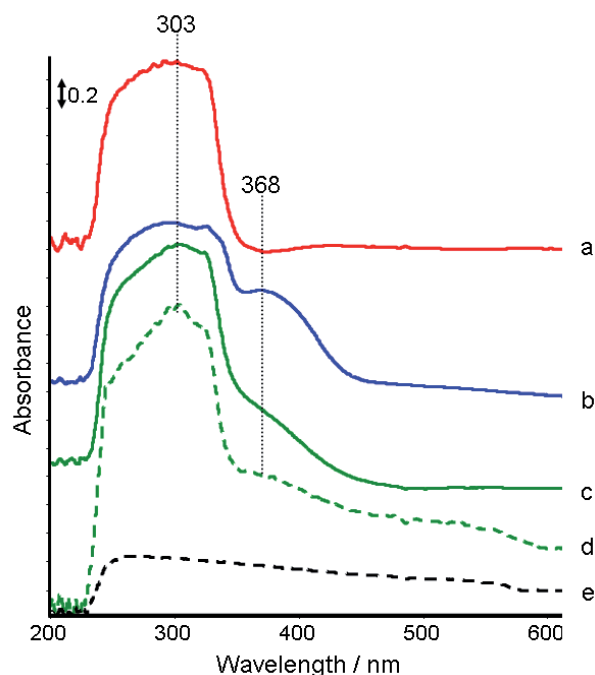


Figure 40. UV-vis-DRS spectra: (a) pure **22** as solid, (b) 1:1-mixture of **22** and KOH as solid, (c) **22** adsorbed on Al₂O₃, (d) **22** adsorbed on Pt/Al₂O₃, (e) pure Pt/Al₂O₃.

is involved in the adsorption process.

The adsorption of **22** on Pt/SiO₂ has been investigated as well. But neither with UV-vis-DRS nor with FTIR-transmission spectroscopy adsorbates of **22** could be detected on the catalyst surface (cf. Figure 41c). A reason for this might be that the neutral support SiO₂ does not stabilise charged species which occur after dissociation of **22** on Al₂O₃. This shows that the support has essential influence on the adsorption of **22**.

Finally, the adsorption of a 1:1 mixture of **14** and **22**, imine and chiral modifier, on Pt/Al₂O₃ was tested. Imine **14** was chosen for this study because it adsorbs in significant amount on the catalyst surface and the spectrum of adsorbed **14** shows several bands of distinct shape which are already assigned. The interaction between the two compounds in CH₂Cl₂ has been studied before with ATR-FTIR spectroscopy. Characteristic bands and pattern of the anion of **22** could be observed like the protonation of **14** (cf. Appendix p. H). Under these conditions both tautomers of **14** – the protonated imine-form and protonated quinoid-form – are present [106].

The FTIR-transmission spectrum of **14** and **22** co-adsorbed on Pt/Al₂O₃ shows clearly the characteristic bands of adsorbed **22** (cf. Figure 41a and 41d). Characteristic bands for the presence of **14** can be observed at 1635 cm⁻¹ (partly overlaid by a strong band of **22** at 1620

This surprising behaviour was also proved by FTIR-transmission spectroscopy. Figure 41a shows the FTIR-transmission spectrum measured from a self-supporting wafer of **22** adsorbed on Pt/Al₂O₃. The spectrum shows bands at 1238, 1216, 1208, 1104, and 1073 cm⁻¹. The band positions are similar to the positions which were observed for the solid 1:1-mixture of **22** and KOH and the 1:1-mixture of **22** and **20** in liquid phase (cf. Figure 31). This confirms the conclusion made from the UV-vis-DRS spectra. The adsorption behaviour of **22** on pure Al₂O₃ is the same as on Pt/Al₂O₃ (cf. Figure 41b) which shows that mainly the catalyst support

cm^{-1}) and at 1538 cm^{-1} . Both bands appear with rather weak intensity in the spectra. Hence, the ion pair formed in solution between **14** and **22** (cf. Appendix p. H) is mostly separated when it comes in the vicinity of the catalyst surface. The favoured species for adsorption is **22**. The same behaviour could be detected on pure Al_2O_3 (cf. Figure 41b and 41e), too. This shows very clearly that the support is responsible for the strong adsorption of **22**. These findings could also be validated by UV-vis-DRS spectroscopy (spectrum not shown). $\text{Pt}/\text{Al}_2\text{O}_3$ shows after co-adsorption of **14** and **22** two bands at 303 and 368 nm which are prominent for dissociated **22**. Bands characteristic for **14** could not be detected. This demonstrates that from an 1:1-mixture of **14** and **22** mainly **22** adsorbs on $\text{Pt}/\text{Al}_2\text{O}_3$.

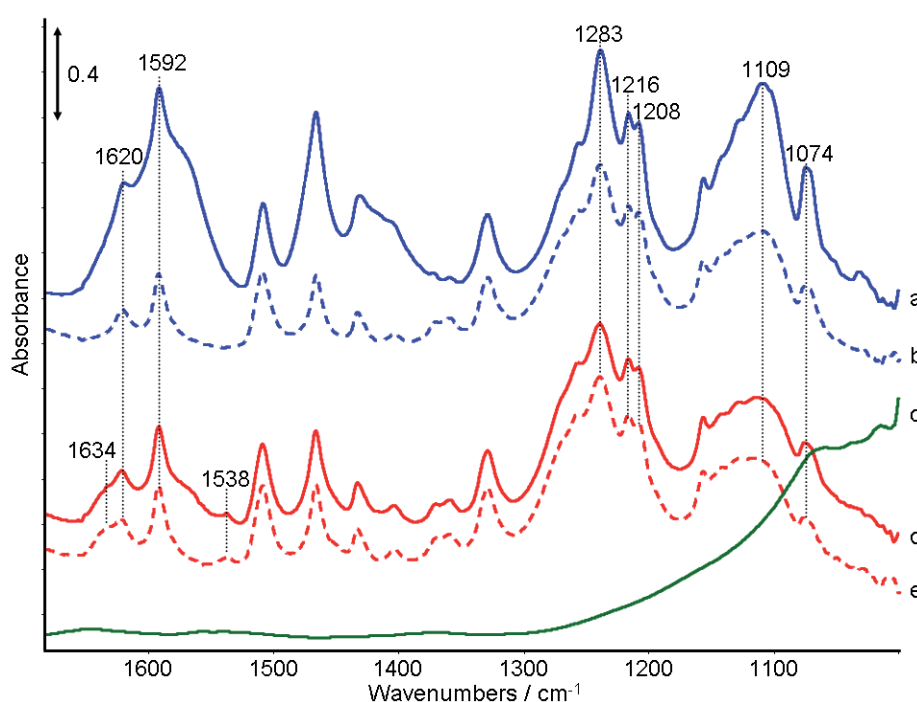


Figure 41. Difference FTIR-transmission spectra (measured from self-supporting wafer) of: **22** adsorbed on (a) $\text{Pt}/\text{Al}_2\text{O}_3$ (spectrum of pure $\text{Pt}/\text{Al}_2\text{O}_3$ subtracted), (b) on Al_2O_3 (spectrum of pure Al_2O_3 subtracted), (c) Pt/SiO_2 (spectrum of pure Pt/SiO_2 subtracted); **14** and **22** co-adsorbed on (d) $\text{Pt}/\text{Al}_2\text{O}_3$ (spectrum of pure $\text{Pt}/\text{Al}_2\text{O}_3$ subtracted) and (e) on Al_2O_3 (spectrum of pure Al_2O_3 subtracted).

5.4 Elucidation of the adsorption sites

There is still the question remaining at which site of the catalyst the adsorption of the imines and of the chiral modifier occurs: on the support, on the metal or on both. It was shown that **14**, **20**, **21** and **22** adsorb on $\text{Pt}/\text{Al}_2\text{O}_3$ but also on pure Al_2O_3 . Thus, the question arises to which extent the metal surface is involved in the adsorption. The adsorption of CO provides information concerning the “free” platinum sites. Comparing the FTIR-transmission spectra of adsorbed CO on a pure platinum catalyst with the spectra of adsorbed CO on loaded catalysts the available sites for the platinum carbonyl formation can be determined. In this

way the extend of platinum sites involved in the adsorption of imines and of the chiral modifier can be estimated. The results of the CO-adsorption are shown in Figures 42 and 43.

The spectrum of CO adsorbed on Pt/Al₂O₃ shows a splitted band with maxima at 2077 cm⁻¹ and 2054 cm⁻¹ (cf. Figure 42). This band position is characteristic for Pt⁰-sites. The appearance of two maxima results from adsorption on different sites. Contrary to this, the spectra of the catalysts with pre-adsorbed species show only one band for adsorbed CO: at 2056 cm⁻¹ for **14**, 2061 cm⁻¹ for **21** and at 2060 cm⁻¹ for **22**. This evidences that one site of the particles – the site at 2055 cm⁻¹ – is occupied by **14**, **21**, and **22**. The intensity of the CO band is similar in the spectra of pure Pt/Al₂O₃ and Pt/Al₂O₃ loaded with **14** or **21**. But in the spectrum of Pt/Al₂O₃ loaded with **22** a lower band intensity is observed indicating that also the second platinum site is partly occupied by adsorbed **22**.

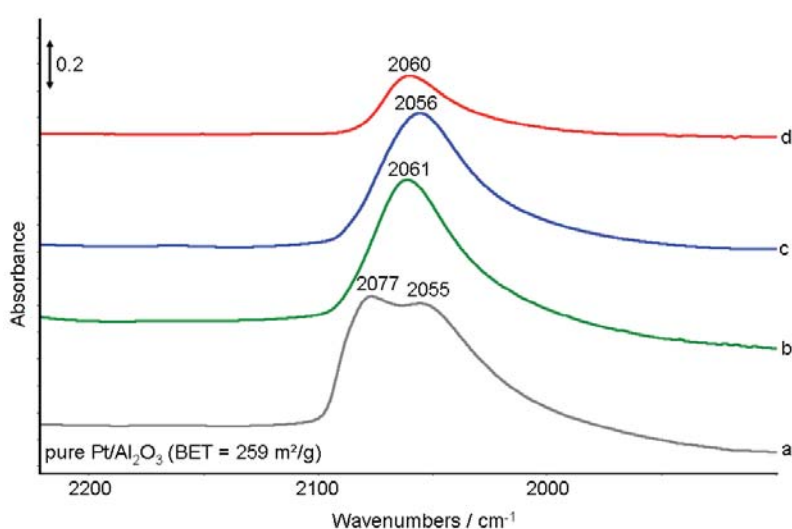


Figure 42: Spectra of adsorbed CO on Pt/Al₂O₃: (a) pure catalyst, (b) pre-adsorbed **21**, (c) pre-adsorbed **14** and (d) pre-adsorbed **22**.

The spectrum of CO adsorbed on Pt/SiO₂ shows two bands at 2089 cm⁻¹ and 2061 cm⁻¹ (cf. Figure 43). The band shape of the CO-bands adsorbed on the Pt/SiO₂ catalysts loaded with **14** and with **21** is similar to those in the experiments with Pt/Al₂O₃. The bands occur at 2083 and 2056 cm⁻¹ in the spectrum of Pt/SiO₂ loaded with **21** and at 2080 and 2070 cm⁻¹ in the spectrum of Pt/SiO₂ loaded with **14**, respectively. Contrary to the pure catalyst in which the band at higher wavenumbers is more intense, the band at lower wave numbers is most intense when the imine was pre-adsorbed. Hence, it seems that the site at 2089 cm⁻¹ is mostly occupied by adsorbates in these experiments while the site at 2061 cm⁻¹ is less occupied. The spectrum of CO adsorbed on Pt/SiO₂ loaded with **22** shows two bands at 2117 cm⁻¹ and at 2079 cm⁻¹. Referring to the band position and intensity, **22** adsorbs mainly at the

site which occurs at 2089 cm^{-1} in the spectrum of the pure catalyst. The band of weak intensity at 2117 cm^{-1} indicates the appearance of a Pt^+ species.

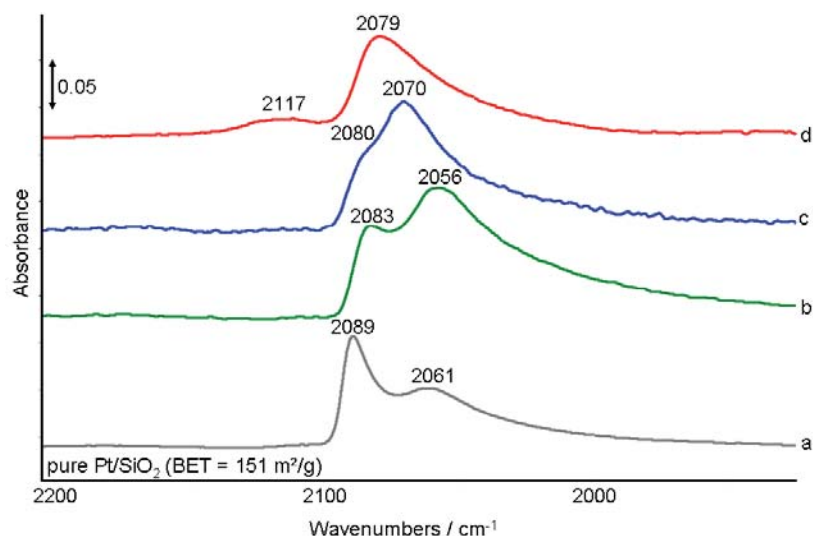


Figure 43: Spectra of adsorbed CO on Pt/SiO₂: (a) pure catalyst, (b) pre-adsorbed **21**, (c) pre-adsorbed **14** and (d) pre-adsorbed **22**.

Interestingly, the band intensities of the Pt/SiO₂ sample are much lower as for the Pt/Al₂O₃ sample. This is caused by the different BET surface areas. Pt/SiO₂ catalyst has BET surface area of $159\text{ m}^2/\text{g}$ and Pt/Al₂O₃ one of $259\text{ m}^2/\text{g}$. On the other hand the metal particle size and distribution has a big influence, too. The TEM-picture (cf. Figure 44) of the Pt/Al₂O₃ catalyst shows a homogeneous particle distribution with an average particle size of 5-10 nm. In contrast the TEM-picture of the Pt/SiO₂ (cf. Figure 44) catalyst shows very small particles of less than 5 nm but also huge agglomerates of more than 100 nm.

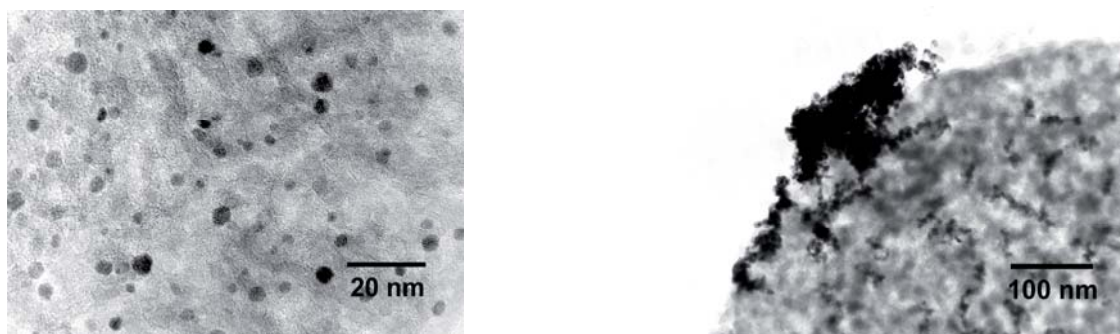


Figure 44. TEM pictures of the catalysts: 5 wt% Pt/Al₂O₃ (left) and wt% Pt/SiO₂ (right).

5.5 In situ studies: Testing the reaction unit

The comprehensive ex situ characterisation of the reactants including the interactions between themselves was necessary to get reference data for the in situ measurements. The ex situ investigations showed already certain limitations for the in situ analysis. Raman spectroscopy

is difficult to use because of the strong fluorescence introduced by the model acid **22** (cf. Appendix p. J). The solid catalyst cannot be observed directly via UV-vis-DRS spectroscopy because the concentration of the catalyst is too low in the liquid phase. The application of UV-vis-transmission spectroscopy is also difficult due to of the relatively high concentration levels (cf. Appendix p. K). The starting concentration of imine has to be chosen $0.2 \text{ mol}\cdot\text{L}^{-1}$ or even higher in order to provide adequate analysis conditions for the application of ATR-FTIR and Raman spectroscopy. For this reason only broad bands of the imine and the corresponding product appear in the in situ measured UV-vis spectra. The broad bands perturb in situ investigations of interactions between **21** and **22** which should be performed at a lower concentration level in order to get more detailed UV-vis spectra. Finally, strong solvent bands limit the study of the interaction of **21** with **22** by using ATR-FTIR spectroscopy.

Instead of a comprehensive in situ analysis of the complete process, some selected in situ studies will be presented in this chapter to show the applicability of the reaction unit despite the previous mentioned spectroscopic limitations.

Figure 45 shows the in situ measured ATR-FTIR and Figure 46 the respective Raman spectra of the hydrogenation of **21** (cf. Scheme 20). The reaction mixture contains **21** dissolved in CH_2Cl_2 ($c = 0.2 \text{ mol}\cdot\text{L}^{-1}$) and 32 mg $\text{Pt}/\text{Al}_2\text{O}_3$ as catalyst. After dosing of molecular hydrogen with a pressure of 20 bar and start of stirring the reaction progress can be monitored. Suitable bands for reaction monitoring of the imine conversion can be detected by ATR-FTIR spectroscopy at 1639, 1593, 1483, and 1213 cm^{-1} (cf. Figure 45). The respective Raman bands appear at 1639, 1595, 1288, and 1213 cm^{-1} (cf. Figure 46).

Generally, the band at 1639 cm^{-1} which is prominent for the $\nu(\text{C}=\text{N})$ vibration is the most suitable band for monitoring conversion because this band is not overlaid by any other bands from the solvent or the product **23**. Characteristic bands indicating the formation of the product can be observed at 1601 and 1504 cm^{-1} . Interestingly, these bands occur only in the ATR-FTIR spectra.

The Raman spectrum of the corresponding product provides only one weak band at 1603 cm^{-1} and a band at 993 cm^{-1} which is overlaid with a substrate band at 1000 cm^{-1} . For this reason Raman spectroscopy is rather suitable for monitoring the conversion while ATR-FTIR spectroscopy enables the simultaneous monitoring of conversion and product formation. The product is characterised by a band at 1504 cm^{-1} which can be assigned to the $\delta(\text{NH})$ vibration. This band was chosen to monitor the product formation.

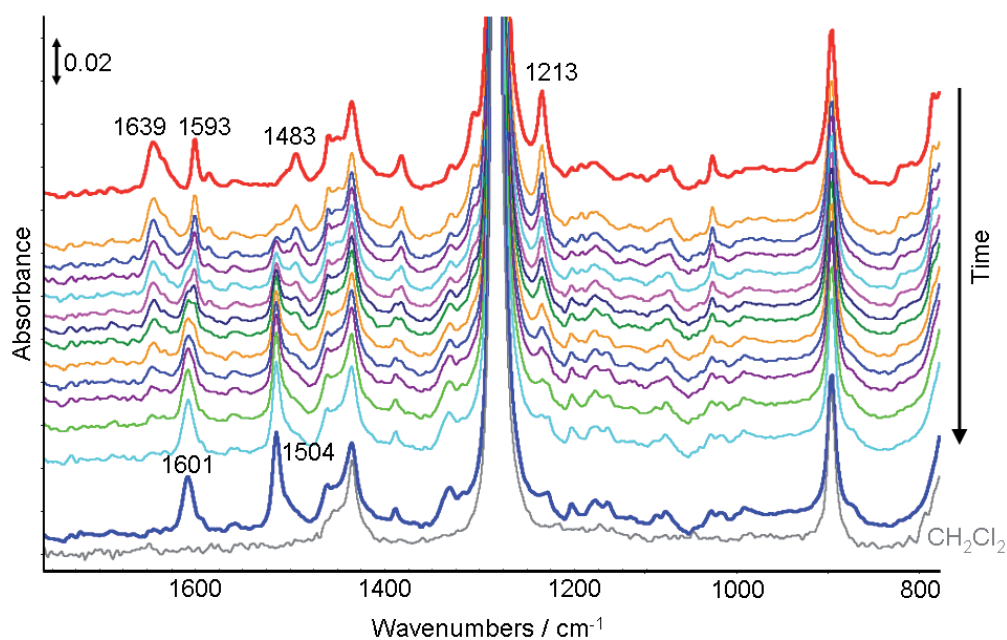


Figure 45: Hydrogenation reaction of **21** to **23** monitored by ATR-FTIR spectroscopy; $c_{\text{start}} = 0.2 \text{ mol}\cdot\text{L}^{-1}$, $V(\text{CH}_2\text{Cl}_2) = 40 \text{ mL}$, $m(\text{Pt}/\text{Al}_2\text{O}_3) = 32 \text{ mg}$.

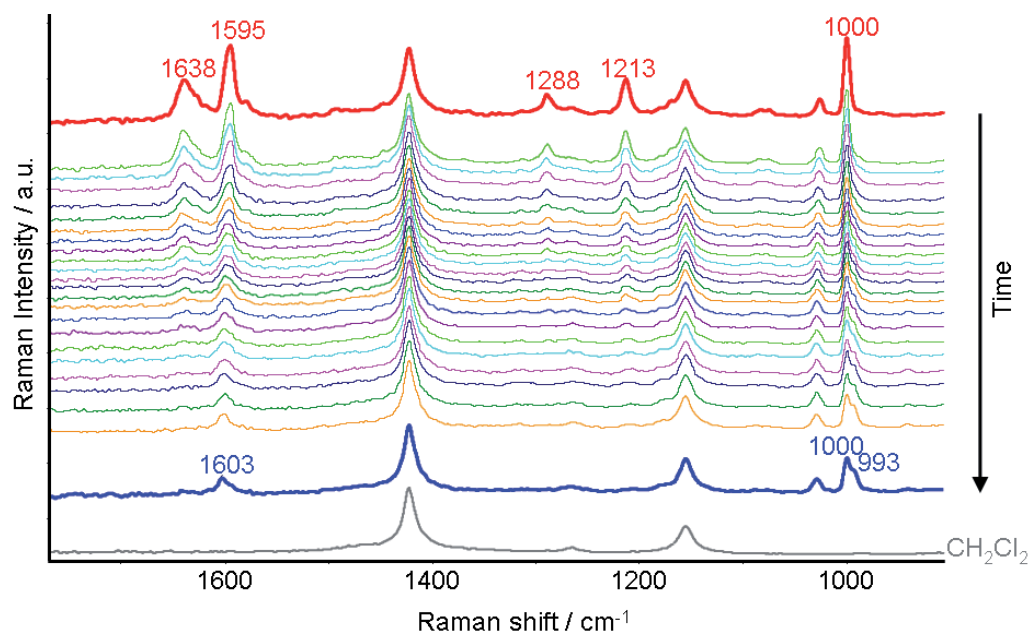
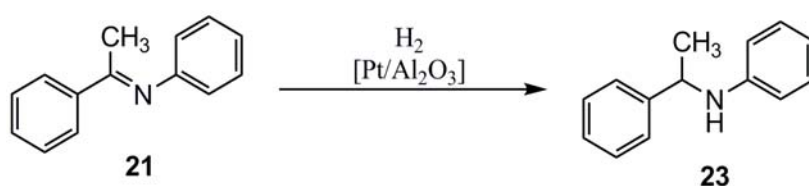


Figure 46: Hydrogenation reaction of **21** to **23** monitored by Raman spectroscopy; $c_{\text{start}} = 0.2 \text{ mol}\cdot\text{L}^{-1}$, $V(\text{CH}_2\text{Cl}_2) = 40 \text{ mL}$, $m(\text{Pt}/\text{Al}_2\text{O}_3) = 32 \text{ mg}$.



Scheme 20. Reaction scheme for Figures 45 and 46.

An important result of the in situ experiments is that the Lewis acid catalyst Pt/Al₂O₃ converts **21** under the applied conditions to the corresponding reaction product with high selectivity. This has been proven by taking NMR spectra of the reaction mixture at the end of the reaction.

In order to obtain adequate results from the in situ experiments a screening of reaction conditions was made. The reaction should not proceed so fast that not enough spectra for suitable analysis can be taken but also not too slow, so that the analysis takes more time than necessary. First in situ investigations showed that the reaction time of the imine hydrogenation is relatively short already at room temperature [40]. Heating of the reaction mixture leads to a drastic increase of the reaction rate. A test at 60°C showed that the reaction was finished in less than 10 minutes. Considering that the ATR-FTIR spectroscopic measurement has an acquisition time of 2 minutes, the best possible time resolution is 5 minutes, which is too slow when the reaction is performed at 60°C. On the other hand, for the production of an Arrhenius plot, measurements at least at 5 different temperatures are required. Typically, the interval between the temperatures should be 10 K. Adequate cooling of the reaction unit to certain reaction temperatures is difficult because a temperature of 60°C is required.

Another important factor is the amount of catalyst which is applied in the reaction. If too much catalyst is used, mass transfer limitation can occur because a lower amount of reactants – especially hydrogen – as required could be present at the active site of the catalyst. On the other hand, if the amount of catalyst is too small, the error of balancing can be too high and the experiments are not comparable.

The previous experiments show that the band of the $\nu(\text{C}=\text{N})$ vibration has strong intensity in the Raman spectra, while the acquisition time for recording spectra is shorter than in ATR-FTIR spectroscopy. For these reasons Raman spectroscopy was chosen for monitoring the conversion using the band of the $\nu(\text{C}=\text{N})$ vibration.

Figure 47 shows the results of some screening experiments in which the catalyst amount was varied. The conversion of **21** to **23** can be estimated by the changes of the integral band intensity of the $\nu(\text{C}=\text{N})$ vibration in the Raman spectra. The reaction rate obviously depends on the amount of catalyst in the reaction mixture. The reaction rate increases with the amount of catalyst. 50% conversion can be observed after 9 and 19 min when 64 and 32 mg catalyst were applied.

Additionally, the solvent, the catalyst support and the substrate have been varied. Figure 48 shows the conversion of **21** to **23** in $\text{CF}_3\text{CH}_2\text{OH}$ (cf. Figure 48a) and in CH_2Cl_2 (cf. Figure 48b) with 32 mg $\text{Pt}/\text{Al}_2\text{O}_3$.

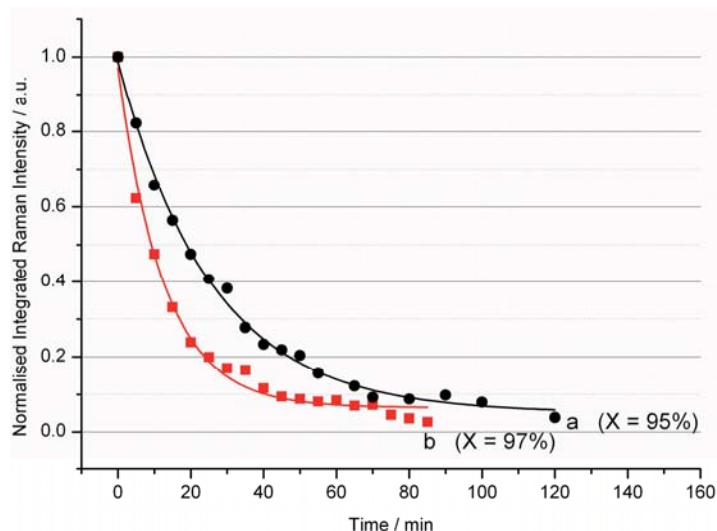


Figure 47. Variation of catalyst amount: $m(\text{Pt}/\text{Al}_2\text{O}_3) =$ (a) 32 and (b) 64 mg, reaction progress of the hydrogenation of **21** to **23** monitored by Raman spectroscopy; $c(\mathbf{21})_{\text{start}} = 0.2 \text{ mol}\cdot\text{L}^{-1}$, $V(\text{CH}_2\text{Cl}_2) = 40 \text{ mL}$; the conversion is calculated from ^1H NMR spectra taken from the reaction mixture after reaction was finished (error $\sim 3\text{-}5\%$).

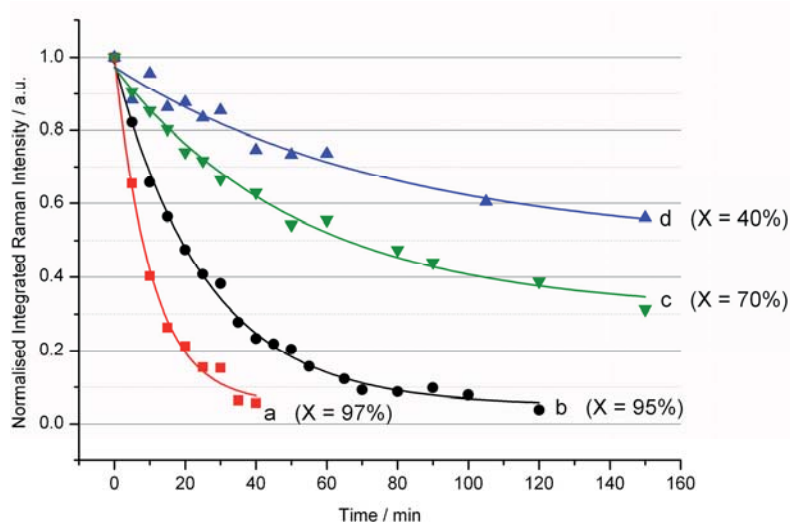
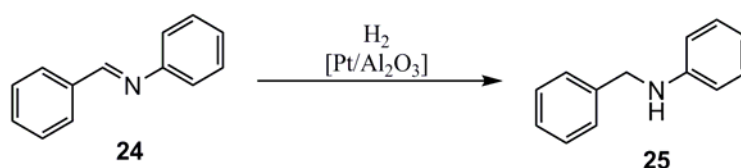


Figure 48. Variation of solvent, catalyst and substrate: $m(\text{Pt}/\text{Al}_2\text{O}_3) = 32 \text{ mg}$ in (a) $\text{CF}_3\text{CH}_2\text{OH}$ or (b) CH_2Cl_2 , (c) of the hydrogenation of **24** to **25** with $m(\text{Pt}/\text{Al}_2\text{O}_3) = 32 \text{ mg}$ in CH_2Cl_2 , (d) $m(\text{Pt}/\text{SiO}_2) = 55 \text{ mg}$ in CH_2Cl_2 ; reaction progress of the hydrogenation of **21** to **23** monitored by Raman spectroscopy; $c(\mathbf{21}, \mathbf{24})_{\text{start}} = 0.2 \text{ mol}\cdot\text{L}^{-1}$, $V(\text{solvent}) = 40 \text{ mL}$; the conversion is calculated from ^1H NMR spectra taken from the reaction mixture after reaction (error $\sim 3\text{-}5\%$).



Scheme 21. Reaction scheme of the hydrogenation of the aldimine N-benzylideneaniline **24**.

Comparing the reaction in CH_2Cl_2 and $\text{CF}_3\text{CH}_2\text{OH}$ the reaction rate is higher when the experiment is carried out in $\text{CF}_3\text{CH}_2\text{OH}$ under the same reaction conditions (cf. Figure 48b). The increased reaction rate could be explained by: i) the formation of hydrogen bonds from the solvent to solute (cf. Figure 30 and 32) and activating the substrate and ii) the greater solubility of hydrogen in $\text{CF}_3\text{CH}_2\text{OH}$ compared to CH_2Cl_2 . In general, the in situ measured spectra gave no hints on side products or intermediates.

In order to estimate the different reaction rate in the hydrogenation of ketimines and aldimines N-benzylideneaniline **24** (cf. Scheme 21) as non-prochiral aldimine was

incorporated in the study. Aldimine **24** has nearly the same structure as **21** without the methyl group at the α -carbon atom of the imine group.

The electronic and steric influences from the phenyl groups should be in both molecules the same which restricts all differences in reaction rate to the presence of the methyl group or the hydrogen atom at the α -carbon atom. The temporal changes of Raman band intensity during hydrogenation of **24** are shown in Figure 48c. The obtained curve indicates that the reaction rate of the hydrogenation of **24** is much slower compared to the rate of **21** measured under the same conditions. This shows that steric reasons seem to be less important as limiting factor for the reaction rate because **21** is sterically more hindered than **24** due to the methyl group. Obviously, the electronic structure should be the reason for the different reaction rates. But it is rather difficult to distinguish if the electronic structure of **21** favours the adsorption / desorption behaviour on the catalyst surface or the attack of hydrogen on the C=N double bond.

The support of the catalyst has been varied as well. It is known that the catalyst support may have important influence on the properties of the catalyst. Two catalysts with different acidity of the support were chosen for the experiments: 5 wt% Pt/Al₂O₃ and 5 wt% Pt/SiO₂. The Pt/SiO₂-catalysed experiment revealed a different reaction pathway. Here, the monitoring of reaction progress indicates a lower reaction rate (cf. Figure 48d). This was rather surprising because both catalysts are loaded with 5 wt% of platinum. The difference in surface area (BET: 269 m²/g for Pt/Al₂O₃ and 151 m²/g for Pt/SiO₂) has been considered by using a greater amount of catalyst (55 mg Pt/SiO₂ have been used for the experiment). As known from the TEM pictures (cf. Figure 44) the Pt/Al₂O₃ catalyst has a homogeneous distribution of particles which have a size of 5-10 nm, while the Pt/SiO₂ catalyst has very small particles of less than 5 nm but also huge agglomerates of more than 100 nm. Furthermore, it seems that the major amount of platinum on the surface of the Pt/SiO₂ catalyst is catalytic inactive because it is agglomerated. It is well known that the size of the metal particles on the catalyst surface has great impact on the reaction rate. Hence, both catalysts are not comparable to each other because of the different size of the metal particles. This inhibits an elucidation of the influence of the catalyst support on the reaction rates. Due to these results no more reaction monitoring experiments have been performed with the Pt/SiO₂ catalyst. Although the reaction rate was decreased dramatically when Pt/SiO₂ was applied the product selectivity was still good. No side-product could be detected after reaction in the reaction mixture.

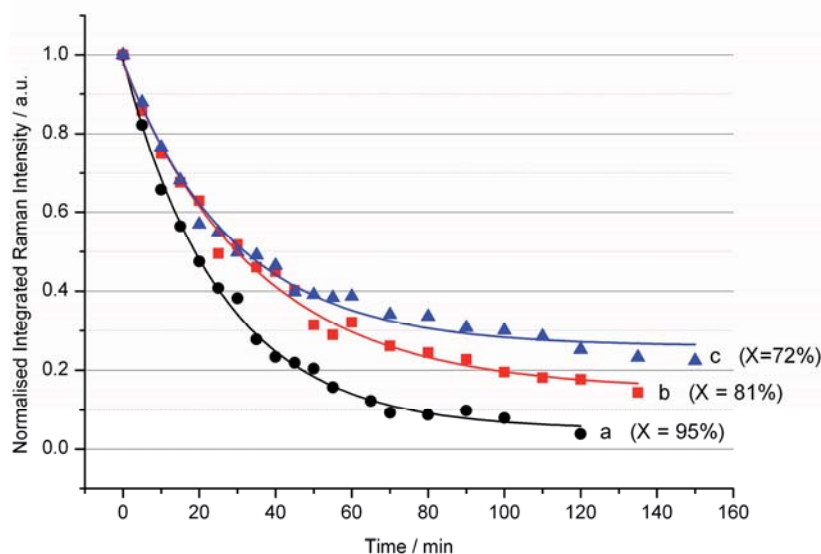


Figure 49. Reaction rates of (a) 32 mg pure Pt/Al₂O₃, (b) 36 mg Pt/Al₂O₃ with pre-adsorbed **21** and (c) 36 mg Pt/Al₂O₃ with pre-adsorbed **22** examined by the temporal changes of the $\nu(\text{C}=\text{N})$ band intensity in the Raman spectra of **21**; $c(\mathbf{21})_{\text{start}} = 0.2 \text{ mol/L}$, $V(\text{CH}_2\text{Cl}_2) = 40 \text{ mL}$; the conversion is calculated from ¹H NMR spectra taken from the reaction mixture after reaction was finished (error ~3-5%).

of Pt/Al₂O₃ with pre-adsorbed **21** or **22** have been used. As already mentioned the temporal changes of the Raman band intensity of the $\nu(\text{C}=\text{N})$ vibration was analysed which reflects the imine conversion. The obtained curves indicate that the adsorbates lower the rate of conversion (cf. Figure 49b and 49c). Pre-adsorbed **22** affects the reaction rate stronger than pre-adsorbed **21**. It seems that both types of adsorbates poison the catalyst. This is in line with the results of the CO-adsorption: adsorbed **21** blocks at least one of the two sites of the platinum particles while **22** blocks one site completely and the second site partially.

5.6 Conclusion 3

The ex situ experiments showed that the interaction between the model substrate **21** and the model acid **22** are strongly influenced by the used solvent. A contact ion pair between protonated imine and acid anion of **22** occurs only in solvents with a low value for HBA β like CH₂Cl₂ or CF₃CH₂OH. When the distance between protonated imine and acid anion of **22** becomes too large as an effect of solvation, the stabilisation of the positive charge proceeds via the formation of a carbocation as observed in CH₃OH. Both effects are detrimental for the achievement of enantiomeric excess. Taking the spectroscopic findings into account that the initial step of the reaction is the interaction between substrate and chiral modifier leading to a protonation of the imine, these findings can be also transferred to the mechanism of the organocatalytic transfer hydrogenation reaction of **21** to **23** published by Hoffmann et al. [138] and Rueping et al. [138]. The parallel existence of ion pairing and hydrogen bonding in the same sample as concluded by Fleischmann et al. [161] from NMR spectroscopic results

For elucidating the effect of pre-adsorbed imines or chiral modifier on the reaction rate the hydrogenation reaction was investigated with pre-adsorbed **21** and **22** using Pt/Al₂O₃ as catalyst. The amount of adsorbed species was determined with TGA and is about 10 wt%. For the comparison of reaction rates (cf. Figure 49) 32 mg of pure Pt/Al₂O₃ and 36 mg

could not be observed in the experiments carried out with ATR-FTIR, UV-vis, and Raman spectroscopy.

The Lewis acid support of the Pt/Al₂O₃ catalyst interacts strongly with imines as well as with the model acid. Respective adsorbates of **14**, **20**, **21** and **22** were observed by FTIR-transmission and UV-vis-DRS spectroscopy. Surprisingly, **22** adsorbs as anion on the solid catalyst and is deactivated completely for the catalytic cycle. Hence, an immobilisation on Lewis acid supports is possible but implicates deactivation of the chiral modifier. The imines **14** and **20** adsorb via both – the oxygen and the nitrogen – atoms on the support. During imine adsorption on Al₂O₃ the proton is separated from the hydroxyl group by bonding to the oxygen anions of the support. The adsorption of **21** takes place via the nitrogen atom only. Such detailed spectra like for **14**, **20** or **22** could not be obtained for adsorbed **21**. As proved by CO adsorption, **14**, **21**, and **22** adsorb not only on the support. The platinum surface is partly involved in the adsorption process as well.

On Pt/SiO₂ the imines **14** and **21** adsorb in a different manner. This might be caused by the lower acidity of the support. Also **22** seems to adsorb only with a low amount on the support. However, the different adsorption mode on SiO₂ compared to Al₂O₃ might be caused by missing separation of the proton from the hydroxyl group during adsorption of **14** or **22**. The investigations with CO adsorption show that a part of the metal surface is involved in the adsorption of **14**, **21**, and **22** on the catalyst. This is confirmed by the in situ experiments which showed that pre-adsorbed **21** and **22** have deactivating effect on the catalyst performance.

Because of the low concentration of catalyst and adsorbates it was not possible to detect the adsorbates on the surface of the catalyst by in situ UV-vis-DRS spectroscopy. However, it could be demonstrated that the set-up is adequate for monitoring this hydrogenation reaction using ATR-FTIR and Raman spectroscopy. The experiments showed that the reaction proceeds fast at room temperature and can be accelerated by increasing temperature, increasing amount of catalyst or by changing the solvent. Because of the different morphology of the platinum particles on Pt/Al₂O₃ and Pt/SiO₂ a direct comparison of the reaction rates is difficult. Insofar, the influence of support on the reaction rate could not be properly elucidated.

For future experiments it should be taken into account that Lewis acid catalysts like Pt/Al₂O₃ lead to adsorption and deactivation of imines and chiral modifiers like **22**. For the optimisation of the hydrogenation reaction, catalysts with neutral support like Pt/C or Pt/SiO₂ would be more favourable. However, in this study the Lewis acid Pt/Al₂O₃ catalyst enabled a

proper analysis of the adsorbates. Even at 100°C at $5 \cdot 10^{-4}$ mbar these adsorbates are stable which was proved by FTIR-transmission spectroscopy. The application of substrates with a second active site as **20** would facilitate the development of an enantioselective heterogeneous catalyst for this reaction. It was shown already that the applied substrates attack cinchonidine-modified Pt/Al₂O₃ with two sites which provokes a sterically favoured adsorption mode and lead finally to enantiomeric excess in the obtained product [130, 143]. From the analytical point of view the coating of ATR-FTIR and UV-vis-DRS probes with the catalyst would enable the direct study of adsorbates under reaction conditions [37, 164]. Finally, the application of nanoparticles as catalysts would open the possibility to study the electronic structure in form of surface-plasmon resonance of the working catalyst under reaction conditions by UV-vis spectroscopy.



6. General conclusion and outlook

The results of both application examples demonstrate the advantages of using coupled in situ optical spectroscopy for the elucidation of reaction mechanisms. In particular the probe-technique offers new possibilities because it enables measurements in sophisticated reactors. Besides the presented application examples both reaction setups have been already used successfully in other projects [165, 166]. This shows the versatile applicability of the developed systems for the in situ analysis of reactions. The realised investigations showed that the reactant conversion as well as the product formation can be observed nicely by ATR-FTIR and Raman spectroscopy. In both application examples ATR-FTIR spectroscopy showed more detailed spectra in the fingerprint region between 1800 and 800 cm^{-1} . Metal-non-metal vibrations appearing in the low-frequency area and can be properly observed by Raman spectroscopy if no fluorescence occurs. While these methods give information about the structural states of molecules, the additional application of UV-vis spectroscopy provides information in terms of the electronic state, for example, delocalised electrons or charge transfer transitions. Both applied setups allow the analysis of clear solutions as well as suspensions. However, some limitations of the different spectroscopies have to be considered. Thus, the analysis of concentrated solutions by UV-vis-transmission spectroscopy is difficult because the bands are blurred to one broad band. Nevertheless, also such bands can be facilitated for the supplemental characterisation of samples. Dilution series are often useful for a deeper interpretation of the UV-vis spectra. Otherwise, comparable higher concentrations of reactants and products in solution are required to enable the appropriate analysis by in situ ATR-FTIR and Raman spectroscopy. Insofar a compromise has to be made in many cases to enable the reaction monitoring under realistic conditions using different spectroscopic methods in one setup.

The experiments showed that the analysis of clear solutions is rather easy when no fluorescence occurs which may perturb Raman spectroscopic measurements. But the appearance of particles in the reaction mixture can disturb the measurements using Raman or UV-vis-transmission spectroscopy. In this case a UV-vis-DRS probe can be applied in both setups for the monitoring of solid compounds. However, if the concentration of particles in the solution is too low, no bands in the UV-vis spectra can be detected because no sufficient reflection medium is available.

The extent of perturbation of Raman spectroscopic measurements in slurries depends on the scattering properties of the particles. Contrary to UV-vis spectroscopy there are no

technical solutions to overcome these problems. Although an analysis of the gas phase was not intended the observation of dissolved gases in the liquid phase is possible. Thus, heteronuclear diatomic molecules like CO, CO₂, SO₂ or NH₃ can be detected properly by ATR-FTIR spectroscopy in liquid phase.

The analysis of the catalyst under working is desirable to understand its mode of action in the respective reaction. However, the analysis of the working catalyst is difficult because the catalyst concentration in liquid systems is often very low which causes problems in terms of detection limits of the different spectroscopies. In this case UV-vis spectroscopy is the most promising method since it is a more sensitive method than ATR-FTIR or Raman spectroscopy.

Taking all the described advantages and limitations of the different spectroscopic methods into account, the successful application of all these methods depends strongly on the nature of the reactants. Therefore, the coupling of ATR-FTIR, Raman and UV-vis spectroscopy is not applicable for all problems. The selection of the optimal method combination has to be evaluated by test measurements in each case.

Interesting future applications would be the coating of ATR-FTIR and UV-vis-DRS probes with thin layers of solid catalysts to analyse the working catalyst under reaction conditions. The application of theoretical methods for the identification and assignment of the observed bands in the spectra was not part of the thesis. However, a validation of the assignments by calculations would be desirable. On the other hand the calculation of spectra is often performed without consideration of intermolecular interactions referring to solute-solvent and solute-solute interactions. Thus, the deviation between calculated spectra and spectra measured under reaction conditions is often too large for making proper assignments. The decrease of the error in the calculations leads to increased calculation times. Hence, the application of theoretical methods is promising but still challenging [167].

Another field of application of computer-based methods would be the use of chemometrics [168]. This technique enables analysis of single species occurring in multi-component systems like reaction mixtures. Interesting examples for the application of chemometrics in connection with spectroscopy are indirect hard modelling [169], PCD (pure component decomposition) [170] and BTEM (Band-target entropy minimisation) [171]. A chemometric analysis of a multi-component system under reaction conditions would provide deep insights into the investigated process. However, the necessary expenditure time has to be considered.

The measurement of true kinetics was not the objective in both investigated reaction examples because this work was focussed on the elucidation of the reaction mechanism. The [3+3] cyclocondensation reaction is a non-isothermal process and due to volume contraction by temperature changes the concentrations vary. A kinetic analysis of this process would be a large and complex field of research which was out of the frame of this thesis. The kinetic analysis of the heterogeneously catalysed asymmetric hydrogenation of imines was accompanied by problems of tempering and mass transfer limitation which is determined by the stirring rate. However, the apparent reaction rates determined from temporal changes of band intensities are adequate to make qualitative predictions about the reaction kinetics.



7. Literature

- [1] B. M. Weckhuysen, *In situ spectroscopy of catalysts*, edited by B. M. Weckhuysen, American Scientific Publishers **2004**
- [2] A. Brückner, *Catal. Today*, **2010**, *155*, 155.
- [3] B. M. Weckhuysen, *Chem. Soc. Rev.*, **2010**, *39*, 4557.
- [4] M. Hunger, J. Weitkamp, *Angew. Chem.*, **2001**, *113*, 3040; *Angew. Chem. Int. Ed.*, **2001**, *48*, 3904.
- [5] M. A. Bañares, *Catal. Today*, **2005**, *100*, 71.
- [6] B. M. Weckhuysen (editor) *Chem. Soc. Rev.*, **2010**, *39*, 4541.
- [7] A. Bunesco, S. Reimann, M. Lubbe, A. Spannenberg, P. Langer, *J. Org. Chem.*, **2009**, *74*, 5002.
- [8] M. Lubbe, A. Bunesco, A. Villinger, P. Langer, *Synlett* **2008**, 1862.
- [9] L. R. Knöpke, S. Reimann, A. Spannenberg, P. Langer, A. Brückner, U. Bentrup, *ChemCatChem*, **2011**, *3*, 1459.
- [10] M. Bartoszek, M. Beller, J. Deutsch, M. Klawonn, A. Köckritz, N. Nemati, A. Pews-Davtyan *Tetrahedron*, **2008**, *64*, 1316.
- [11] J. M. Thomas, J.-C. Hernandez-Garrigo, *Angew. Chem.*, **2009**, *121*, 3962; *Angew. Chem. Int. Ed.*, **2009**, *48*, 3904.
- [12] H. M. Heise, L. Küpper, L. N. Butvina, *Sensor. Actuat. B-Chem.*, **1998**, *51*, 84.
- [13] L. Küpper, H.-M. Heise, L. N. Butvina, *J. Mol. Struct.*, **2001**, *563-564*, 173.
- [14] U. Bentrup, L. Küpper, U. Budde, K. Lovis, K. Jähnisch, *Chem. Eng. Technol.*, **2006**, *29*, 1216.
- [15] J. Fahrenfort, *Spectrochim. Acta*, **1961**, *17*, 698.
- [16] R. L. McCreery, *Raman spectroscopy for chemical analysis*, Vol. 157 in Chemical Analysis, John Wiley & Sons, **2000**
- [17] R. Borsdorf, M. Schulz, *Spektroskopische Methoden (IR, UV/VIS) in der organischen Chemie*, 5., bearbeitete Auflage WTB, **1989**, p. 112-114.
- [18] H. Suzuki, *Bull. Chem. Soc. Jp.*, **1960**, *33*, 379.
- [19] M. Hesse, H. Meier, B. Zeeh, *Spektroskopische Methoden in der organischen Chemie*, 4. überarbeitete Auflage, Georg Thieme Verlag, **1991**
- [20] A. Brückner, *Chem. Commun.*, **2005**, 1761.
- [21] U. Bentrup, J. Radnik, U. Armbruster, A. Martin, J. Leiterer, F. Emmerling, A. Brückner, *Top. Catal.*, **2009**, *52*, 1310.
- [22] U. Bentrup, *Chem. Soc. Rev.*, **2010**, *39*, 4718.
- [23] S. J. Tinnemans, J. G. Mesu, K. Kervinen, T. Visser, T. A. Nijhuis, A. M. Beale, D. E. Keller, A. M. J. van der Eerden, B. M. Weckhuysen, *Catal. Today*, **2006**, *113*, 3.
- [24] A. M. Beale, A. M. J. van der Eerden, K. Kervinen, M. A. Newton, B. M. Weckhuysen, *Chem. Commun.*, **2009**, 3015.
- [25] M. G. O'Brian, A. M. Beale, S. D. M. Jaques, B. M. Weckhuysen, *Top. Catal.*, **2009**, *52*, 1400.
- [26] M. G. O'Brian, A. M. Beale, T. Buslaps, V. Honkimaki, B. M. Weckhuysen, *J. Phys. Chem. C*, **2009**, *113*, 4890.
- [27] M. G. O'Brian, A. M. Beale, S. D. M. Jaques, M. Di Michiel, B. M. Weckhuysen, *ChemCatChem*, **2009**, *1*, 99.
- [28] T. A. Nijhuis, S. J. Tinnemans, T. Visser, B. M. Weckhuysen, *Phys. Chem. Chem. Phys.*, **2003**, *5*, 4361.
- [29] T. A. Nijhuis, S. J. Tinnemans, T. Visser, B. M. Weckhuysen, *Chem. Eng. Sci.*, **2004**, *59*, 5487.
- [30] S. J. Tinnemans, M. H. F. Kox, T. A. Nijhuis, T. Visser, B. M. Weckhuysen, *Phys. Chem. Chem. Phys.*, **2005**, *7*, 211.

- [31] J. Engeldinger, M. Richter, U. Bentrup, *Phys. Chem. Chem. Phys.*, **2011**, in press.
- [32] A. Brückner, *Chem. Soc. Rev.*, **2010**, *39*, 4673.
- [33] C. Janke, M. Schneider, U. bentrup, J. Radnik, A. Martin, G. Schloz, A. Brückner, *J. Catal.*, **2011**, *277*, 196.
- [34] G. Mul, G. M. Hamminga, J. A. Moulijn, *Vib. Spectrosc.*, **2004**, *34*, 109.
- [35] A. Pintar, R. Malacea, C. Pinel, G. Fogassy, M. Besson, *Appl. Catal. A – Gen.*, **2004**, *264*, 1.
- [36] K. Kervinen, H. Korpi, J. G. Mesu, F. Soulimani, T. Repo, B. Rieger, M. Leskela, B. M. Weckhuysen, *Eur. J. Inorg. Chem.*, **2005**, 2591.
- [37] T. Bürgi, *J. Catal.*, **2005**, *229*, 55.
- [38] M. Caravati, J.-D. Grunwald, A. Baiker, *Phys. Chem. Chem. Phys.*, **2005**, *7*, 278.
- [39] D. Hollmann, F. Gärtner, R. Ludwig, E. Barsch, H. Junge, M. Blug, S. Hoch, M. Beller, A. Brückner, *Angew. Chem.*, **2011**, *123*, 10429; *Angew. Chem. Int. Ed.*, **2011**, *43*, 10246.
- [40] L. R. Knöpke, N. Nemati, A. Köckritz, A. Brückner, U. Bentrup, *ChemCatChem*, **2010**, *2*, 273.
- [41] C. Kongmark, V. Martis, A. Rubbens, C. Pirovano, A. Löfberg, G. Sankar, E. Bordes-Richard, R.-N. Vannier, W. van Beek, *Chem. Commun.*, **2009**, 4850.
- [42] J. Radnik, U. Bentrup, J. Leiterer, A. Brückner, F. Emmerling, *Chem. Mater.*, **2011**, in press
- [43] S. Quinebèche, C. Navarro, Y. Gnanou, M. Fontanille, *Polymer*, **2009**, *50*, 1351.
- [44] P. M. Tolstoy, B. Koeppe, G. S. Denisov, H.-H. Limbach, *Angew. Chem.*, **2009**, *121*, 5855; *Angew. Chem. Int. Ed.*, **2009**, *48*, 5745.
- [45] G. W. Roberts, *Catalysis in Organic Synthesis* – edited by P. Rylander and H. Greenfield, Academic Press, Inc. **1976**, p. 32 – 35.
- [46] R. Filler, *Fluorine in Bioorganic Chemistry*, edited by Y. Kobayasi, L.M. Yagupolskii, Elsevier, Amsterdam, **1993**
- [47] R. Filler, *Biomedical Aspects of Fluorine Chemistry*, Kodansha Ltd., Tokyo, **1982**, p. 461.
- [48] M. Hudlicky, *Chemistry of organic fluorine compounds, in: A Laboratory Manual with Comprehensive Literature Coverage*, Wiley, New York, **1976**, p. 550.
- [49] R. D. Chambers, *Fluorine in Organic Chemistry*, Blackwell Publishing CRC Press, **2004**, pp. 12 - 24.
- [50] T. Ryckmans, L. Balançon, O. Berton, C. Genicot, Y. Lamberty, B. Lallemand, P. Pasau, N. Pirlot, L. Quéré, P. Talaga, *Bioorg. Med. Chem. Lett.*, **2002**, *12*, 261.
- [51] M. S. Malamas, J. Sredy, C. Moxham, A. Katz, W. Xu, R. McDevitt, F. O. Adebayo, D. R. Sawicki, L. Seestaller, D. Sullivan, J. R. Taylor, *J. Med. Chem.*, **2000**, *43*, 1293.
- [52] A. J. Ciha, P. G. Ruminski, *J. Agr. Food Chem.*, **1991**, *39*, 2072.
- [53] H. Schmidbaur, O. Kumberger, *Chem. Ber.*, **1993**, *126*, 3.
- [54] M. B. Dinger, W. Henderson, *J. Organomet. Chem.*, **1998**, *560*, 233.
- [55] J. Liedtke, S. Loss, C. Widauer, H. Grützmacher, *Tetrahedron*, **2000**, *56*, 143.
- [56] S. Schneider, C. Tzuschicke and B. Bannward, *Multiphase Homogeneous Catalysis*, 1st Edition, edited by B. Cornils, W.A. Herrmann, I.T. Horvath, W. Leitner, S. Mecking, H. Olivier-Booubigou, D. Vogt, Wiley-VCH, **2005**, p. 346.
- [57] D. Clarke, M. A. Ali, A. A. Clifford, A. Parratt, P. Rose, D. Schwinn, W. Bannwardth, C. M. Rayner, *Curr. Top. Med. Chem.*, **2004**, *7*, 729.
- [58] A. Wittkopp, P. R. Schreiner, *The chemistry of diens and polyenes*, Vol.2, John Wiley & Sons, **2002**
- [59] P. R. Schreiner, *Chem. Soc. Rev.*, **2003**, *32*, 289.
- [60] A. Wittkopp, P. R. Schreiner, *Chem. A Eur. J.*, **2003**, *9*, 407.
- [61] C. M. Kleiner, P. R. Schreiner, *Chem. Commun.*, **2006**, 4315.

- [62] M. Kotke, P. R. Schreiner, *Synthesis*, **2007**, 779, 790.
- [63] S. B. Tsogoeva, *Eur. J. Org. Chem.*, **2007**, 2007, 1701.
- [64] H. Feist, P. Langer, *Synthesis*, **2007**, 327.
- [65] P. Langer, *Synthesis*, **2002**, 441.
- [66] C. Mamat, T. Pundt, T. H. T. Dang, R. Klassen, H. Reinke, M. Köckerling, P. Langer, *Eur. J. Org. Chem.*, **2008**, 492.
- [67] C. Mamat, T. Pundt, A. Schmidt, P. Langer, *Tetrahedron Lett.*, **2006**, 47, 2183.
- [68] A. Marrone, A. Renzetti, P. De Maria, S. Gérard, J. Sapi, A. Fontana, N. Re, *Chem. Eur. J.*, **2009**, 15, 11537.
- [69] M. P. Reetz, *Angew. Chem.*, **1984**, 96, 542; *Angew. Chem. Int. Ed.* **1984**, 23, 556.
- [70] A. Mengel, O. Reiser, *Chem. Rev.*, **1999**, 99, 1191.
- [71] H.-H. Schmidke, U. Voets, *Inorg. Chem.*, **1981**, 20, 2766.
- [72] J. Dabrowski, M. Tencer, *Bull. Chem. Soc. Jp.*, **1976**, 49, 981.
- [73] K. Nakamoto, *Infrared and raman spectra of inorganic and coordination compounds – Part B: Applications in coordination, organometallic and bioorganic chemistry*, 5th edition, John Wiley & Sons, **1997**
- [74] B. M. Badiger, S. A. Patil, S. D. Angadi, V. H. Kulkarni, *J. Less-Common. Met.*, **1987**, 133, 263.
- [75] B. Trumpy, *Z. Phys. A-Hadron Nucl.*, **1934**, 88, 226
- [76] R. Escribano, J. M. Orza, S. Montero, C. Domingo, *Mol. Phys.*, **1979**, 37, 361.
- [77] R. J. Meier, *Faraday Discuss.*, **2003**, 124, 405.
- [78] K. Hirai, I Ojima, *Tetrahedron Lett.*, **1983**, 24, 785.
- [79] P. Brownbridge, T. H. Chan, M. A. Brook, G. J. Kang, *Can. J. Chem.*, **1983**, 61, 688
- [80] K. Dehnicke, *Z. Anorg. Allg. Chem.*, **1961**, 309, 266.
- [81] G. V. Fraser, J. M. Chalmers, V. Charlton, M. E. A. Cudby, *Solid State Commun.*, **1977**, 21, 933.
- [82] H. Miyaoka, K. Hasebe, M. Sawada, H. Sano, H. Mori, G. Mizutani, S. Ushioda, N. Otsuka, M. Terano, *Vib. Spectrosc.*, **1998**, 17, 183.
- [83] A. Pärssinen, P. Elo, M. Klinga, M. Leskelä, T. Repo, *Inorg. Chem. Commun.*, **2006**, 9, 859.
- [84] V. Jonas, G. Frenking, *Organometallics*, **1993**, 12, 2111.
- [85] M. T. Reetz, M. Hüllmann, T. Seitz, *Angew. Chem.*, **1987**, 99, 478; *Angew. Chem. Int. Ed.*, **1987**, 26, 477.
- [86] G. E. Keck, S. Castellino, *J. Am. Chem. Soc.*, **1986**, 108, 3847.
- [87] F. H. Allen, O. Kennard, D. G. Watson, *J. Chem. Soc. Perkin. Trans. II*, **1987**, S1-S18.
- [88] C. A. Wilkie, G.-Y. Lin, D. T. Haworth, *J. Inorg. Nucl. Chem.*, **1978**, 40, 1009.
- [89] N. S. Neelam Jalil, L. T. Hameed, *Phosphorus Sulphur*, **1996**, 112, 171.
- [90] S. Pasynkiewicz, K. B. Starowieyski, A. S. Peregodov, D. N. Kravtsov, *J. Organomet. Chem.*, **1977**, 132, 191.
- [91] J. F. McIntyre, R. T. Foley, B. F. Brown, *Inorg. Chem.*, **1982**, 21, 1167.
- [92] R. H. Holm, F. A. Cotton, *J. Am. Chem. Soc.*, **1958**, 80, 5658.
- [93] K. Nakamoto, P. J. McCarthy, A. Ruby, A. E. Martell, *J. Am. Chem. Soc.*, **1961**, 83, 1066.
- [94] K. Nakamoto, P. J. McCarthy, A. E. Martell, *J. Am. Chem. Soc.*, **1961**, 83, 1272.
- [95] H. Masui, *Coord. Chem. Rev.*, **2001**, 219-221, 957.
- [96] T. Onishi, T. Shimanouchi, *Spectrochim. Acta*, **1964**, 20, 325.
- [97] F. A. Cotton, G. Wilkinson, *Advanced inorganic chemistry - A comprehensive text*, 4th edition, John Wiley & Sons, **1980**, p. 331.
- [98] H. Beyer, W. Walter, *Lehrbuch der organischen Chemie*, 22. überarbeitete und aktualisierte Auflage, Hirtzel, **1991**, p. 542.

- [99] T. A. Egerton, N. J. Everall, J. A. Mattinson, L. M. Kessell, I. R. Tooley, *J. Photoch. Photobiol., A*, **2008**, *193*, 10.
- [100] G. H. Posner, *Angew. Chem.*, **1978**, *90*, 527; *Angew. Chem. Int. Ed.*, **1978**, *17*, 487.
- [101] B. C. Ranu, M. Saha, S. Bhar, *J. Chem. Soc. Perkins Trans. I*, **1994**, 2197.
- [102] S. Reimann, L. R. Knöpke, A. Brückner, U. Bentrup, P. Langer, to be published.
- [103] V. Y. Denyushevskii, L. I. Lafer, V. I. Yakerson, A. M. Rubinshtein, G. A. Gorskaya, *Russ. Chem. B+*, **1970**, *19*, 789.
- [104] L. R. Knöpke, S. Reimann, A. Spannenberg, P. Langer, A. Brückner, U. Bentrup, to be published.
- [105] D. Gegiou, E. Lambi, E. Hadjoudis, *J. Phys. Chem.*, **1996**, *100*, 17762.
- [106] L. R. Knöpke, A. Spannenberg, A. Brückner, U. Bentrup, *Spectrochim. Acta A*, submitted.
- [107] N. S. Biradar, V. H. Kulkarni, *J. Inorg. Nucl. Chem.*, **1971**, *33*, 3847.
- [108] G. C. Percy, D. A. Thornton, *J. Inorg. Nucl. Chem.*, **1972**, *34*, 3357.
- [109] J. E. Kovacic, *Spectrochim. Acta A*, **1967**, *23*, 183.
- [110] J. Strauch, T. H. Warren, G. Erker, R. Fröhlich, P. Saarenketo, *Inorg. Chim. Acta*, **2000**, *300-302*, 810.
- [111] J. W. Lewis, C. Sandorfy, *Can. J. Chem.*, **1982**, *60*, 1727.
- [112] Z. Meić, G. Baranović, *Pure Appl. Chem.*, **1989**, *61*, 2129.
- [113] J. J. López-Garriga, S. Hanton, G. T. Babcock, J. F. Harrison, *J. Am. Chem. Soc.*, **1986**, *108*, 7251.
- [114] I. Ortiz-Hernandez, C. T. Williams, *Langmuir*, **2007**, *21*, 3172.
- [115] P. Teyssie, J. J. Charette, *Spectrochim. Acta*, **1963**, *19*, 1407.
- [116] R. C. Paul, P. K. Gupta, S. L. Chadha, *J. Inorg. Nucl. Chem.*, **1977**, *39*, 1854.
- [117] J. R. Ferraro, *Low-frequency vibrations of inorganic and coordination compounds*, Plenum Press **1971**, p. 121.
- [118] M. Höhne, U. T. Bornscheuer, *ChemCatChem*, **2009**, *1*, 42.
- [119] T. C. Nugent, M. El-Shazly, *Adv. Synth. Catal.*, **2010**, *352*, 753.
- [120] K. Kindler, *Justus Liebig Ann. Chem.*, **1931**, *485*, 113.
- [121] M. S. Taylor, E. N. Jacobsen, *Angew. Chem.*, **2006**, *118*, 1550; *Angew. Chem. Int. Ed.*, **2006**, *45*, 1520.
- [122] T. Akiyama, J. Itoh, K. Fuchibe, *Adv. Synth. Catal.*, **2006**, *348*, 999.
- [123] T. Akiyama, *Chem. Rev.*, **2007**, *107*, 5744.
- [124] X. Yu, W. Wang, *Chem. Asian J.*, **2008**, *3*, 516.
- [125] N. Fleury-Brégot, V. de la Fuente, S. Castillón, C. Claver, *ChemCatChem*, **2010**, *2*, 1346.
- [126] S. E. Clapham, A. Hadzovic, R. H. Morris, *Coord. Chem. Rev.*, **2004**, *248*, 2201.
- [127] H.-U. Blaser, F. Spindler, *Hydrogenation of imino groups in comprehensive asymmetric catalysis*, Vol. 1, edited by E. N. Jacobsen, A. Pfaltz, H. Yamamoto, Springer-Verlag, 1999, p. 247-266.
- [128] A. Tungler, K. Fodor, *Catal. Today*, **1997**, *37*, 191.
- [129] H.-U. Blaser, H.-P. Jalett, M. Müller, M. Studer, *Catal. Today*, **1997**, *37*, 441.
- [130] M. Studer, H.-U. Blaser, C. Exner, *Adv. Synth. Catal.*, **2003**, *345*, 45.
- [131] M. van Arx, T. Mallat, A. Baiker, *Top. Catal.*, **2002**, *19*, 75.
- [132] P. Wells, A. Wilkinson, *Top. Catal.* **1998**, *5*, 39.
- [133] G. Szöllösi, I. Kun, M. Bartók, *Chirality*, **2001**, *13*, 619.
- [134] A. S. C. Chan, C. C. Chen, C. W. Lin, Y. C. Lin, M. C. Cheng, S. M. Peng, *J. Chem. Soc. Chem. Comm.*, **1995**, 1767.
- [135] X. Verdager, U. E. W. Lange, S. L. Buchwald, *Angew. Chem.*, **1998**, *110*, 1174; *Angew. Chem. Int. Ed.*, **1998**, *37*, 1103.
- [136] M. Rueping, E. Sugiono, C. Azap, T. Theissmann, M. Bolte, *Org. Lett.*, **2005**, *7*, 3781.

- [137] M. Rueping, C. Azap, E. Sugiono, T. Theissmann, *Synlett*, **2005**, 2367.
- [138] S. Hoffmann, A. M. Seayad, B. List, *Angw. Chem.*, **2005**, *117*, 7590; *Angew. Chem. Int. Ed.*, **2005**, *44*, 7424.
- [139] L. Simon, J. M. Goodman, *J. Am. Chem. Soc.*, **2008**, *130*, 8741.
- [140] T. Marcelli, P. Hammar, F. Himo, *Chem. A. Eur. J.*, **2008**, *14*, 8562.
- [141] A. Dondoni, A. Massi, *Angew. Chem.*, **2008**, *120*, 4716; *Angew. Chem Int. Ed.*, **2008**, *47*, 4638.
- [142] C. Sandorfy, D. Vocelle, *Can. J. Chem.*, **1986**, *64*, 2251.
- [143] Z. Meić, G. Baranović, T. Šuste, *J. Mol. Struc.*, **1993**, *296*, 163.
- [144] H. Le Thanh, G. Richer, C. Sandorfy, P. P. Vaudreuil, D. Vocelle, *Can. J. Spectrosc.*, **1988**, *33*, 128.
- [145] M. Bissonnette, H. Le Thanh, D. Vocelle, *Can. J. Chem.*, **1984**, *62*, 1459.
- [146] M. Allen, J. D. Roberts, *J. Org. Chem.*, **1980**, *45*, 130.
- [147] G. A. Olah, P. Kreienbühl, *J. Am. Chem. Soc.*, **1967**, *89*, 4756.
- [148] M. J. Kamlet, J. L. M. Abboud, M. H. Abraham, R. W. Taft, *J. Org. Chem.*, **1983**, *48*, 2877.
- [149] C. Reichardt, *Chem. Rev.*, **1994**, *94*, 2319.
- [150] J. P. Bégué, D. Bonnet-Delpon, B. Crousse, *Synlett*, **2004**, 18.
- [151] G. Socrates, *Infrared and raman characteristic group frequencies*, John Wiley & Sons, **2001**
- [152] V. Setnička, M. Urbanová, P. Bouř, V. Král, K. Volka, *J. Phys. Chem. A*, **2001**, *105*, 8931.
- [153] S. Alex, P. Turcotte, R. Fournier, D. Vocelle, *Can. J. Chem.*, **1991**, *69*, 239.
- [154] S. Masuda, H. Torii, M. Tasumi, *J. Phys. Chem.*, **1996**, *100*, 15328.
- [155] L. S. Loussier, A. Dion, C. Sandorfy, H. Le Thanh, D. Vocelle, *Photochem. Photobiol.*, **1986**, *44*, 629.
- [156] L. S. Loussier, C. Sandorfy, H. Le Thanh, D. Vocelle, *J. Phys. Chem.*, **1987**, *91*, 2282.
- [157] T. Baasov, N. Friedman, M. Sheves, *Biochemistry*, **1987**, *26*, 3210.
- [158] P. E. Blatz, J. H. Mohler, H. V. Navangul, *Biochemistry*, **1972**, *11*, 848.
- [159] M. Bissonnette, H. Le Thanh, D. Vocelle, *Can. J. Chem.*, **1985**, *63*, 2298.
- [160] P. Brocklehurst, *Tetrahedron*, **1962**, *18*, 299.
- [161] M. Fleischmann, D. Drettwan, E. Sugiono, M. Rueping, R. M. Gschwind, *Angew. Chem.*, **2011**, *123*, 6488; *Angew. Chem. Int. Ed.*, **2011**, *50*, 6364.
- [162] J. J. López-Garriga, G. T. Babcock, J. F. Harrison, *J. Am. Chem. Soc.*, **1986**, *108*, 7241.
- [163] O. Berkesi, T. Körtvélyesi, C. Hetényi, T. Németh, I. Pálinkó, *Phys. Chem. Chem. Phys.*, **2003**, *5*, 2009.
- [164] S. D. Ebbesen, B. L. Mojet, L. Leffers, *J. Catal.*, **2008**, *256*, 15.
- [165] S. Das, D. Addis, L. R. Knöpke, U. Bentrup, A. Brückner, K. Junge, M. Beller, *Angew. Chem.*, **2011**, *123*, 9346; *Angew. Chem. Int. Ed.*, **2011**, *50*, 9180.
- [166] G. Walther, L. R. Knöpke, J. Rabeah, M. P. Checinski, H. Jiao, U. Bentrup, A. Brückner, A. Martin, A. Köckritz, to be published
- [167] R. Hoffmann, P. von Ragué Schleyer, H. F. Schaefer III, *Angew. Chem.*, **2008**, *120*, 7276; *Angew. Chem. Int. Ed.*, **2008**, *74*, 7164.
- [168] K. Danzer, H. Hobert, C. Fischbacher, K.-U. Jagemann, *Chemometrik: Grundlagen und Anwendungen*, Springer-Verlag, **2001**
- [169] E. Kriesten, D. Mayer, F. Alsmeyer, C. B. Minnich, L. Greiner, W. Marquardt, *Chemometr. Intell. Lab.*, **2008**, *93*, 108.
- [170] C. Kubis, R. Ludwig, M. Sawall, K. Neymeyr, A. Börner, K.-D. Wiese, D. Hess, R. Franke, D. Selent, *ChemCatChem*, **2010**, *2*, 287.
- [171] M. Garland, *Catal. Today*, **2010**, *155*, 266.



Experimental Section

APPLICATION EXAMPLE 1:

Elucidating the directing effect of Lewis acids on the reaction pathway in formal [3+3] cyclocondensation reactions

Chemicals and solvents

The applied Lewis acids were received from commercial sources and were used without further purification: Trimethylsilyltrifluoro-methanesulfonate (99%) from ACROS Organics, Titanium(IV)chloride (99.995%) from Aldrich. TiO_2 was received from Sachtleben Chemie GmbH and Al_2O_3 from Sasol Germany GmbH. The solvent CH_2Cl_2 (99.8% extra dry over molecular sieves, stabilized) was obtained from ACROS Organics. 1,3-bis(silyloxy)-1,3-butadiene **1** has been prepared according to literature [a]. The ketenacetals **2a** and **2b** were synthesised according to the protocol of Bunescu et al. [b]. N-salicylideneaniline (97%) was used as received from Aldrich.

General procedures

Ex situ studies: All liquid samples were measured at room temperature in CH_2Cl_2 at $0.5 \text{ mol}\cdot\text{L}^{-1}$ if no other concentration is mentioned. All vessels were flushed with argon and remained closed until start of analysis.

The solid sample of **19** was prepared by mixing solid N-salicylideneaniline **14** with liquid TiCl_4 in 1.0 mL in CH_2Cl_2 in molar ratios of 1:1 and 2:1. The solutions had a concentration of $0.5 \text{ mol}\cdot\text{L}^{-1}$ and the precipitation of **19** occurred spontaneously. Remaining rests of solvent and TiCl_4 were removed by drying the sample.

Ketenacetale **2b** was adsorbed on Al_2O_3 or TiO_2 by stirring a suspension of Al_2O_3 / TiO_2 for one hour at room temperature. The Volume of CH_2Cl_2 was 2.0 mL and the concentration of **2b** $0.5 \text{ mol}\cdot\text{L}^{-1}$. The used amounts of the solids were 0.166 g of Al_2O_3 and 0.120 g of TiO_2 . Afterwards the mixture was filtrated over Whatman Qualitative 5 filtration papers, washed with 3 portions of 5 mL each CH_2Cl_2 and dried overnight on air.

In situ studies: The reaction was carried out in a homemade reaction cell. The cooling has done by a Julabo cryostat. The reaction cell was flushed with argon before reaction and during dosing when the cell was open.

Ketenacetale **2b** (736 mg, 4 mmol) or N-salicylideneaniline **14** (788 mg, 4 mmol) has been dissolved in CH₂Cl₂ at room temperature. The cooling of the solution started and the Lewis acid (722 mg, 4 mmol TMSOTf in 1.0 mL CH₂Cl₂ / 440 μL, 4 mmol TiCl₄ / 533 mg, 4 mmol in 1.0 mL CH₂Cl₂ AlCl₃) has been added when a temperature of 0°C was reached. The total volume was 12 mL now. The solution was cooled down to -60°C, and the diene **1** (2080 mg / 8 mmol) was added. Then the mixture was warmed to 0°C over 4 hours. Finally, the reaction was quenched by addition of 60 mL 10% HCl solution to the reaction mixture.

Data collection

Ex situ studies liquid samples: ATR-FTIR spectra were measured with a Bruker Alpha FTIR spectrometer which was equipped with a Platinum ATR single reflection diamond ATR module. All spectra were recorded with 32 scans at 4 cm⁻¹ resolution.

UV-vis spectra were performed using an AvaSpec 2048 fiber optical spectrometer (Avantes B.V., Eerbeek, Netherlands) equipped with an AvaLight-DHS light source and a FDP-UV-micro-1 transmission probe. The UV-vis spectra were recorded with 50 accumulations and 10 ms integration time.

Raman spectra were recorded using a RXN1-785 Raman system (Kaiser Optical Systems, KOSI Inc., Michigan, USA) equipped with a 70 mW diode laser for excitation at a wavelength of 785 nm. The Raman spectra were recorded with 3 accumulations and 3 sec exposure time.

Ex situ studies solid samples: The solid samples of **14** and **19** were measured with a Bruker Alpha spectrometer equipped with a Platinum ATR single reflection diamond ATR module. The spectrum was recorded with 32 scans at 4 cm⁻¹ resolution. The wafer for the analysis of **2b** adsorbed on Al₂O₃ was made by pressing 50 mg material with 10 tons to a disc with a diameter of 20 mm and was analysed by a Bruker Tensor 27 spectrometer. The cell was evaporated followed by recording the spectrum at room temperature with 50 scans at 2 cm⁻¹ resolution.

The UV-vis spectra were sampled with an AvaSpec 2048 fiber optical spectrometer (Avantes B.V., Eerbeek, Netherlands) equipped with an AvaLight-DHS light source and a FCR-7xx200-2-45 reflection probe. All spectra were recorded with 30 accumulations and an integration time of 23 ms.

In situ studies: ATR-FTIR spectra were recorded by using a fiber optical diamond ATR probe (infrared fiber sensors, Aachen, Germany) connected to a Nicolet Avatar 370 (Thermo Electron) FTIR spectrometer. All spectra were recorded at 4 cm^{-1} resolution with 128 scans.

The UV-vis spectra were collected with the same equipment and same parameters as in the ex situ studies.

APPLICATION EXAMPLE 2

Heterogeneously catalysed asymmetric hydrogenation of imines: Reaction monitoring and mechanistic studies

Chemicals and solvents

All chemicals and solvents were used as received without any further purification. The imines were synthesised from acetophenone(derivates) and aniline(derivates) in toluene using sodium hydrogen carbonate and molecular sieves according to the protocol of Malkov et al. [c]. The acetophenone(derivates) were used as received from Aldrich. Acetophenone (Reagent Plus, 99), propiophenone (99+%), 4'-bromoacetophenone (98%), p-methylacetophenone (95%) and 2-hydroxyacetophenone (99%). Aniline ($\geq 99.5\%$, ACS reagent) was obtained from Sigma-Aldrich and used as received. 4-bromoaniline (puriss., $>99.0\%$ GC), p-toluidine (99.7%) and p-anisidine (99%) were supplied by Aldrich and were used as received as well.

Molecular sieves 4 \AA were received from Merck and sodium bicarbonate ($\geq 99.5\%$, ACS, ISO) from Carl Roth. Toluene (99.8% extra dry over molecular sieves) was obtained from ACROS Organics, dichloromethane (pure, stabilised with ca. 0.2% ethanol) from ACROS Organics, methanol (Chromasolv) from Sigma-Aldrich and 2,2,2-trifluoroethanol (99.8% zur Synthese) from Carl Roth. Rac-1,1'-binaphthyl-2,2'-diyl hydrogenphosphate **22** (95%), N-benzylideneaniline **24** (99%) and N-salicylideneaniline **14** (97%) were used as received from Aldrich.

The used platinum catalysts are obtained from STREM Chemicals (5 wt% platinum on silica powder, reduced, dry (Escat 2351)) and from Evonik (5 wt% on alumina, reduced, dry (catASium F214)).

Interaction of the imines with 1,1'-binaphthyl-2,2'-diyl hydrogenphosphate 22: The interaction of the imine **21** with **22** was investigated in CH_2Cl_2 applying concentrations of $0.5\text{ mol}\cdot\text{L}^{-1}$

obtained by dissolving 98 mg of the imine **21** in 1.0 mL CH₂Cl₂. 175 mg of **22** was added in 35 mg portions under vigorous stirring.

Analysis of the Pt/Al₂O₃ catalyst after hydrogenation reaction: After hydrogenation reaction the used catalyst samples were separated from the reaction mixture by filtration. The filtration cake was washed three times with 10 mL CH₂Cl₂ and dried at room temperature in a fume hood.

For comparison, a reference spectrum of the pure as-received Pt/Al₂O₃ catalyst before and after separate adsorption of imine **14** was taken. For the imine adsorption, the catalyst was stirred in a solution of 1.58 g **14** in 40 mL CH₂Cl₂ for 4h. Then, the catalyst was separated by filtration (Whatman Qualitative 5 filtration papers), washed three times with 10 mL CH₂Cl₂, and dried at ambient temperature in a fume hood.

The adsorption experiments for **20** and **21** on Pt/Al₂O₃ and **14** and **21** on Pt/SiO₂ have been carried out in the same manner but within 5 mL solvent with 198 mg **14**, 221 mg **20**, 196 mg **21**, and 90 mg of Pt/SiO₂. All solids were analysed from self-supporting wafers by FTIR-transmission spectroscopy.

In situ monitoring of the hydrogenation reaction: The in situ analysis of the hydrogenation of imines (0.2 mol·L⁻¹) was performed in CH₂Cl₂ or CF₃CH₂OH at 25°C. 1.57 g **21** or 1.45 g **24** were dissolved in 40 mL of the solvent. 32 / 64 mg of the Pt/Al₂O₃ catalyst or 55 mg Pt/SiO₂ catalyst was used in the experiment. For testing the setup, the hydrogenation was firstly carried out without **22**. Before starting the reaction the reaction mixture was flushed three times with argon and three times with hydrogen. The initial hydrogen pressure was 20 bar. The reaction started with switching-on the stirrer (400 rpm) and reaction progress could be monitored by the pressure drop which was usually about 4 bar.

Data acquisition

The ATR-FTIR spectra of the solid samples were measured with a Bruker Alpha spectrometer equipped with a Platinum ATR single reflection diamond ATR. The spectra were recorded with 32 scans at 4 cm⁻¹ resolution at room temperature.

All ATR-FTIR and Raman spectra of the dissolved samples have been measured in CH₂Cl₂ with a concentration of 0.5 mol·L⁻¹ at room temperature. The ATR-FTIR spectra were measured with a Nicolet Avatar 370 (Thermo Electron) FTIR spectrometer equipped with a

fiber optical diamond ATR probe (infrared fiber sensors, Aachen, Germany) with 128 scans at 4 cm^{-1} resolution.

Raman spectra were recorded using a RXN1-785 Raman system (Kaiser Optical Systems, KOSI Inc., Michigan, USA) equipped with a 70 mW diode laser for excitation at a wavelength of 785 nm. The Raman spectra were recorded with 3 accumulation terms with 3 seconds exposure time.

UV-vis spectra of the dissolved samples have been measured in CH_2Cl_2 with a concentration of $5 \cdot 10^{-4}\text{ mol}\cdot\text{L}^{-1}$. UV-vis spectra were performed with an AvaSpec 2048 fiber optical spectrometer (Avantes B.V., Eerbeek, Netherlands) equipped with an AvaLight-DHS light source and a FDP-UV-micro-1 transmission probe. The UV-vis spectra were recorded with 50 accumulations and 10 ms integration time.

Selected bond lengths and angles in the bis-chelate complex **8b**

Suitable crystals for X-ray analysis could be obtained from the 1:1-mixture of ketenacetales **2a** and **2b** and TiCl_4 in CH_2Cl_2 solution. The obtained molecular structure is shown in Figure S1, selected bond lengths and angles are given in the Table A.

Table A. Selected bond lengths [Å] and angles [°] in bis-chelate complex **8b**.

Ti1-O1	1.9028(12)	Ti2-O7	1.8993(12)
Ti1-O4	1.8961(12)	Ti2-O10	1.8955(12)
Ti1-O2	2.0805(12)	Ti2-O8	2.0834(12)
Ti1-O5	2.0730(13)	Ti2-O11	2.0634(12)
O1-C2	1.300(2)	O8-C14	1.244(2)
O4-C7	1.309(2)	C19-O11	1.246(2)
C4-O2	1.244(2)	O10-C17	1.305(2)
C9-O5	1.239(2)	C12-O7	1.304(2)
C3-C2	1.337(3)	C17-C18	1.340(3)
C7-C8	1.338(3)	C13-C12	1.340(3)
C4-C3	1.431(2)	C14-C13	1.436(3)
C8-C9	1.434(3)	C18-C19	1.433(3)
O8-Ti2-O11	84.16(5)	O4-Ti1-O5	83.16(5)
O11-Ti2-C14	91.13(4)	O5-Ti1-O1	82.95(5)
C14-Ti2-C13	97.08(2)	O1-Ti1-O2	83.26(5)
C13-Ti2-O8	87.76(4)	O2-Ti1-O4	81.81(5)
O8-Ti2-O10	83.06(5)	O1-Ti1-C11	96.90(4)
O8-Ti2-O7	82.99(5)	O1-Ti1-C11	94.44(4)

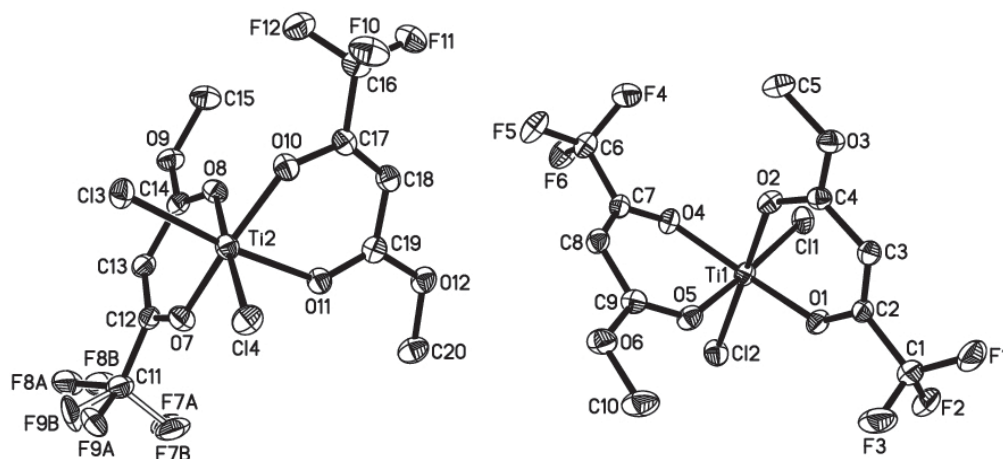


Figure S1. Molecular structure of the bis-chelate complex **8b**. Displacement ellipsoids are drawn at the 30% probability level. Hydrogen atoms are omitted for clarity.

ATR-FTIR and Raman spectrum of N-salicylideneaniline **14 in CCl₄ (cf. Figure 25)**

The different band intensities occurring in the ATR-FTIR and Raman spectra of the same sample (**14** in CCl₄; $c = 0.5 \text{ mol}\cdot\text{L}^{-1}$) are shown in Figure B. The vibrations at 1618 / 1619, 1593 and 1573 cm^{-1} ($\nu(\text{C}=\text{N})$, $\nu(\text{Ph}-\text{N})$ and $\nu(\text{Ph}-\text{C})$ vibration modes) occur in different but still strong intensities in both spectra. Contrary the band of the $\nu(\text{Ph}-\text{OH})$ vibration occurs with strong intensity at 1283 cm^{-1} in the ATR-FTIR spectrum but with very weak intensity at 1286 cm^{-1} in the Raman spectrum. In contrast the Raman spectrum shows a distinct band at 1322 cm^{-1} which does not appear in the ATR-FTIR spectrum.

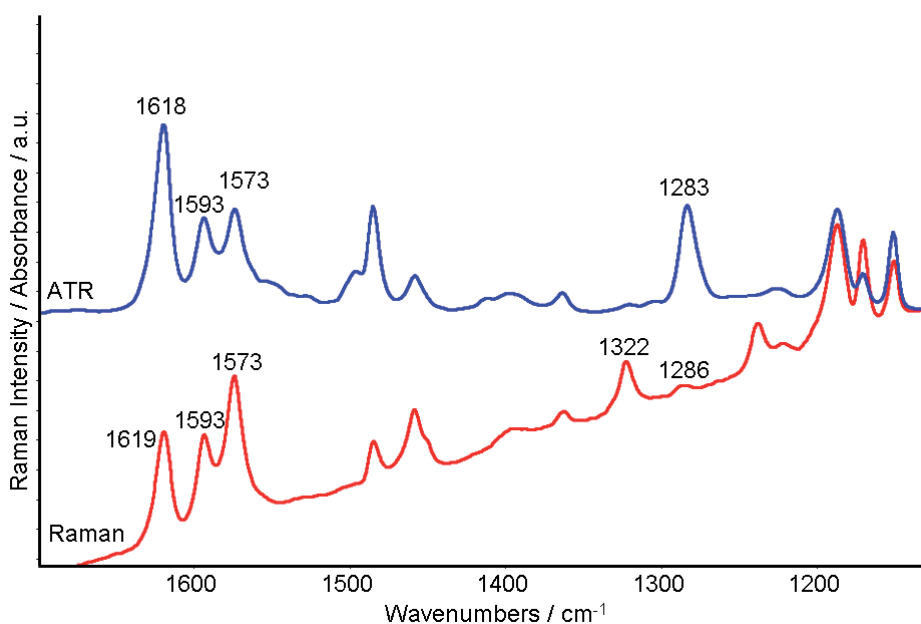


Figure B. N-salicylideneaniline **14** in CCl₄ ($c = 0.5 \text{ mol}\cdot\text{L}^{-1}$); ATR-FTIR spectrum (above) and Raman spectrum (below).

ATR-FTIR spectrum of the 1:1-mixture of **14 and **22** in CH₂Cl₂ before the co-adsorption experiment on Pt/Al₂O₃ took place (cf. Figure 41)**

The interaction between N-salicylideneaniline **14** and 1,1'-binaphthyl-2,2'-diyl hydrogen-phosphate **22** in CH₂Cl₂ ($c = 0.5 \text{ mol}\cdot\text{L}^{-1}$) are shown in Figure C. The bands at 1231 / 1212, 1092/1068, 962 / 945 and 867 / 852 / 833 / 816 cm⁻¹ of the 1:1-mixture of **14** and **22** occur in similar positions as in the 1:1-mixture of **22** and KOH (cf. Figure 30). Hence the appearance of these bands indicates the dissociation of **22**. The band at 1589 cm⁻¹ can be dedicated to a vibration of **22**. The bands at 1661 and 1611 cm⁻¹ can be assigned as $\nu(\text{C}=\text{O})$ and $\nu(\text{C}=\text{C})$ vibrations of the quinoid-tautomer. Finally the bands at 1646 and 1618 cm⁻¹ can be dedicated to the $\nu(\text{C}=\text{NH}^+)$ and the $\nu(\text{C}=\text{C})$ vibration modes of the phenyl rings.

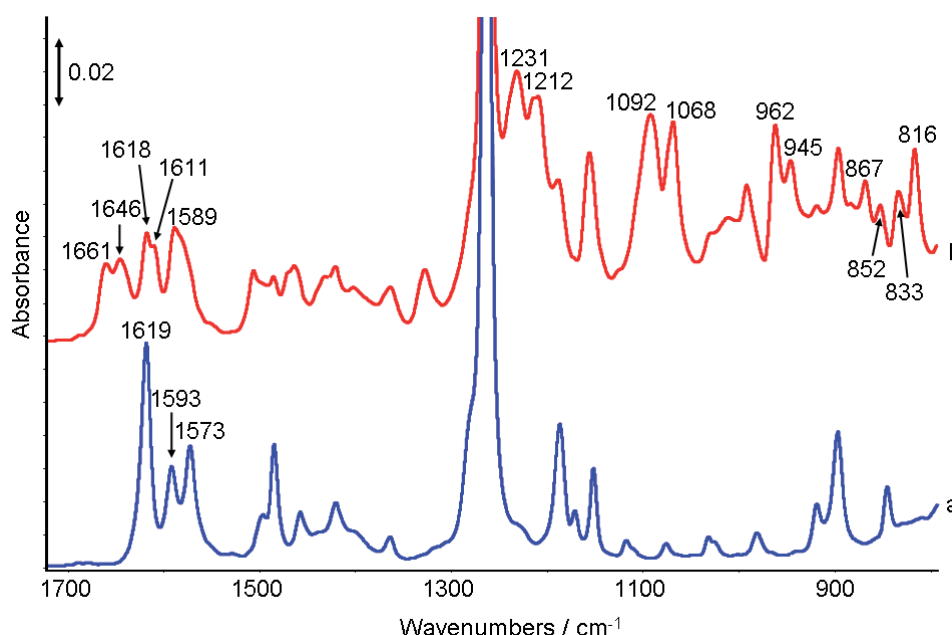


Figure C. ATR-FTIR spectra of (a) pure **14** and (b) a 1:1-mixture of **14** and **22** in CH₂Cl₂ ($c = 0.5 \text{ mol}\cdot\text{L}^{-1}$).



Remark to the spectroscopic limitations

The ATR-FTIR probes provide information in diluted liquid systems only between 1800 and 650 cm^{-1} . The transmittance of the probe (cf. Figure D) is limited due to the MCT-detector and by the absorption of the diamond prism. Both compounds hinder to detect signals in adequate signal to noise ratio in other wavenumber regions. Generally, the energy throughput is relatively low. Conventional ATR-FTIR units have a peak value (indicates the energy throughput) of 6.40 while good probes have only 0.30. Thus, the signal to noise ratio is naturally higher.

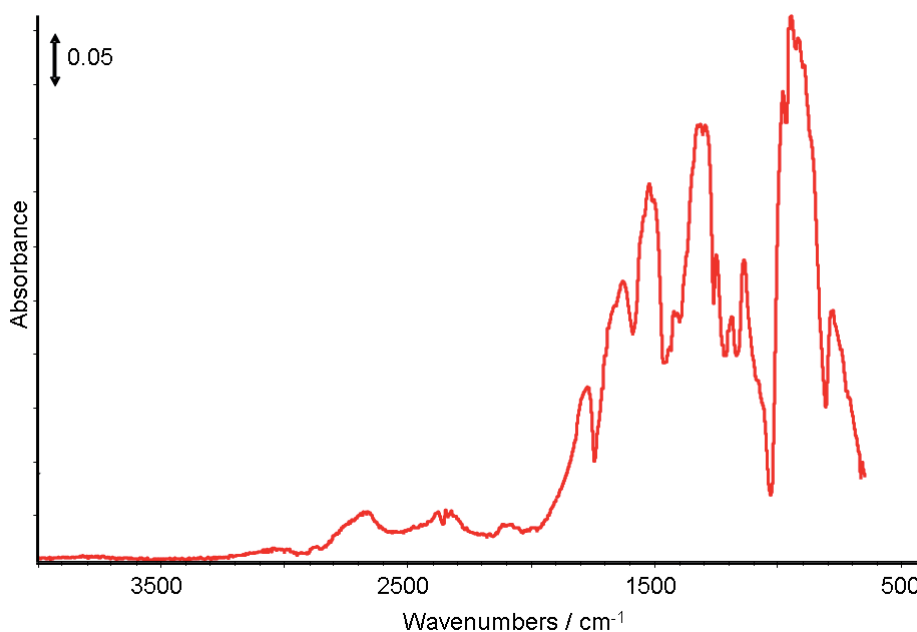
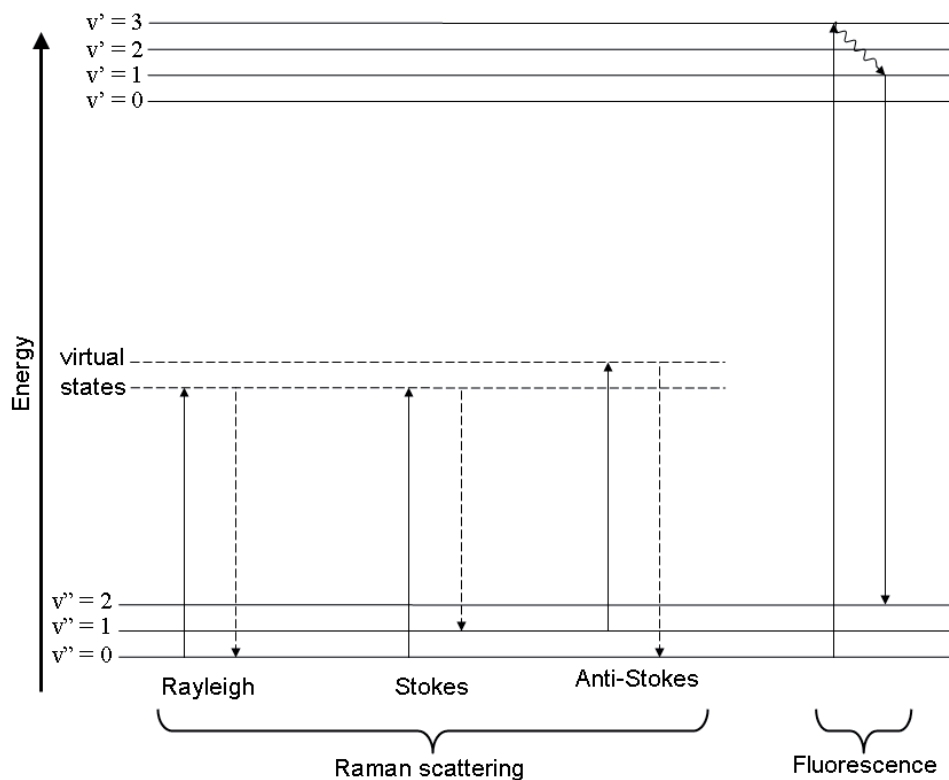


Figure D. Transmittance of the ATR-FTIR probe.

Another frequently occurring problem is when the possible strong adsorption of reaction products or precipitates adhere during reaction on the diamond prism. These adsorbates might cause wrong interpretation about reaction progress and are sometimes difficult to remove after reaction. On the other hand if the adsorbates are reaction intermediates they can be observed very nicely under the applied reaction conditions because of their relatively high concentration. Interestingly, such effects were not observed on the lens and the optical windows of the Raman und UV-vis probes. Contrary to the ATR-FTIR probe the Raman probe has not such a limitation referring to the detection area. Here is the complete spectra region from 3250 – 150 cm^{-1} accessible. The important drawback is fluorescence which occurs in many cases when organic substrates are used (cf. Figure E and Scheme A) [d, e].



Scheme A. Jablonski diagram of Raman and fluorescence processes.

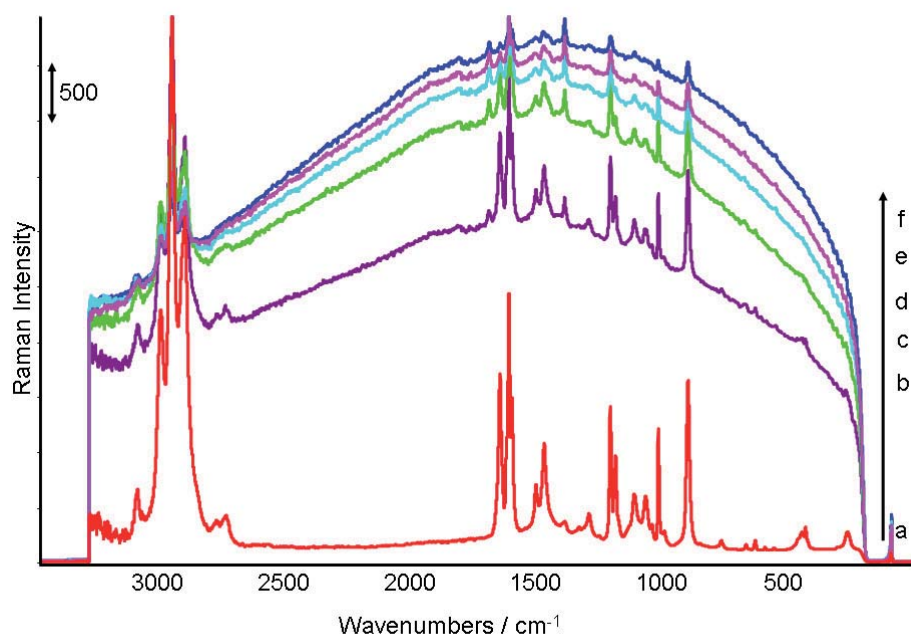


Figure E. Increasing fluorescence due to dosing of **22** to **24** in CH_2Cl_2 ($c=0.5 \text{ mol}\cdot\text{L}^{-1}$): (a) 0, (b) 20, (c) 40, (d) 60, (e) 80 and (f) 100 mol-% **22**.

The application of UV-vis spectroscopy is difficult considering the concentration of the reactants in the reaction mixture. If the concentration is too high the bands become broader and the result is one blurred band as shown in Figure F. In higher concentrated solutions the equipment detects also transitions which are too weak to be detected under normal conditions.

This leads to a band shift to longer wavelengths. Another important drawback is that the law of Lambert and Beer is not valid if the concentration is too high

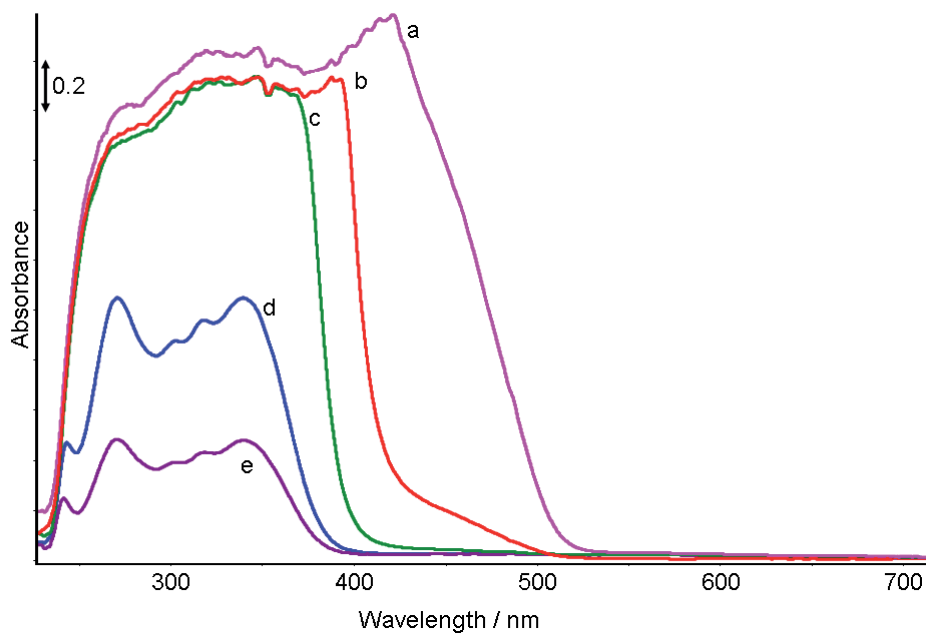


Figure F. Dilution series of **14** in CH₂Cl₂: (a) $c=5 \cdot 10^{-1} \text{ mol} \cdot \text{L}^{-1}$, (b) $c=5 \cdot 10^{-2} \text{ mol} \cdot \text{L}^{-1}$, (c) $c=5 \cdot 10^{-3} \text{ mol} \cdot \text{L}^{-1}$, (d) $c=5 \cdot 10^{-4} \text{ mol} \cdot \text{L}^{-1}$, (e) $c=5 \cdot 10^{-5} \text{ mol} \cdot \text{L}^{-1}$.

Remark to the limitations measuring kinetics

The obtained reaction rates should not be considered as true kinetics. Therefore the reaction unit has too many intrinsic limitations. One important drawback is the tempering of the autoclave. Tempering around 20°C is difficult and usually realised by simultaneous heating and cooling. This is not possible in this case because the cooling loop line was removed to enable the installation of the probes. Consequently, the heating is not modified considering the missing cooling loop which provokes too strong heating because the lack of cooling capacity. This problem becomes smaller with rising temperature because less cooling is required and cool air surrounding the unit has less effect on the reactor temperature. The temperature inside the autoclave may change also because the gas dosed from the hydrogen burette is cooled down due to the Joule-Thomson-effect. Finally the massive reactor walls made from stainless steel impede fast tempering of the reaction mixture as well, especially when the mixture is stored in the glass insert inside the reactor.

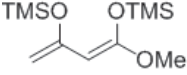
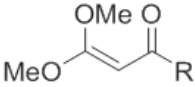
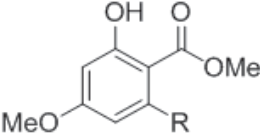
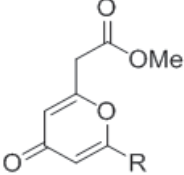
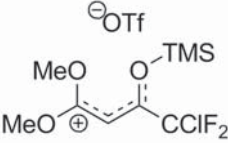
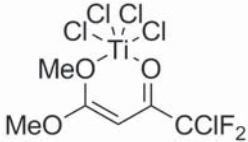
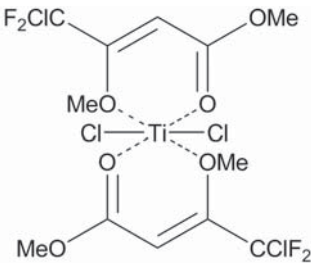
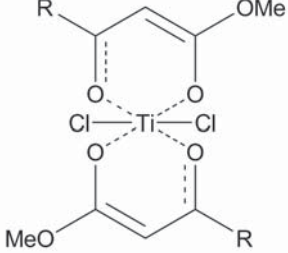
These problems may be partly overcome when the investigations takes place at higher temperatures because in this case the heating is used mainly to hold the working temperature. This was not possible for the hydrogenation reaction because the reaction becomes too fast for a proper analysis at higher temperatures.

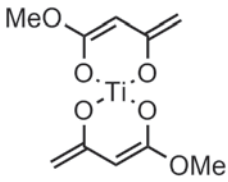
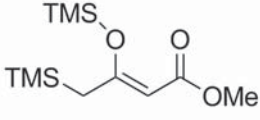
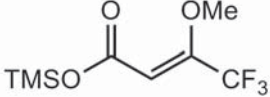
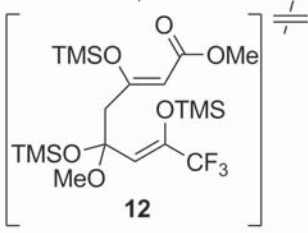
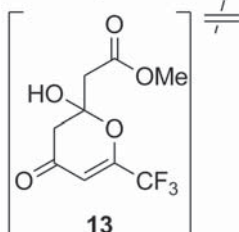
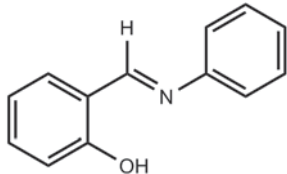
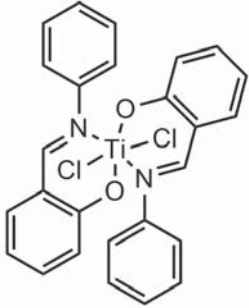
Mass transfer limitation occurring inside the autoclave during the measurements has to be considered as well. Here should be separated between the solubility of reaction gas in the liquid phase and passage of reaction gas from the gaseous phase into the liquid phase. The solubility depends on the applied solvent and the solvent temperature. When the solubility is small and the reaction is faster than the reactive gas is replenished from the gaseous phase. Consequently, mass transfer limitation will occur. The passage of reaction gas from the gaseous phase into the liquid phase strongly depends on the stirring rate. High stirring rates favours the fast passage of reactive gas into the liquid phase [f]. Besides the geometry of stirrer and reactor the stirring rate is the principal parameter. But the stirring rate inside the autoclave is determined by the stirring stability of the magnetic stirring bar. The installation of an overhead stirrer is not possible because all flanges are already occupied by probes, the gauge or the gas supply.

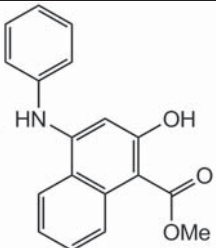
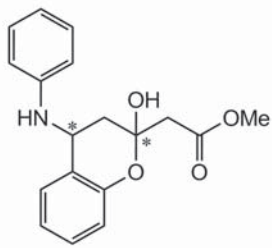
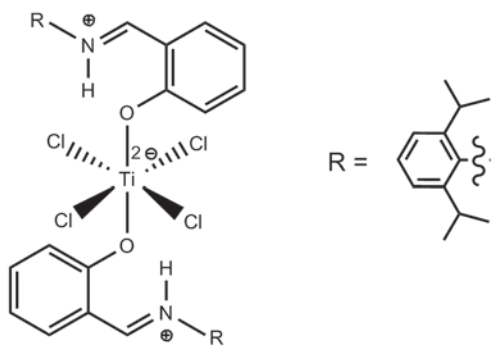
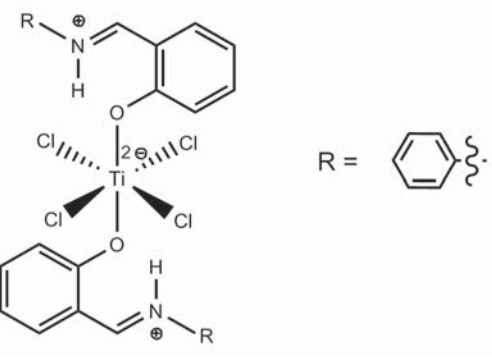
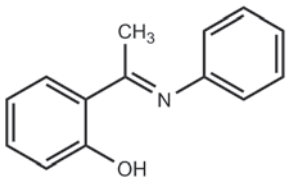
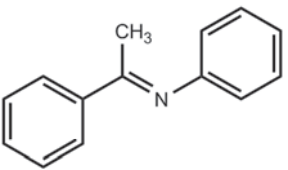
Comprehensively these aspects show that a proper kinetic analysis is difficult with the current setup. Even if the pointed out proposals for improvement will be realized there still difficulties to overcome. Nevertheless the current setup is adequate to detect reaction speeds which are adequate to answer the questions about occurring adsorbates on the catalyst surface on the reaction performance. Under the applied conditions the spectroscopic devices have an

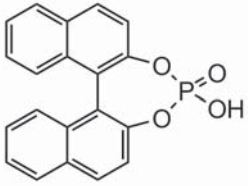
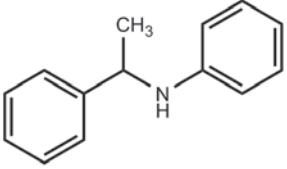
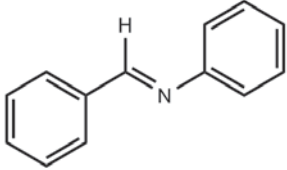
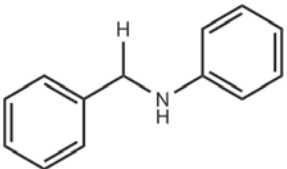
adequate resolution to give detailed information of the reaction progress. Tests show that the results are reproducible within a small experimental error.

Table of compounds

Entry	Structure	Description
1		1,3-bis(silyloxy)-1,3-butadiene (diene)
2a,b		Ketenacetale 2a: R = CCIF ₂ , 2b: R = CF ₃
3a,b		Salicylate-type product in the TiCl ₄ -mediated cyclocondensation reaction of 1 and 2a,b 3a: R = CCIF ₂ , 3b: R = CF ₃
4a,b		Pyranone type product in the TMSOTf-mediated cyclocondensation reaction of 1 and 2a,b 4a: R = CCIF ₂ , 4b: R = CF ₃
5		Intermediate formed between 2a and TMSOTf
6		Intermediate formed between 2a and TiCl ₄ proposed from UV-vis spectrum
7		Intermediate formed between 2a and TiCl ₄ proposed from ATR-FTIR spectrum
8a,b		Intermediate formed between 2a , 2b and TiCl ₄ proved by X-Ray single crystal structure analysis

9		Intermediate formed between 1 and TiCl ₄
10		Intermediate formed between 1 and TMSOTf
11		Rearrangement product of 10 at -60°C
12		Proposed in situ formed intermediate in the TMSOTf-mediated cyclocondensation reaction of 1 and 2b to 3b
13		Proposed in situ formed intermediate in the TMSOTf-mediated cyclocondensation reaction of 1 and 2b to 3b
14		N-salicylideneaniline (aldimine)
15		Proposed intermediate formed between 14 and TiCl ₄

16		Proposed naphthene-type product in the TiCl_4 mediated cyclocondensation reaction of 1 and 14
17		Obtained chromane-type product in the TiCl_4 mediated cyclocondensation reaction of 1 and 14
18		Compound described by Strauch et al. [g]
19		Isolated intermediate formed between 14 and TiCl_4
20		2-(1-(phenylimino)ethyl)phenol (ketimine)
21		N-(1-phenylethylidene)aniline (ketimine)

22		1,1'-binaphthyl-2,2'-diyl hydrogenphosphate (model compound)
23		N-(1-phenylethyl)aniline (hydrogenation product of 21)
24		N-benzylideneaniline (aldimine)
25		N-benzylaniline (hydrogenation product of 23)



Supplementary literature

- [a] G. A. Molander, K. O. Cameron, *J. Am. Chem. Soc.*, **1993**, *115*, 830.
- [b] A. Bunescu, S. Reimann, M. Lubbe, A. Spannenberg, P. Langer, *J. Org. Chem.*, **2009**, *74*, 5002.
- [c] A. V. Malkov, A. Mariani, K. N. MacDougall, P. Kocovsky, *Org. Lett.*, **2004**, *6*, 2253.
- [d] R. L. MeeCreery *Raman Spectroscopy form Chemical Analysis – Chemical Analysis* Vol. **157**, edited by J. D. Wineforder, John Wiley & Sons, **2000**, p. 3-5.
- [e] B. M. Weckhuysen, *In situ spectroscopy of catalysts* – edited by B. M. Weckhuysen, American Scientific Publishers **2004**
- [f] G. W. Roberts, *Catalysis in Organic Synthesis* – edited by P. Rylander and H. Greenfield, Academic Press, Inc. **1976**, p. 32 – 35.
- [g] J. Strauch, T. H. Warren, G. Erker, R. Fröhlich, P. Saarenketo, *Inorg. Chim. Acta*, **2000**, *300-302*, 810.



